SUPPRESSION OF VORTEX-INDUCED VIBRATIONS FOR ELLIPTICAL CYLINDERS USING MIXED CONVECTION

THESIS

Jeffrey A. DesRoches, Captain, USAF

AFIT-ENY-MS-18-M-251

DEPARTMENT OF THE AIR FORCE
AIR UNIVERSITY

AIR FORCE INSTITUTE OF TECHNOLOGY

Wright-Patterson Air Force Base, Ohio

AFIT-ENY-MS-18-M-251

SUPPRESSION OF VORTEX-INDUCED VIBRATIONS FOR ELLIPTICAL CYLINDERS USING MIXED CONVECTION

THESIS

Presented to the Faculty

Department of Aeronautics and Astronautics

Graduate School of Engineering and Management

Air Force Institute of Technology

Air University

Air Education and Training Command

In Partial Fulfillment of the Requirements for the

Degree of Master of Science in Aeronautical Engineering

Jeffrey A. DesRoches, BS

Captain, USAF

March 2018

DISTRIBUTION STATEMENT A.
APPROVED FOR PUBLIC RELEASE; DISTRIBUTION UNLIMITED.

AFIT-ENY-MS-18-M-251

SUPPRESSION OF VORTEX-INDUCED VIBRATIONS FOR ELLIPTICAL CYLINDERS USING MIXED CONVECTION

Jeffrey A. DesRoches, BS
Captain, USAF

Committee Membership:

Dr. Anthony N. Palazotto
Chair

Dr. Hui Wan
Member

Dr. William P. Baker
Member

Abstract

Transverse vortex-induced vibrations (VIVs) of a 2-D, elliptic cylinder with various aspect ratios and stiffness are studied. The cylinder is elastically mounted and heated, and the flow direction is aligned with the direction of the thermal induced buoyancy force. The amplitude of transverse motion due to VIVs can be reduced as the thermal control parameter, the Richardson number (*Ri*), increases. Complete suppression is achieved when *Ri* is above a critical value. This critical *Ri* depends on both body-to-fluid density, aspect ratio, and structural stiffness. The study includes finding the lock-in regime for each aspect ratio, where the vibrational amplitude is at a maximum. Bodies at lock-in require a higher critical *Ri* to suppress VIV than either rigid or flexible structures; however, the gap between the critical *Ri*s decreases with an increase in aspect ratio. Drag experienced by the body is also studied. As the *Ri* increases, the mean drag coefficient also increases due to the increase in heat transfer for a body at rest. However, for a body in motion, the coefficient of drag is decreased to a local minimum at the critical *Ri* since the motion’s contribution to the drag is greater than the contribution of the heat transfer. A maximum drag reduction of 44% was found for an aspect ratio of 2 at the critical Richardson number.

Acknowledgments

I would first like to thank my thesis advisor Dr. Anthony Palazotto of the Department of Aeronautics and Astronautics at the Air Force Institute of Technology. The door to Prof. Palazotto's office was always open, and his student-first mentality, guidance, and passion for research has been essential to the success of this thesis.

I would also like to thank Dr. Hui Wan of the Department of Mechanical and Aerospace Engineering at the University of Colorado, Colorado Springs. Dr. Wan's prior research paved the way for the research completed in my thesis. Despite his relocation to Colorado, Dr. Wan has never failed to provide me the guidance and knowledge I required. I am gratefully indebted to his dedication to the completion of my research.

I would also like to thank Dr. William Baker of the Department of Mathematics and Statistics at the Air Force Institute of Technology. I was taught that every good engineer should find a mathematician to keep them in check, and I thank you for your expertise is this role help you have provided to the research effort.

I would also like to acknowledge Dr. Soumya Patnaik of the Air Force Research Labratory as the sponsor to the research in this thesis. I thank you for your vital recommendations and support for my thesis.

Finally, I must express my very profound gratitude to my parents and to my wife for providing me with unfailing support and continuous encouragement throughout my educational career and the process of researching and writing this thesis. Your help has been beyond words. I love you guys.

Capt Jeffrey DesRoches

Table of Contents

List of Tables

List of Figures

Nomenclature

A	reference area (typically associated with the cross-sectional area)	$A_{ellipse} = \pi ab\ (length^2)$
$A_{x,y}$	Amplitude of centroid translation along the *x*-axis and *y*-axis respectively	(distance/D)
a	half the major diameter of an ellipse	(length)
AR	aspect ratio	a/b
b	half the minor diameter of an ellipse	(length)
c	damping coefficient	
CFD	computational fluid dynamics	
C_D, C_y	fluid-dynamic coefficient associated with the force in the *y*-direction—also known as the coefficient of drag	$\frac{2F_y}{\rho_f v^2 A}$
C_L, C_x	fluid-dynamic coefficient associated with the force in the *x*-direction—also known as the coefficient of lift	$\frac{2F_x}{\rho_f u^2 A}$
$\overline{C_L}, \overline{C_D}$	mean lift and drag coefficients	
c_p	specific heat capacity (constant pressure)	
D	diameter, major diameter, or hydraulic diameter	(length)
DOF	degrees-of-freedom	
DSI	desynchronization vortex shedding regime I	
DSII	desynchronization vortex shedding regime II	
F_i	directional component of force	
f_{vac}	the natural frequency measured in vacuum	$\frac{1}{2\pi}\sqrt{k/m}$ (Hz)
f_{com}	common frequency at which synchronization or lock-in occurs at a given *Re*—i.e. $f_{ex}=f_{com}$	$\frac{1}{2\pi}\sqrt{k/(m+\Delta m)}$ (Hz)

f_{ex}	the forced or self-excited frequency of oscillation of a body	(Hz)
f_{st}	vortex shedding frequency of a body at rest—also known as the Strouhal frequency	(Hz)
f_{vs}	vortex shedding frequency of a body in motion—associated with flexible bodies	(Hz)
g	acceleration due to Earth’s gravity	9.81 (m/s^2)
Gr	Grashof number (diameter as length scale)	$\frac{g\beta(T_s - T_\infty)D^3}{\nu^2}$
IB(P)	initial branch (periodic)	
IB(QP)	initial branch (quasi-periodic)	
k	stiffness (spring) coefficient	
k_t	thermal conductivity	
LB(P)	lower branch (periodic)	
LB(QP)	lower branch (quasi-periodic)	
LSOR	Line Successive Over Relaxation	
m	mass of the body or solid	$A\rho_s$ (mass)
Δm	added mass	$m[(f_{vac}/f_{ex})^2 - 1]$ (mass)
M_{red}	reduced mass	$\frac{m}{(\rho_f\, D^2)}$
p	kinematic pressure	(force/length^2)
Pr	Prandtl number	$\frac{\upsilon}{\alpha}$
PSD	power spectral density	
Q_i	directional component of position	
Re	Reynolds number (arbitrary length scale “L”)	$\frac{\rho_f LU}{\mu}$
Re_D	Reynolds number (diameter as length scale)	$\frac{\rho_f DU}{\mu} = \frac{UD}{\nu}$

Ri	Richardson number	$\frac{Gr}{Re^2}$
Ri_c	critical Richardson number	
RMS	Root Mean Squared	$x_{rms} = \sqrt{\frac{1}{n}(x_1^2 + x_2^2 + x_3^2 \ldots + x_n^2)}$
S	vortex separation distance	(distance/D)
SS	Steady State vortex shedding regime	
St	Strouhal number	$\frac{f_{st}D}{U}$
T	temperature	(K or ^{o}R)
T_s	temperature at the body's surface	(K or ^{o}R)
T_∞	freestream fluid temperature	(K or ^{o}R)
U	freestream flow velocity	(length/time)
U_{red}	reduced velocity	$\frac{U}{f_{ex}D}$
u, u*	total velocity vector of a fluid particle (*dimensionless)	(length/time), ([length/time]/U)
u, u^*	velocity component in the *x*-direction (*dimensionless)	(length/time), ([length/time]/U)
v, v^*	velocity component in the *y*-direction (*dimensionless)	(length/time), ([length/time]/U)
VIV	vortex-induced vibrations	
x	axis in three dimensional reference frame associated with the direction of body translation	
y	axis in three dimensional reference frame associated with the direction of freestream flow	
z	axis in three dimensional reference frame associated with the length of the rod	
α	thermal diffusivity	$\frac{k_t}{\rho_f c_p}$ (length^2/time)

β	coefficient of thermal expansion	
ζ	damping coefficient	
θ	non-dimensional temperature	$\frac{T - T_\infty}{T_s - T_\infty}$
μ	dynamic viscosity	(force/length^2)
ρ_f, ρ_s	density (fluid and solid respectively)	(mass/length^3)
τ	shear stress	(force/length^2)
υ	kinematic viscosity	$\frac{\mu}{\rho}$ (length^2/time)
$\boldsymbol{\omega}$	vorticity	$\nabla \times \boldsymbol{u}$ (Hz)
2-D	two-dimensional	
3-D	three-dimensional	

Key Terms Defined

active suppression	VIV suppression methodology which requires a directed energy input to the system
bluff-body	A body that, when subject to an external flow, experiences flow separation due to its geometry.
critical Richardson number	Optimum value of the Richardson number where the vibrational amplitude is reduced to a threshold where the motion is deemed negligible and the drag cost is minimized. Richardson numbers greater than Ri_c come with a significant increase drag cost for minimal increases in suppression.
flexible-region	Occurs when the excitation frequency of the body in fluid does not align with the frequency of the external, fluid-dynamic forces due to the body being overly flexible. The fluid-dynamic forces and motion are completely out of phase.
lock-in region	Also known as the resonance and synchronization region. Occurs when the excitation frequency of the body in fluid closely aligns with the frequency of the external, fluid-dynamic forces.
passive suppression	VIV suppression methodology which utilizes modifications to the bluff-body geometry or by adding neighboring bodies near the bluff-body in question.
Reynolds number	Dimensionless number that is the ratio of inertial forces to viscous forces. This value helps determine if the boundary layers will be laminar, turbulent, or if the flow will separate.
Richardson number	Dimensionless number that is the ratio of the natural convection relative to the forced convection.
stiff-stiff region	Occurs when the excitation frequency of the fluid-immersed body does not align with the frequency of the external, fluid-dynamic forces due to the body being overly rigid. The fluid-dynamic forces and motion are in phase.
Strouhal number	Dimensionless number that describes the separation frequency within the vortex shedding regime for a fixed body.
vortex-induced vibrations	Vibrational motion of a flexible structure due to asymmetric, periodic, fluid-dynamic forces imposed in the body surface from an external flow.

vortex shedding	Flow separation mode where two coupled, opposing vortices form in an oscillatory manner at opposite sides of the aft end of the bluff-body. The vortices completely detach from the body and are swept downstream while new vortices form along the body in their place.

I Background

1.1 Overview

This research is directed to the study of vortex-induced vibrations in which an elliptical cross section is considered. The effect of the flow's ability to cause the cross sectional vibration is studied. The cross section's surface is heated to a uniform temperature and the ability to suppress the vortex-induced vibrations is evaluated.

The problem of vortex-induced vibrations (VIVs) involves a fluid interaction with a flexible body. Suppose a uniform flow field is imposed upon an infinitely long, slender cylinder. The direction of the freestream is perpendicular to the length of the cylinder. The cylinder is considered infinite so that the boundary conditions can be ignored. This assumption will be justified in Chapter II.

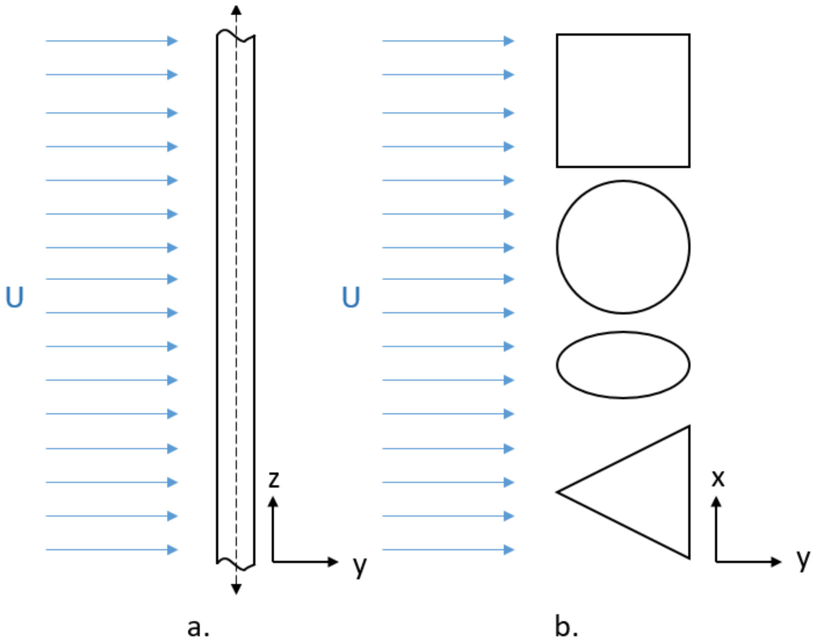

Figure 1. a) Side profile of an infinitely long cylinder subject to a uniform flow field. b) Cross-sectional view of the cylinder with examples of common cross-sections studied. The y-direction is parallel to the flow field. The x-direction and z-direction are both perpendicular to the flow. The z-direction is parallel to the un-deformed center line (dashed) running along the length of the cylinder. *U* and the blue arrows represent the freestream velocity and flow field.

The cylinder may have any cross section, but some are more applicable than others. Figure 1 demonstrates the physical setup described, along with some sample cross sections commonly studied. Mechanical, civil, ocean, and aeronautical engineers all have had a vested interest in the study of VIV. Studies include characterizing, suppression, and the utilization of this phenomenon. There are many physical applications of this research, such as: heat exchangers, aircraft control surfaces, ocean risers, bridges, power lines, offshore structures, tow cables, chimneys, pipelines, and many other aerodynamic and hydrodynamic applications [1]. Figure 2 (below) demonstrates some physical applications for VIV research. Circular bluff-bodies remain the largest focus of these studies, due to their increased relevance from manufacturing ease and application—pipes, wires, cables, columns, etc. However, rectangular, triangular, and elliptical, and various other bluff-bodies are also studied. Research opportunities in vortex shedding and VIV are virtually endless. Many parameters have been considered in these studies, and many others, and the combinations thereof remain unexplored both experimentally and computationally.

The rod in the flow field is subject to fluid-dynamic forces. Like all real structures, the cylinder has some finite rigidity, and would flex to the fluid-dynamic forces it experiences. The problem is time-dependent since flow characteristics, such as boundary layers, develop over time. The combination of flows and structures of interest are those resulting in flow separation at the aft end. For example, a thin plate oriented such that width of the plate was parallel to the freestream flow field would likely not demonstrate separation; however, other shapes, known as bluff-bodies, are likely to demonstrate flow separation due to sharp corners or curvature at the aft end. The separation is due to an adverse pressure gradient and backflow of the fluid of the aft end.

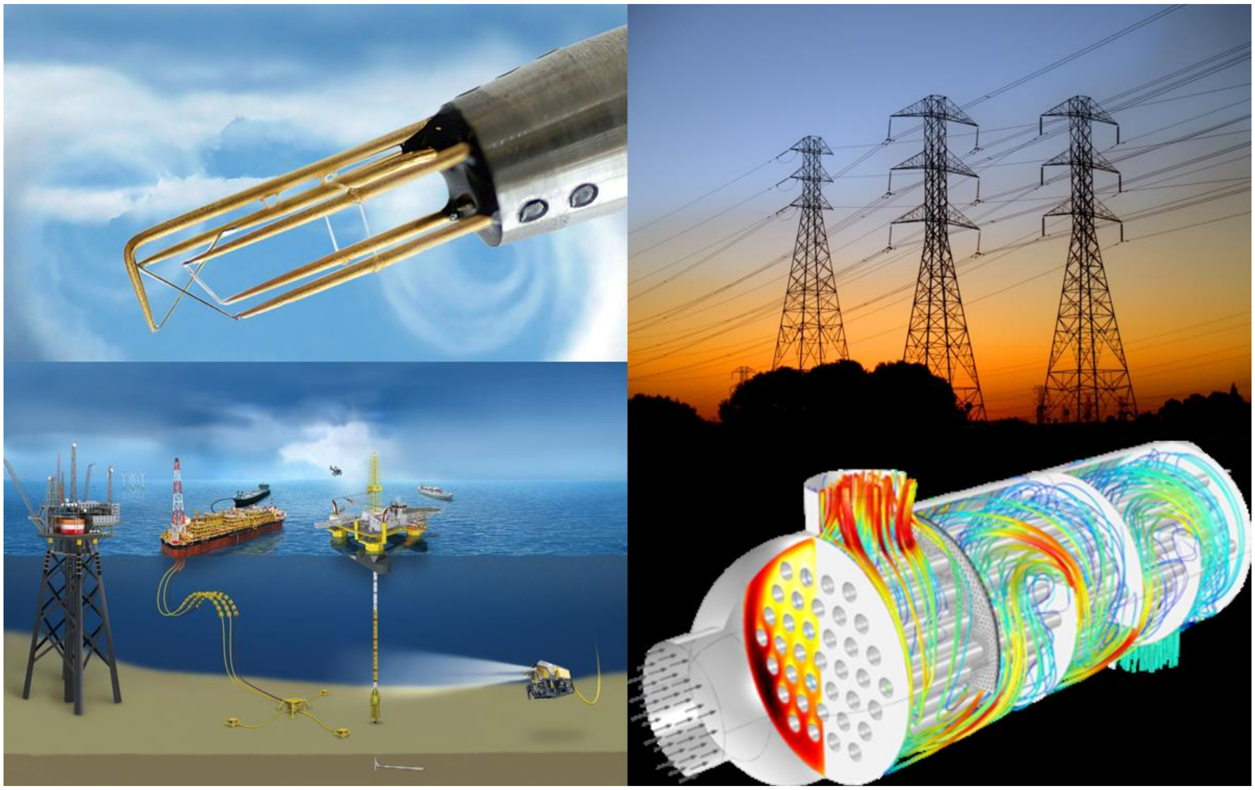

Figure 2. Applications of VIV studies. (Top-left) hotwire anemometer. (Top-right) power lines and towers. (Bottom-left) Ocean risers and drilling platforms. (Bottom-right) shell and tube heat exchanger. Each application involves a long slender body (or bodies) subject to a fluid flow field.

Given the right flow conditions, the separation occurs in a periodic manner and will cause the structure to vibrate. To many structures, vibrations are adverse to the integrity or function of the product, so it is desired to find ways to suppress, or eliminate them. The goal of this thesis is to observe if a uniform, elevated temperature boundary condition at the cylinder's surface can alter the flow in the way that eliminates periodic separation. An elliptic, slender, three-dimensional (3-D) cylinder is reduced to a two-dimensional (2-D) cross section with various aspect ratios (AR). The cross section will be elastically mounted by treating the body as a mass-spring system that is allowed to translate to replicate a slice of a beam undergoing bending deformation. An exaggerated illustration of this concept is shown in Figure 3 below.

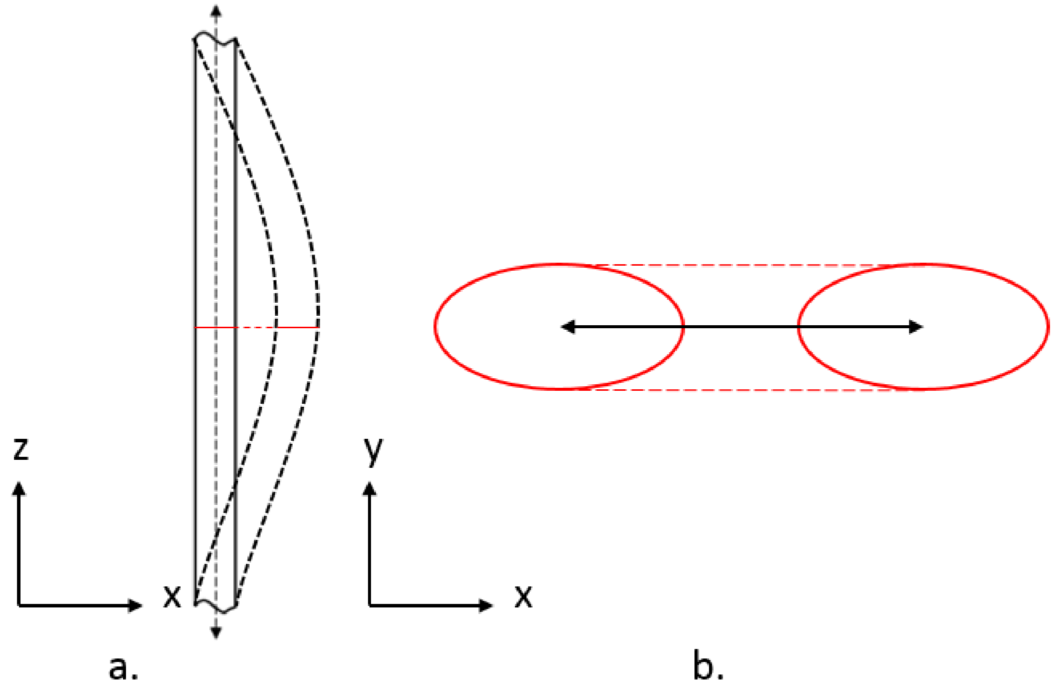

Figure 3. a) Side view of a 3-D slender beam undergoing exaggerated bending. The red line shows a sample of where the 2-D cross section is taken. The dark, dashed lines show the deformed beam. b) Top-down view of the cross section translating in the x-y plane due to bending. Note: any bending mode is applicable.

1.2 Vortex Shedding

The vortex shedding phenomenon at the aft end of bluff-bodies has been thoroughly researched and investigated since the late 1800s [2]–[5]. Sarpkaya (2004), who's work with VIVs stretched back to the 1960s defines a bluff-body as:

> [A]n elastic or elastically mounted fore-and-aft body of proper mass, material damping, and shape whose cross-section facing the ambient flow at high-enough Reynolds numbers gives rise to separated flow and hence to two shear layers, which interact with each other and bound an unsteady wake[1], p4].

Circular cylinders are the most studied bluff-body; however, squares, triangles, and other bluff-body shapes have also been considered [1]. Additionally, most of the research has been focused in the laminar regime with low Reynolds number (*Re*) flow. Typically, the *Re* is high enough to ensure separation at the aft end of the body, but not such that turbulence occurs. Specifically, for flow around circular cylinders, separation occurs towards the aft edge creating predictable, oscillating, vortex formation [6]. Circular cylinders are one sample bluff-body which demonstrates clear vortex shedding. Higher *Re* flows tend to produce unpredictable turbulence that lack defined vortex formations. Although highly encouraged by Sarpkaya's recommendations for future research considering high *Re* flows, this will not be the focus of the present research [1]. Figure 4. demonstrates the different flow regimes for a circular cylinder as a function of *Re*.

In both the "bound vortex" and "vortex shedding" regimes shown in Figure 4, a zero-shear line occurs between the vortices formed on each side of the aft end and marks the location of what is known as the shear layer [1]. This shear layer is developed from the velocity gradient in the viscous fluid the two bound vortices. The line of zero shear is most clearly shown as the red-dashed streamline running between the two bound vortices in the top right illustration of Figure 4. A similar streamline exists in the vortex shedding regime; however, the location on the aft end shifts in an oscillatory manner and follows a contour between the opposing vortices. This can be seen in Figure 5 below. At the aft end of the elliptical cross section, a white line exists between the red and blue areas of rotation. While the bound vortex zero-shear line is at the center of the body in Figure 4, the point where zero-shear line is found in Figure 5 is definitively lower than the midpoint of the aft section. The point where the line meets the body will continue to move as the vortices alternate in formation.

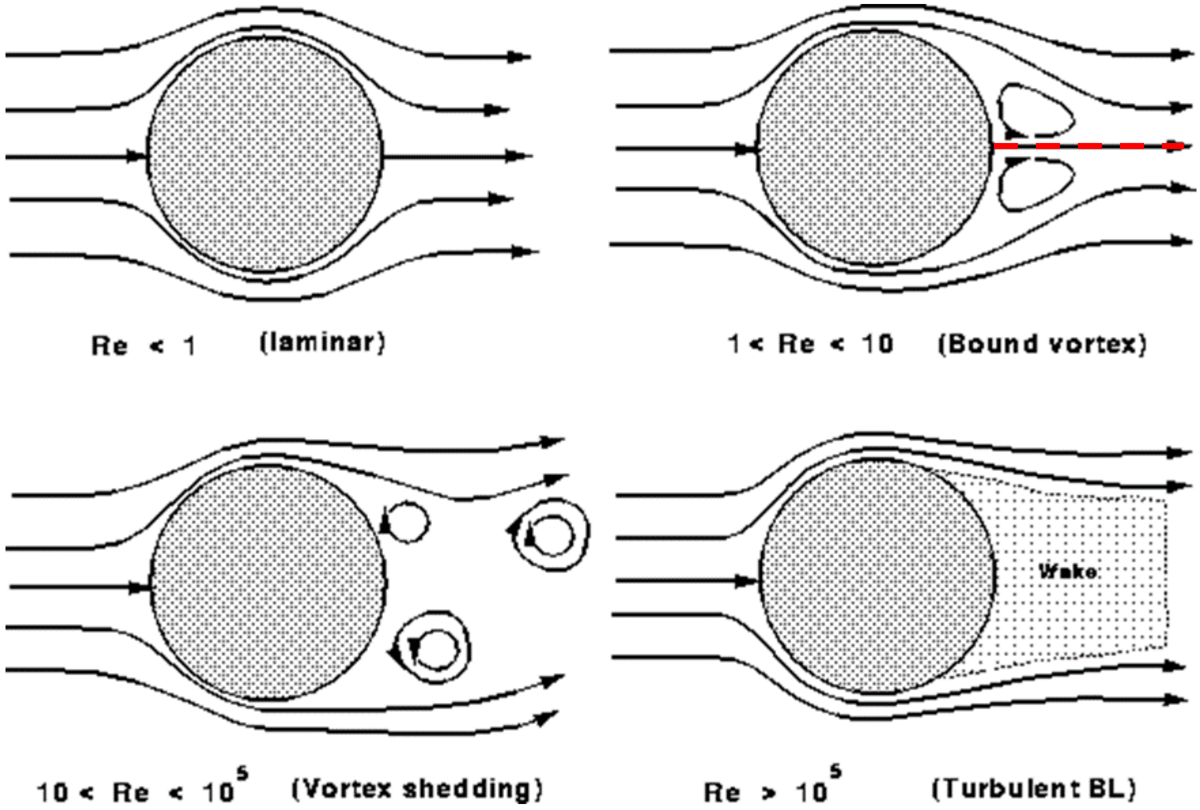

Figure 4. Flow regimes as an approximate function of the Reynolds number for a circular cylinder. The arrowed lines are stream lines. (Top-left) Laminar region where the flow remains completely attached to the body. (Top-right) Laminar region where separation occurs at the aft end, resulting in two, symmetric, bound vortices. (Bottom-left) Regime of interest where vortex shedding—laminar region where the separation point has shifted fore and non-symmetric are formed in an oscillatory manner. (Bottom-right) Turbulent boundary layer formation [1].

Among the first to study this phenomenon, Strouhal (1878) found a relationship between the shedding frequency of a fixed body (f_{st}) and the *Re* Relationship [2]. This relationship was later reduced to the non-dimensional parameter known as the Strouhal number (*St*) as shown in Eq 1. *D* is the hydraulic diameter of the bluff-body and *U* is the freestream velocity of the fluid.

$$St = \frac{f_{st} D}{U} \tag{1}$$

As each vortex grows at the body surface, they inevitably separate from the body and a new vortex forms in its place. The vortex formation on one side of the aft end is coupled with the vortex formation on the opposing side. This processes repeats in an alternating, periodic manner near the aft end of the bluff-body. The seminal works of Strouhal and others, like Bérnard (1908) and Von Kármán (1911), characterize this observation, and it is now known as the Bérnard-Kármán vortex street [3]–[5]. A typical vortex street is shown in Figure 5.

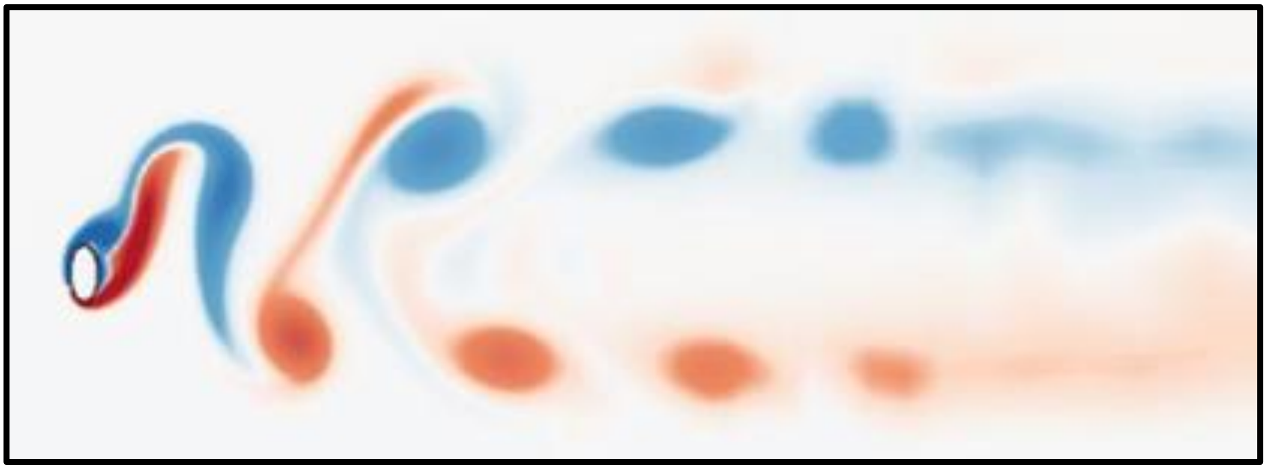

Figure 5. Visualization of the Bérnard-Kármán vortex street from a 2-D, elliptical bluff-body. Flow is from left to right and the body is allowed to translate along a vertical axis, perpendicular to the flow and passing through the body's centroid. Image is produced using an in-house CFD solver.

1.3 Vortex-Induced Vibrations

Most of the original research in vortex shedding focused on characterizing the wake of the fluid downstream of a rigid, bluff-body; however, simulations that relate to physical applications demand a fluid and flexible body interaction. This has brought about the study coined as vortex-induced vibrations. The primary goal of studying VIVs is finding ways to suppress them. In vortex shedding regime, periodic lift and drag forces act on the surface of the body as the vortices are shed. The fluid-dynamic forces reach a periodic steady state that oscillates at a nearly equal frequency. For a stationary body, this frequency is f_{st}; however, f_{vs} will denote the shedding frequency of a body in motion. These two frequencies will slightly differ for the same cross section and *Re* [1].

According to Sarpkaya, the excitation frequency of an elastically mounted body in a fluid (f_{com}) differs from its natural frequency in a vacuum (f_{vac}) [1]. Eq. (2-3), below, demonstrate how these two frequencies differ. In these equations, k is the stiffness (spring) coefficient, m is the mass of the body, and Δm is the added mass. The added mass is a function of the shape, orientation, physical surroundings of the body, the viscous fluid motion—the latter being the largest factor and the most variable over time. Therefore f_{com} is variable, and can only be solved *a posteriori* and needs experimental or computational data to find exactly [1]. Eq. (4) shows how the added mass can be found.

$$f_{vac} = \frac{1}{2\pi}\sqrt{\frac{k}{m}} \tag{2}$$

$$f_{com} = \frac{1}{2\pi}\sqrt{\frac{k}{m + \Delta m}} \tag{3}$$

$$\Delta m = m\left[\left(\frac{f_{vac}}{f_{ex}}\right)^2 - 1\right] \tag{4}$$

When the frequency of the external fluid-dynamic forces (f_{ex}) matches f_{com}, the structure may be subject to large translational amplitudes. These large amplitudes in motion may result in the failure of the structure or the optimal opportunity to generate energy, and it is these ends that have motivated the research in this field.

It is not uncommon for f_{ex} and f_{com} to closely align. This is known as the lock-in/resonance/synchronization region. Given a bluff-body shape that is prone to VIVs, there exist a range of parameters where the lock-in region occurs. The reduced mass (M_{red}), commonly seen as m^*, reduced velocity (U_{red}), *Re*, and the damping factor (ζ) are the most prevalent non-dimensional parameters used to characterized a fluid flow/bluff-body coupling. These parameters Eq (5–8) are as defined in Wan and Patnaik (2016) and will be used in the study conducted in this thesis [7].

$$M_{red} = \frac{m_{body}}{\rho_{fluid}\, D^2} \tag{5}$$

$$U_{red} = \frac{U}{f_{vac}\, D} \tag{6}$$

$$Re = \frac{U\, D}{\nu} \tag{7}$$

$$\zeta = \frac{c}{2\sqrt{k\, m}} \tag{8}$$

In these equations, m_{body} (or m) is the mass per unit length of the bluff-body, U is the free stream velocity and D is the characteristic length of the body (the diameter for a circle, major axis length for an ellipse, or hydraulic diameter for any given bluff-body). Constants k and c and the spring and damping coefficients as seen in Eq. (9)). Index i indicates the directional component of Q (position) and F (external force) in the directions of motion. In this particular problem setup, Q will be the translational displacement of the body's centroid from its position at rest and F will be the lift force [7].

$$m\frac{d^2Q_i}{dt^2} + c\frac{dQ_i}{dt} + k\, Q_i = F_i \tag{9}$$

As noted in [1], most experimental and computational research in this field reduces a six-degree-of-freedom (DOF) physical body to a one-DOF representation. A model of this is shown in Chapter II. This is done since the most significant amplitudes are found in the direction perpendicular to the flow. Therefore, the models that allow the body to move typically restrict the motion to translation perpendicular to the flow (x-axis). Depending on the body, some models also allow for translation parallel to the flow (y-axis) and rotation about the axis passing through the centroid, parallel to the length of the cylinder (z-axis). This will be the axis system used to describe the following research.

Research of VIVs is conducted both with physical experimentation and with Computational Fluid Dynamics (CFD). Most work prior to 1990 was done experimentally, but computational simulations have since increased in representation. These simulations are both conducted in 2-D and 3-D. Analytical work is limited in this field due to the non-linearity in the governing equations and highly unpredictable nature of flow separation and turbulence, especially once complex geometry and multiple bodies are introduced.

Great strides have been made in the field of VIVs as many cylinder shapes have been investigated. However, limited research has been done on the characterizing and suppression of elliptical cross sections. This gap in research has influenced the decision to make elastically-mounted elliptical cylinders the focus of this research. Navrose, Yogeswaran, Subhankar, and Mittal (2014) simulated and characterized the free vibrations of elliptic cylinders from varying aspect ratios (AR) between 0.7 and 1.43 [8]. Their work will serve as a baseline for finding and characterizing the lock-in region and will be covered more in-depth in the following section.

1.4 Vortex Shedding Regimes

The lock-in region is of particular interest for VIV research. Each cross-section and *Re* combination must be tested to have a complete understanding of the fluid-structure interaction for a flexible body. The lock-in region is associated with the natural frequency, which is governed by the mass and stiffness of the structure. To find the lock-in region, researchers have fixed M_{red} and varied U_{red} since U_{red} determines f_{vac} (refer back to Eq. 6). The following discussion demonstrates how the lock-in region can be determined based on experiments or computational simulation.

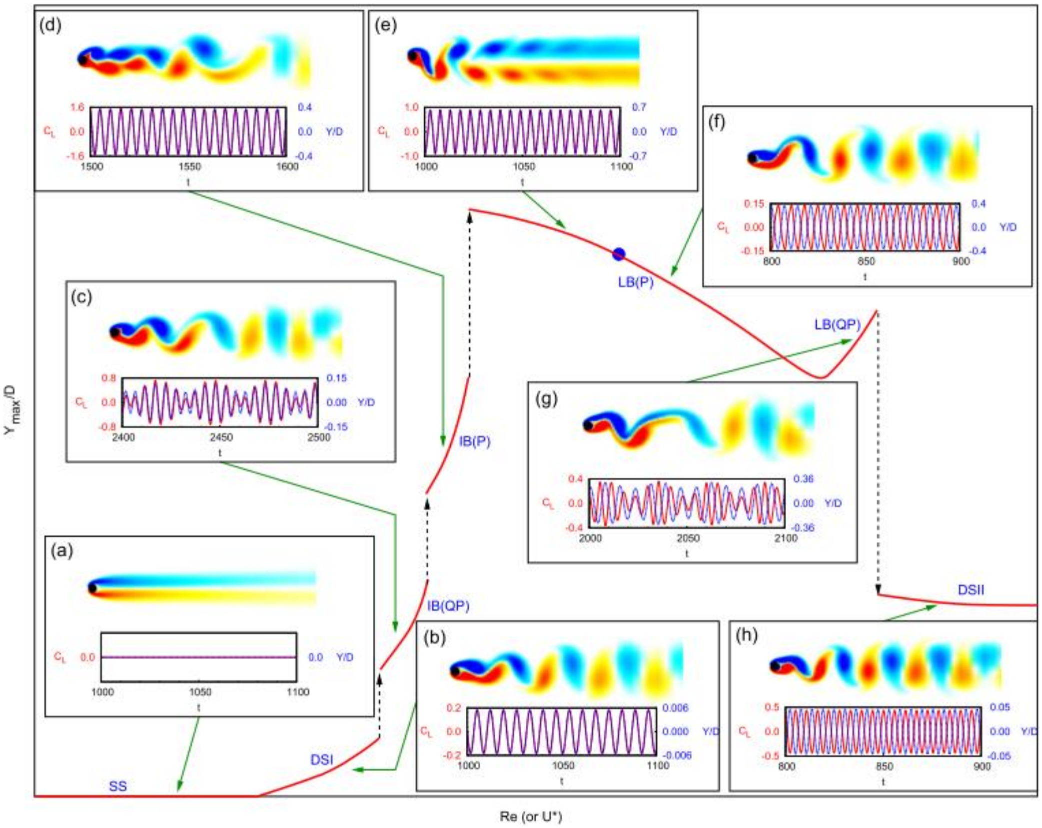

Figure 6. The different flow-regimes/branches for a freely vibrating cylinder of AR=1.11 are shown here schematically. The primary plot is the vibrational amplitude vs *U. The subplots(a-h) show the following regimes: (a) SS - steady state, (b) DSI - desynchronization regime I, (c) IB(P) - initial branch (periodic), (d) IB(QP) - initial branch (quasi-periodic),**

(e-f) LB(P) - lower branch (periodic), (g) LB(QP) - lower branch (quasi-periodic) and, (h) DSII - desynchronization regime II. [8]

Navrose, Yogeswaran, Sen, and Mittal (2014) conducted a thorough investigation of elliptical cylinders between $0.7 \leq \mathrm{AR} \leq 1.43$ for $60 \leq Re \leq 140$ with either the major or minor axis aligned with the freestream flow [8]. Their model was elastically mounted in 2-DOF and had a M_{red} of 10. The bodies in this studies experienced VIVs, making these parameters suitable as a baseline for comparing the expanded AR range in the present research.

A significant portion of their paper is classifying the different flow regimes as they vary U^* (U_{red}) and Re by increasing and decreasing the flow velocity. It is important to note this method of changing U_{red} as opposed to varying f_{vac}. Their analysis is useful for validating the model produced for the present research as the same regimes should be exhibited in the unheated simulations. In order to make any comparisons, the vortex shedding regimes and how they are determined must be well understood. Figure 6, above, demonstrates the different branches experienced by ellipses as U_{red} is varied.

The first regime (a) is the steady state regime (SS) and is only considered when the Re is too low for vortex shedding to occur. This region precedes vortex shedding and no oscillation of the body or fluid is observed. This region essentially the desired end state when full VIV suppression is achieved. This regime will not be found in the model used in the present research since the Re will be fixed at 100 unless the AR is sufficiently small (the width of the ellipse perpendicular to the freestream is small).

In the desynchronization regime I (DSI) shown in (b), the body undergoes a small oscillation from vortex shedding. In this regime, the body is significantly stiff relative to the fluid forces acting on it, limiting the motion. The frequency of the vortex shedding is not aligned with the natural frequency of the elastically-mounted body—hence the term desynchronization; however, the forcing function is in phase with the motion of the body. This may be seen by comparing the transient coefficient of lift with the motion. As seen in figure (b), the red curve depicting C_L and the blue amplitude curve are overlapping. Note, the plot has separate axes for each dependent variable. Another means to determine phase is to plot the two dependent variables against each other. A positive slope with little variance from the trend line indicates the two are in phase, while a negative slope shows out of phase.

Plots (c) and (d) show the initial branches (IB). The initial branch quasi-periodic IB(QP) and periodic IB(P), are named after the onset of the lock-in region. The IB(QP) regime (c) demonstrated a pronounced beating in the lift signal. This is due to the natural frequency influencing the signal in addition to the shedding frequency. This may be revealed under a power spectral density (PSD) analysis. A PSD indicates how influential a given frequency is on a random signal. If the C_L signal is analyzed in this way, the predominant frequency can be considered f_{vs}. Figure 7 demonstrates how the results from a PSD analysis. A peak also develops around f_{vac} for a simulation in the IB(QP) regime. In the IB regions, the body is stiff, limiting the amplitude of the oscillation. The IB(P) (d) is found in close proximity to the alignment of f_{vs} and f_{com} and the beating has ceased. The body is still stiffer than the natural frequency so the amplitudes are less than when perfect alignment is achieved. The forcing function is in phase with the motion.

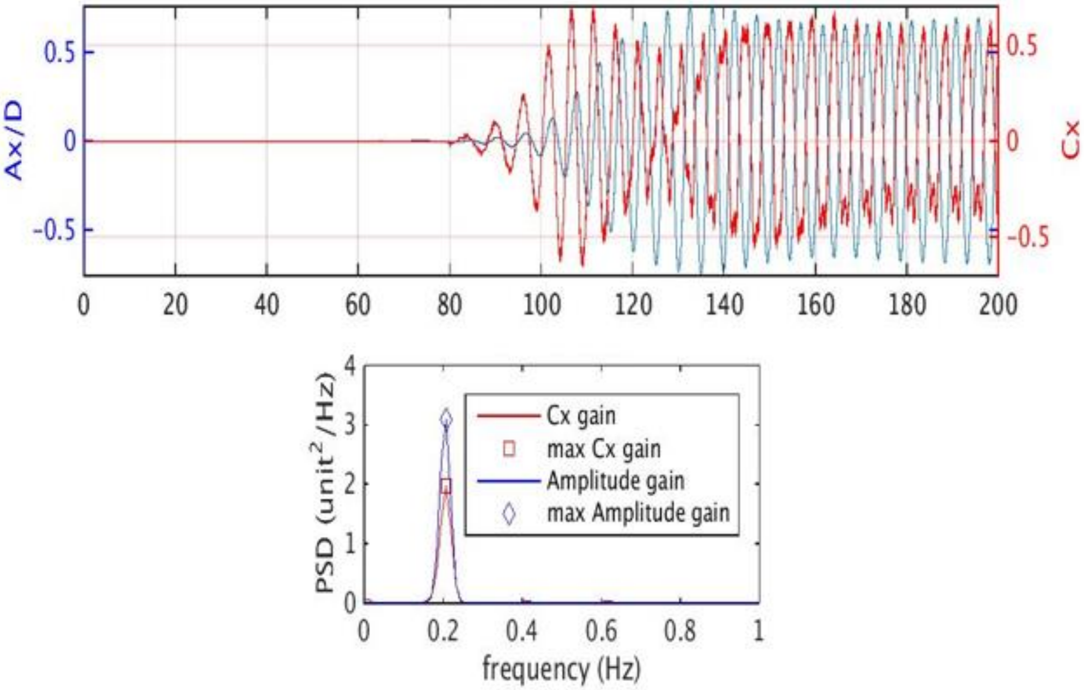

Figure 7. (Top) Sample transient amplitude in blue and transient lift coefficient in red. (Bottom) Sample PSD plot of the shown amplitude and lift coefficient curves. The peak value determines the most influential frequency present in the signal. The frequency found in this way for the amplitude is f_{ex} and the frequency for the lift coefficient is f_{vs}.

The lock-in regime (e-g) is associated with the lower branch (LB), and also has a quasi-periotic (QP) and periodic (P) region. The beginning of the LB region is denoted by the point of peak amplitude. This is where $f_{vs} = f_{com}$. The phase and frequency are aligned starting at the beginning of the LB(P) (e). As the body becomes more flexible, the lift force and motion fall out of phase, which gradually reduces the amplitude. This phenomenon was also recorded by Prasanth and Mittal (2008) [9]. This phase angle is found to reach 180° near the middle of the lock-in region (f). In the LB(QP) region beating occurs due to the presence of harmonics. To conduct a suppression analysis, it is best to find the U_{red} associated with the beginning of LB(P) as it represents the worst-case scenario for structural vibrations. However, all points in the LB(P) region have high amplitudes and would be sufficient to prove suppression.

Lastly, (h) the desynchronization regime II is observed (DSII). In this regime, the body is now considered flexible and the frequencies are no longer aligned. Additionally, the lift and motion signals are out of phase. Despite these factors, the amplitudes are higher than the DSI regime since the body is flexible and easily moved. This is also a region of interest since this region represents a large band of probable flow regimes as the *Re* increases.

Understanding these regimes is instrumental in characterizing the responses for each AR studied in the present research prior to adding thermal effects for suppression. Suppressing in the lock-in and flexible regions are important outcomes needed by engineers for design purposes and will be an emphasis in the results in Chapter IV. Wan and Patnaik (2016) use these two regions in their study for thermal effects on a circular bluff body, and laid out the basis for suppressing elastically-mounted, elliptical bodies [7].

1.5 Suppression Methodology

As previously stated, the primary goal of studying VIVs is finding ways to suppress them. In many instances, it is desired that VIV be suppressed in order to prevent fatigue and structural failure, preserve function, or maintain certain downstream flow conditions. A secondary objective is to study how the changes to the system affect the drag coefficient (CD, Cy). In many cases, suppression is achieved at the cost of increased drag, so a solution which increases drag the least is ideal.

There are two major suppression categories—active and passive. Passive methods rely on the geometry of the bluff-body itself or the use of additional control bodies. Passive methods do not rely on any directed energy to achieve suppression. Conversely, active suppression relies on additional energy input to alter the flow around the bluff body. Active methods include the use of jets, body rotation, acoustic control, and thermal effects. Examples of these methods will be discussed later in this chapter. Both passive and active methods of suppressing VIV have been deeply researched. Each method comes at some cost such as energy consumption, increased drag, function degradation, or manufacturing difficulty. Researchers in the VIV field use both experimental and computational models to validate the effectiveness of these methods [6].

The different methods also find their prominence in different flow parameters—namely air versus water, omnidirectional or unidirectional flow orientation, and high *Re* versus low *Re*. Omnidirectional solution allow the freestream to change direction within the *x*-y plane. Unidirectional solution rely on a fixed freestream direction. Bearman and Branković (2003) conducted experiments comparing circular cylinders with strakes (wide fin-like protrusions) and bumps taken from applications in air and attempted to apply them to water [10]. While these designs showed good results in air, suppression was limited for the channel flows tested in water. Rashidi, Hayatdavoodi, and Esfanhani (2016) presented a comprehensive review of these vortex shedding methodologies [11]. They provide a section specifically on suppression using thermal effects and conclude that more focus is needed in finding optimal solutions, which is a secondary goal of the research in this thesis.

1.5.1 Passive Suppression

Early experimental work in vortex shedding and VIV primarily focused on suppression by passive methods. Researchers explored various ways to alter the geometry of the bluff-body cylinders. Zdravkovich (1981), summarizes most of the previous research in this domain and brakes these geometry manipulations into three primary categories: surface protrusions, shrouds, and near-wake stabilizers [6]. Helical strakes, fins, studs, and spheres are examples of surface protrusions.

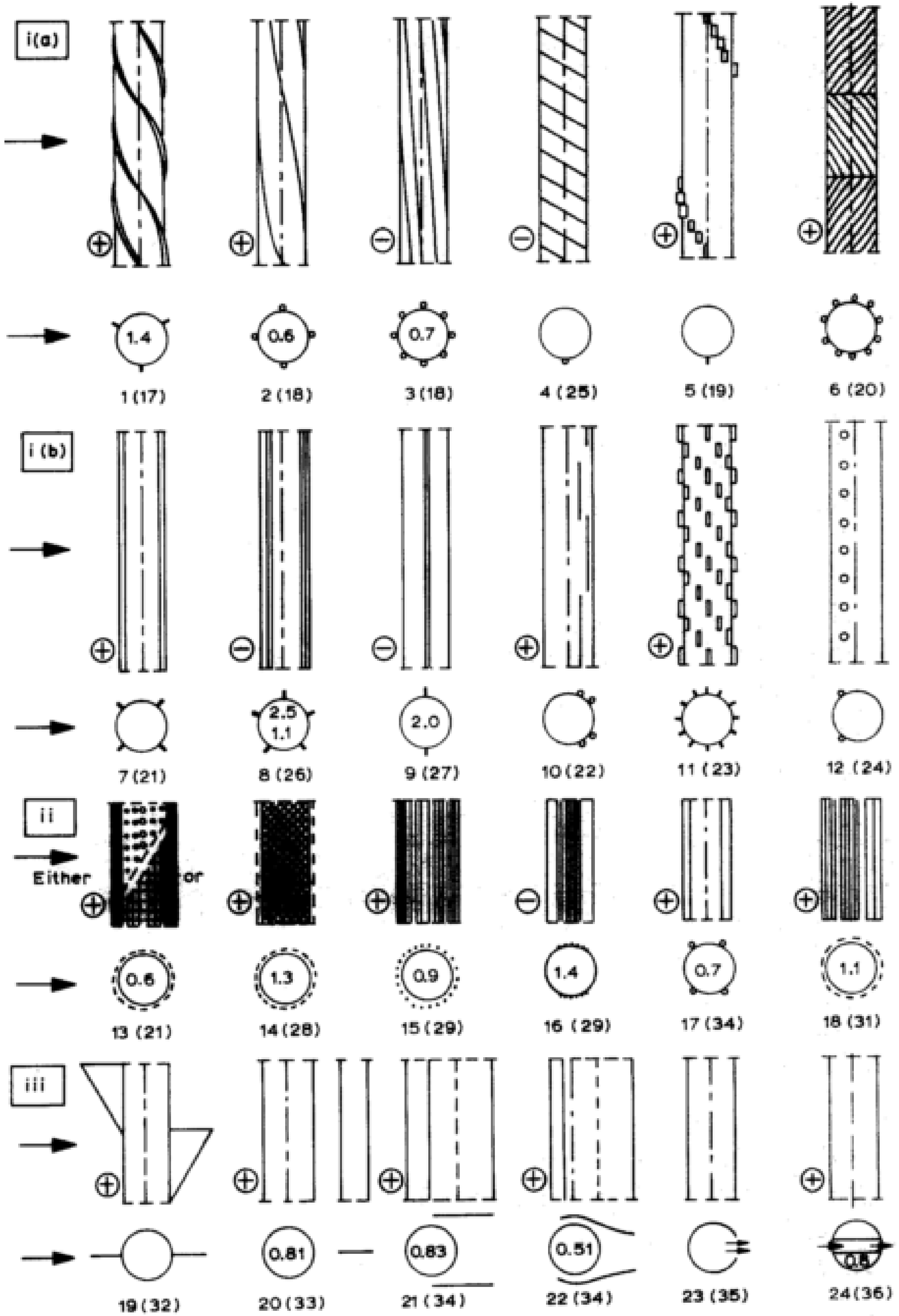

Figure 8. Passive VIV suppression categories (i) surface protrusions ((a) omnidirectional and (b) unidirectional), (ii) shrouds, (iii) nearwake (+ effective, - ineffective) [6].

Surface protrusion methods are predominantly omnidirectional, since their geometry makeup is not dependent on the flow direction. These applications target scenarios where the direction of the fluid and orientation of the body are subject to change. Shrouds are covers added to the cylinder that focus on entraining the fluid. Examples of shrouds include perforated layers, gauze, axial rods and axial slats. Like surface protrusions, shrouds are typically omnidirectional. Unlike the aforementioned methods, near-wake stabilizers are unidirectional. They prevent interaction of the entrainment layers and come in the form of splitters, plates, guiding canes, and slits [6]. Figure 8, above, shows pictorial examples for each of these categories.

1.5.1.1 Passive Suppression by Geometry manipulation

Since Zdravkovich's (1981) summary of the pioneering work with geometric alterations, several other have contributed to the field with focuses in various methods. The following are a few examples of research recently completed in this specific field.

Baek and Karniadakis (2009) conducted CFD studies of cylinders modified with a slit at the diameter, parallel to the flow. Their study sought to find the optimal slit width at Re = 500 and 1000. The slit produced a jet, which in turn leads to VIV suppression. The optimal slit width was different for each Re at 16% and 12% the diameter respectively. This is significant because the results show little suppression at 12% for the Re = 500 case.

Similar studies were conducted in experiments using air at a higher Re [12]. Continuing the trend from Baek and Karniadakis, the higher Re required a smaller slit for optimal suppression at 5% the diameter. The optimal suppression width decreased the amplitude by 81.78%, and was the highest suppression shown of the three cases. The minimum-drag width, however, was found at a much larger width, 14.64%. This example of a single method in different conditions demonstrates some of the difficulty for real-world planning and prediction as well as the tradeoff between suppression and drag.

Splitter plates are also an effective means of vortex shedding. Numerous researchers have investigated this topic with various nuances [6]. Soumya and Prakash (2017) computationally investigated the effectiveness of splitter plates for various elliptical shapes [13]. These simulations were conducted at low Re (50–200) with varying AR from 1.0–0.5. The model is limited by not allowing the cylinder to translate as a result of the lift and drag forces. The research is also limited by not investigated elliptical ARs greater than one. A significant aspect of [13] is its consideration of the shear layer interaction length. This consideration is important when trying to suppress VIVs by means of altering the separation point to get a solution more like the bound vortices found in Figure 4.

Splitters create a unique flow-recycling region when suppressing vortex shedding. The shear layer interaction length is the region where these opposing vortices are allowed to interact beyond the splitter plate. As *Re* and AR increases, the critical splitter length increased. This coincides with the desire for the flow to separate closer to the stagnation point of an elliptical bluff-body for higher *Re* and *AR.* Wu, Shu, and Zhao (2014) also investigated splitter plates for circular cylinders, but with the addition of the splitter being undulatory [14]. The splitter plate was forced to move in a wave-like motion, similar to that of a snake. The simulation was limited to a fixed, circular cylinder at a *Re* of 100. This method takes a traditionally passive method and adds an active element by forcing the splitter plate to undulate. Beyond providing another means of drag reduction and VIV suppression, this research is mentioned to emphasize the vast quantity of suppression methods and variations thereof.

Geometry manipulation methods have shown promising results and have been implemented on several real-world products such as chimneys and deep-sea risers, where an omnidirectional solution is required. However, not every application can allow for these changes to the body. Additionally, the high increases in drag may also be a drawback to certain applications such as a heat exchanger.

1.5.1.2 Passive Suppression by Control Bodies

Zdravkovich (1977, 1987, and 1988) also pioneered experimental research with multiple cylinders in tandem with various arrangements [15]–[17]. Figure 9 shows various configurations which have been considered in past research. This research is of particular interest since structures such as chimneys, columns, risers, and cables are commonly arranged among other similar objects. It is important for designers to know which configurations may increase the likelihood or amplitude of the VIVs to avoid critical failure of the structure. Alternatively, designs of these structures could be significantly improved if the special arrangement alone can reduce or completely suppress the forces from VIVs. Due to the significant relevance to this work and the numerous configurations that exist, copious research has been conducted in this area. For more information in this area both Sumner (2010) and Zhou and Mahbub (2016) conducted meta-analyses of past research [18], [19]. They included whether the work was experimental or computational, parameters considered, and a synopsis of discrepancies and significant trends. Although control bodies are not considered for thermal effect suppression, a constant theme of plotting C_D, C_L, and St against the different parameter changes is demonstrated throughout these studies and will be used when studying thermal effects. Control and multiple bodies would need to be strongly considered in heat exchanger or multi-axis anemometers design. There is no available research combining the effect of multiple bodies and thermal effects; however, this remains outside of the scope of the present research, as a baseline isolating thermal effects for a single elliptic cylinder is needed first.

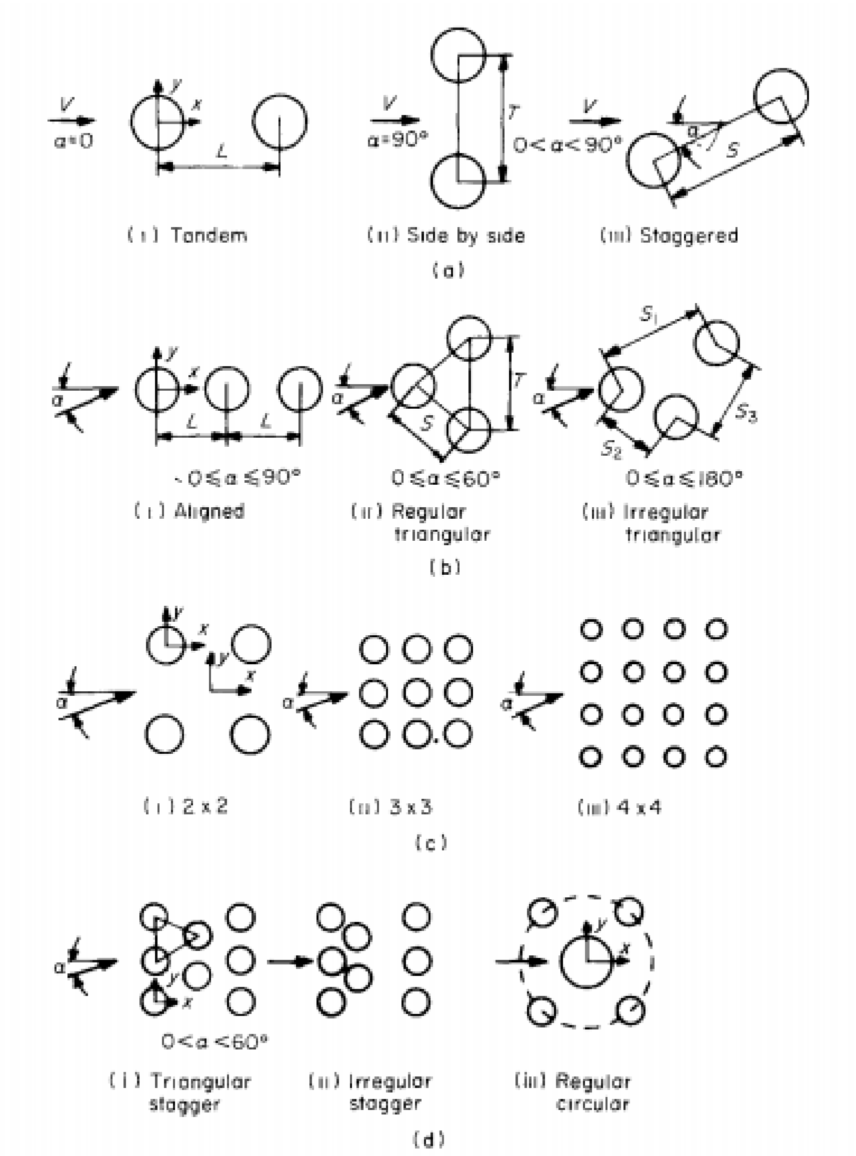

Figure 9. Passive suppression using various arrangements of multiple circular cylinders [16].

Although daunting, great strides have been made in the analysis and prediction of multi-body suppression. Meneghini et al. (2001) produced numerical simulations at low Re (100–200), which successfully replicated the results found in early experimental work [20]. Their simulations showed that the characteristics of flow for parallel, tandem cylinders change when the gaps (*L*) are greater than or less than 3*D*. When the L < 3*D*, suppression is achieved for the foremost cylinder. For side-by-side arrangements, the flow regimes changes at 2*D*. Suppression is never achieved for either cylinder; however, for L ≤ 2, a shedding phenomenon called *flopping* occurs. This is when the bodies seems to act as one and alternating vortices are shed from the outside edges of the two bodies. This phenomenon resulted in an increase in magnitude of the average lift forces [20].

Song, Duan, and Gu (2017) investigated the use of three control rods similar to the configuration shown in Figure 9-d-(iii) [21]. Their research numerically simulated the different angular configurations as well as gap spacing to the main cylinder. The focus of this study was on suppressing VIVs for the main cylinder. Their simulation allowed for two-DOF motion in the *x* and *y*-axis for the main cylinder.

Song et al. (2017) first took into account a rough baseline of an isolated cylinder's maximum amplitude at various U_{red} when $Re = 150$ which is shown in Figure 10 below. This curve is consistent with many other sources such as Wan and Patnaik (2016) and is a standard for finding f_{com} for dynamic models. In this case, $4 \leq U_{red} \leq 7$ represents the lock-in region where the frequencies align and the greatest amplitudes are found [7]. Typically, frequencies in this region are used to simulate the worst-case-scenario—in this paper, $U_{red} = 5$ is used. The later section on vortex-shedding modes examines this methodology. Their findings included a region exists for both angular orientation and gap distance where substantial VIV suppression occurs. This study is significant in that this configuration can effectively suppress vibrations from a third of possible flow directions, making it a semi-omnidirectional solution. The limitation of this study is that only a single *Re* was considered.

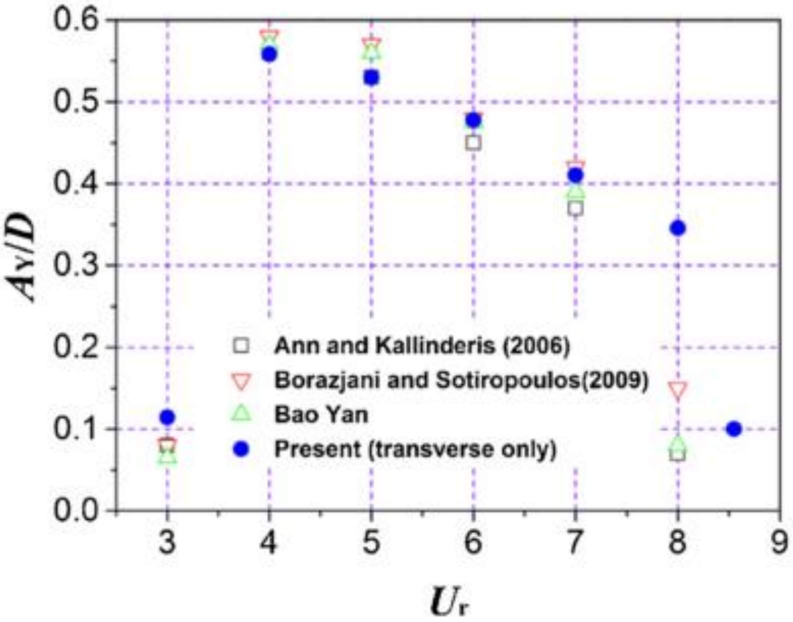

Figure 10. U_{red} **sweep for a fixed** M_{red} **(2) and** ***Re*** **(150) for a circular cylinder [21]**

At significantly higher *Re* (5000-50,000) Silva-Ortega and Assi (2017) experimentally investigated the addition of 2, 4 and 8 cylinders [22]. In addition to varying position, gap distance, and *Re*, They found that an eight control cylinder configuration produced the best results with a 99% decrease in amplitude, but at the cost of a 12% drag increase. Alternatively, the four control cylinder configurations were best at minimizing drag, but were susceptible to high vibration amplitudes. This continues the trend of drag reduction and amplitude reductions being at opposite ends of the trade space for design consideration.

Although research in the field of passive suppression for VIVs has made significant headway, they are commonly limited or not best suited for specific applications. Omnidirectional methods tend to have limited suppression capability while unidirectional methods are naturally limited in practical application amidst naturally occurring flow fields such as in atmosphere or the ocean. Specific application may require the use of active methods to optimally suppress VIVs.

1.5.2 Active Suppression

Like passive suppression, researches have studies several active methodologies to suppress VIVs. Active suppression methods are classified as those which require energy to suppress VIVs. Examples of active suppression include cylinder rotation, electrical methods, feedback control, suction and blowing, magnetic fields, and thermal effects [11]. Active suppression methods consistently show high potential to suppress VIVs but, in some cases, are limited in practicality (i.e. rotating the columns supporting a bridge). Once again, the amount of research in this field is vast, so only a few examples from the literature will be presented in this thesis.

Electric methods take an electric discharge and creates an electric force to alter the flow field. Like many other methods, this methods relies on delaying the onset of separation from the bluff body. For this to be effective, the fluid in its ambient state must be neutral, making air the predominant candidate for experimentation. The charged ions have an opposing force due to the charge signs. While denser fluids such as water show little potential due to the energy required, research such as those conducted by Artana, Moreau, and Touchard (2003) found it suitable for aerodynamic applications [23].

Feedback control methods use sensors and actuators to adjust to stabilize the near-wake flow field and is currently used in many applications such as aircraft. For circular bluff bodies objects, Williams and Zhao (1989) used acoustic feedback signals from hot-wire anemometers and controlling an actuator at the frequency observed by the hot-wire [24]. Many other works in this area presented in [11], and show potential for implementing other active methods such as thermal effects. Feedback methods utilizing proportional–integral–derivative (PID) controllers are useful for producing optimal solutions for flexible bodies where the flow is subject to change as proven by Zhang, Cheng, and Zou (2004) [25], [26]. Complete suppression is achieved with minimal drag increases; however the design requires a significantly higher amount of complexity and may not be feasible for many application for this reason.

1.6 Suppression Using Thermal Effects

The particular active suppression method which will be utilized in the present research for this thesis is suppression using thermal effects. Convection heat transfer for a fluid past a body is a well-researched documented area; however, the application of heat transfer for VIV suppression is significantly limited in comparison. Convection is the heat transfer mode where heat is both conducted between the body and the surrounding fluid and transferred downstream due to advection simultaneously. Convection comes in two forms: forced and natural. Forced convection relies on the freestream velocity for advection, where natural convection relies on buoyant forces (due to density change within the fluid from differing particle temperatures) to create a flow field. Mixed convection combines these two forms. The premise of this method relies on the buoyant forces acting on the heated fluid near the body reduce the adverse pressure gradient at the aft end of the bluff-body, which is responsible for flow separation. Most studies in the field require that the freestream flow vector be aligned with the gravity/ buoyant force vector for the method to be effective.

Chang and Sa (1990) are among the first to numerically investigate the feasibility of using natural convection to induce suppression [27]. At a *Re* of 100, the surface temperature of the body is heated until suppression is achieved. In terms of non-dimensional parameters, Chang and Sa found a ratio of the Grashof number (*Gr*) to the *Re* ($Gr^{1/2}/Re$) where the vortex shedding was suppressed. The *Gr*, defined in Eq. (10), is used to represent the ratio of the buoyancy to viscous force acting on a fluid and is frequently associated with the study of natural convection.

In this equation g is the acceleration due to gravity, β is the bulk expansion coefficient, T_s and T_∞ are the surface and freestream temperatures respectively, D is the hydraulic diameter, and ν is the kinematic viscosity. The difference between T_s and T_∞ is the major parameter that is experimentally altered in this study.

$$Gr = \frac{g\beta(T_s - T_\infty)D^3}{\nu^2} \tag{10}$$

Michaux-Leblond and Bélorgey (1997) experimentally verified these results stating $Gr^{1/2}/Re > 0.7$ as the critical point where:

> …natural convection is preponderant. Buoyancy effects rule the wake and are responsible or the suppression of the vortex street. The vortex street progressively disappears. There take place two standing eddies. Then, for greater heat input, there clearly appears a secondary flow that fills the loss momentum deficit due to the drag of the cylinder so that the wake shrinks, becoming shorter [[28], p. 97].

They provide a graphical visualization on how additional heat affects the velocity field, particularly at a lower *Re*, and is shown in Figure 11 below. The fluid from $-0.5 < y/d < 0.5$ is the fluid directly aft of the circular cylinder. P/L represents the thermal power (heat energy per unit time) added to the cylinder surface per unit length. As the thermal energy increases, the surrounding fluid temperature gradient in the wake becomes greater, leading to larger buoyant forces, and inevitably a decrease, adverse pressure gradient at the aft end. The adverse pressure gradient is what causes backflow and separation. If the backflow is reduced, the vorticity (**ω**) in the shear layer is decreased. Vorticity, Eq. (11), is a vector representing the change in velocity over a change in position.

$$\boldsymbol{\omega} = \nabla \times \boldsymbol{u} \tag{11}$$

If the vorticity is sufficiently decreased, the vortex shedding mode may return to the bound vortex mode, eliminating the development of oscillatory lift and drag forces. The more the back flow is reduced, the less vorticity will be present and the smaller the vortex wake will be.

Figure 11 demonstrates that as more heat is added at the body surface, the less the local velocity (*U*) will be in comparison to the freestream velocity (U_o). The non-dimensional comparison of the two (U/U_o) is the independent variable and the position away from the center in terms of the diameter (y/d) is the dependent variable. The most notable change lies at the y/d=0 line. The unheated velocity ratio is appoximaly -0.2 where the 375 W/m experiment yields velocity ratios close to 0.8. Although this is still a reduction from the freestream, the difference from the freestream is significantly reduced. Overall, the velocity ratio tends to be increased throughout the y/d range as more heat is added, showing the effect of natural convection and buoyant forces.

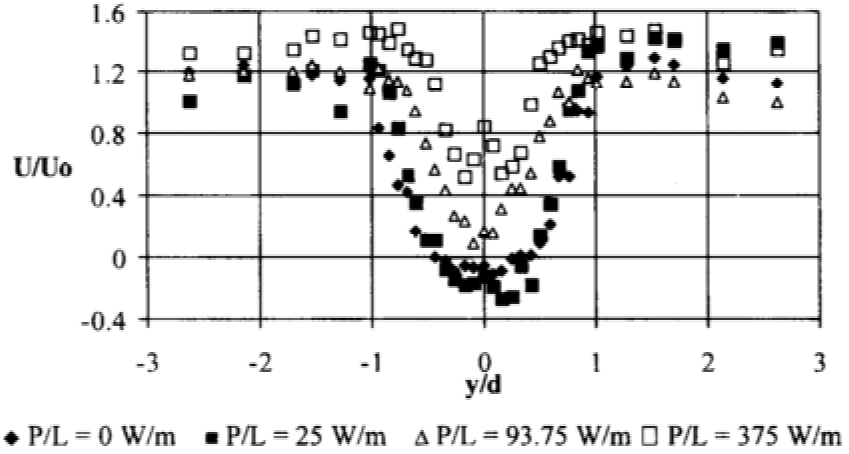

Figure 11. Non-dimensional fluid velocity at x/D = 1.35 and Re = 130. Note: x refers to the axis aligned with the flow and y refers to the access perpendicular to the flow [28].

Although these works provide the plausibility of vortex-shedding, their studies do not include an elastically mounted cylinder that is allowed to translate. This is necessary if VIV suppression is to be studied. Wan and Patnaik (2016) delivered this addition to the VIV body of knowledge and has inspired the present research in this thesis [7]. Their study was conducted at Re = 150 with M_{red} = 0.8, 2, and 20. The chosen Re ensures vortex-shedding for a circular cylinder. The reduced masses are varied to represent different materials in water. In particular M_{red} = 2.0 is approximately the ratio of aluminum in water and was the primary focus in Wan and Patnaik's paper.

Wan and Patnaik first found the lock-in region by sampling bodies with different natural frequencies until steady state. For M_{red} = 2, the lock-in region as shown in Figure 12 shows a region falls between $4 \leq U_{red} \leq 7$ (boxed in green). Here, the amplitude is significantly increased, with a peak at $U_{red} \approx 4$. This is the "worst-case scenario" Wan and Patnaik Figure 13 shows the vortex structure at the peak lock-in frequency whereas Figure 14 demonstrates the same structure but with some additional heat added at the surface. The separation (S) in the figures becomes notably smaller as a reflection of the decreased motion.

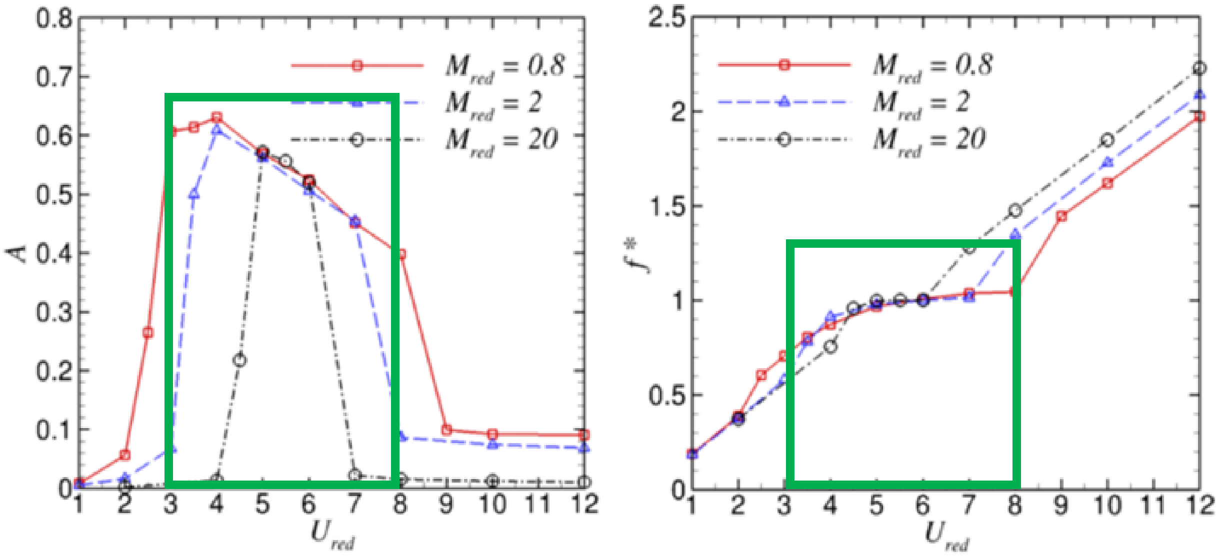

Figure 12. U_{red} sweep for a 2-D circular cross section at Re=150. M_{red} = 0.8, 2, and 20. The left plot shows the amplitude (A) in terms of diameters as the dependent variable. The right plot shows the frequency ratio f^* which is f_{ex}/f_{vac}. The U_{red} values boxed in green represents the lock-in region. Here f^* is approximately 1, meaning $f_{ex} \approx f_{com}$. The amplitudes in this region shown in the left figure are significantly larger than those outside this region [7].

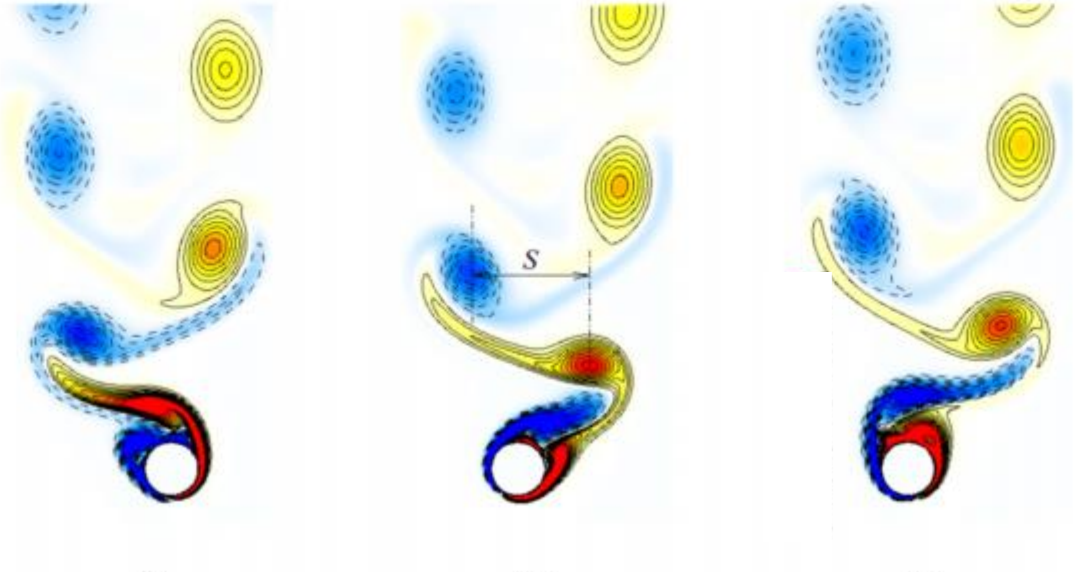

(a) (b) (c)

Figure 13. Vortex structure of a VIV cylinder at various locations, *M_{red}*=2.0, *U_{red}*=4.0, *Ri*=0, *Re*=150. (a) Rightmost. (b) Middle. (c) Leftmost. *S* is a measure of the vortex separation within the vortex street [7]

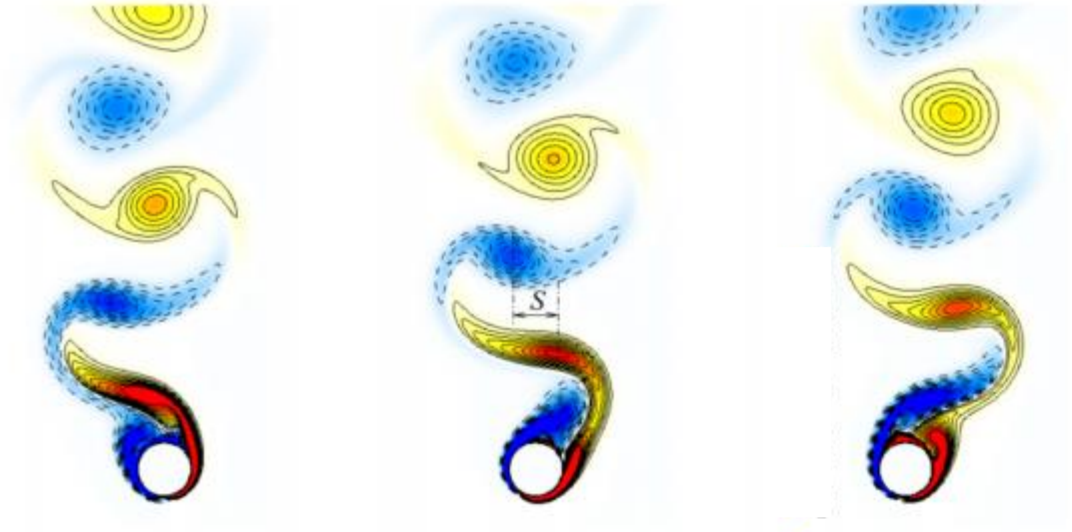

(a) (b) (c)

Figure 14. Vortex structure when the cylinder is located at two extreme positions (a) and (c), and the middle (b). *M_{red}*=2.0, *U_{red}*=4.0, *Ri*=0.3, *Re*=150. (a) Rightmost. (b) Middle. (c) Leftmost. *S* is a measure of the vortex separation within the vortex street [7]

Figure 13 and Figure 14 are contour plots of the rotation within the flow at the peak of the lock-in region (worst-case scenario). Red represents strong counter-clockwise rotation where blue represents strong clockwise rotation. Similarly, the solid lines (other than the body surface) represent streamlines associated with counter-clockwise rotation and dashed lines represent streamlines with clockwise rotation. In these simulations, the body was allowed to translate, and is responsible for the different vortex separations. A body with lots of motion (as seen in Figure 13) has a larger S than a body with less amplitude (shown in Figure 14). Visually, this enables the ability to subjectively determine if the suppression method is reducing the vibrational amplitude of the body.

Once the lock-in region is established, Wan and Patnaik increasing the temperature by increasing a non-dimensional parameter known as the Richardson number (*Ri*). *Ri* is a dimensionless number comparing the ratio of the buoyant forces to shear forces. *Ri* can be expressed as a ratio of *Gr* to *Re* as shown in Eq. (12). This is essentially the same ratio used by Michaux-Leblond and Bélorgey (1997) previously discussed.

$$Ri = \frac{Gr}{Re^2} \tag{12}$$

Simulations were run at a constant *Ri* until steady state is reached. Once steady state is reached, the translational amplitude of the body is determined by measuring the peak displacement of the centroid of the body from its location at rest. Figure 14 demonstrates a simulation where *Ri* is maintained at 0.3. As previously discussed, the comparison of Figure 13 to Figure 14 show how increasing *Ri* decreases the translational motion of the body. Sequential simulations are run following this same process until the translational amplitude is approximately zero. This is demonstrated by the amplitude plots in Figure 15, below.

In Figure 15, the amplitudes (*x*) of four simulations are plotted as the dependent variable against time. The left plot shows the transient response while the right plot demonstrates the same simulations but in a smaller window of time at steady state. The *Ri* = 0.3 curve represents the same simulation demonstrated in Figure 14. As *Ri* is increased, these plots show a decrease in the amplitude. This is best shown in the steady state plot on the right. Additionally, increasing *Ri* also delays the onset of vortex shedding. This is demonstrated by the delayed growth in amplitude over time. For example, the *Ri* = 0.3 reaches steady state at about 80 units of time where *Ri* = 0.5 reaches steady state at approximately 120 time units. At *Ri* = 0.8, the amplitude appears to be completely suppressed for all time and remains constant at close to zero.

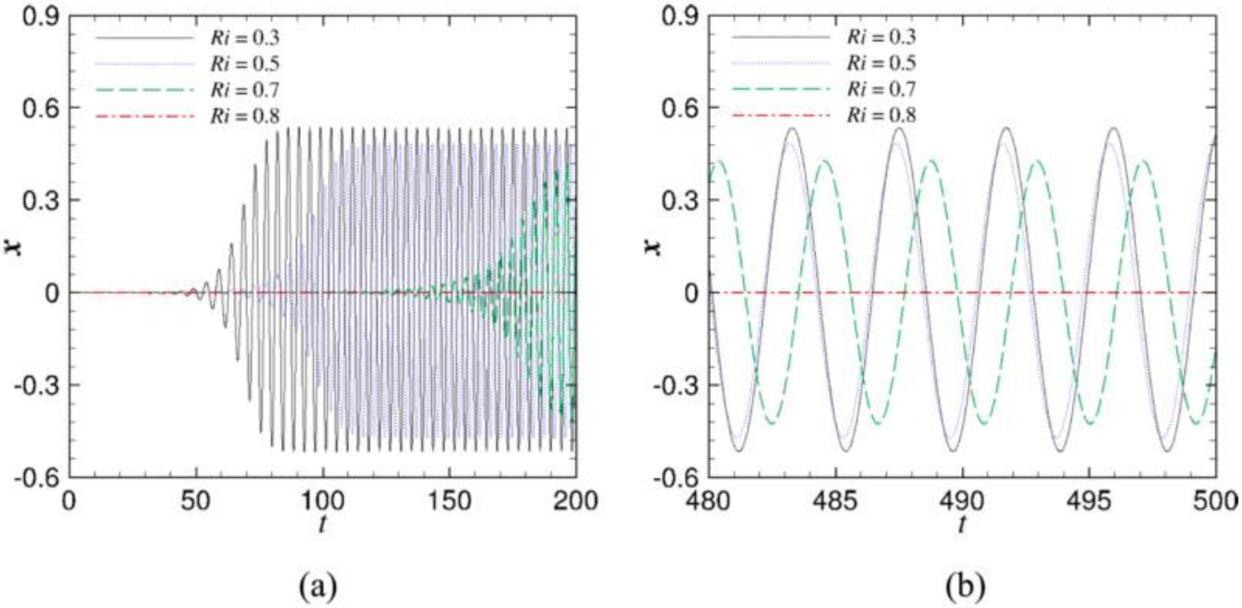

Figure 15. Time history of the displacement of transverse vibration, *Ri*=0.3, 0.5, 0.7, and 0.8. M_{red}=2.0, U_{red}=4.0 *Re*=150: (a) Transient. (b) Steady phase. [7]

Figure 16, below, demonstrates the steady-state vortex formation at *Ri* = 0.8. At this *Ri*, suppression is achieved and bound vortices are formed as opposed to vortex shedding. A wide shear layer (shown by the white space between vortices at the aft end) shows how the velocity differences due to backflow has greatly decreased. Compare this shear layer to those found in Figure 13 and Figure 14. In both of these images the white zero-shear region is very thin, showing much higher differences in velocity. Qualitatively these contour plots can demonstrate if suppression is achieved by analyzing the vortex structure. Quantitatively, the same information may be garnered by amplitude plots such as those displayed in Figure 15. Since circular cross sections are within the family of ellipses (AR = 1), the postulate of the research presented in this thesis explores if suppression can be achieved for ellipses of various ARs by the same thermal effect mechanism.

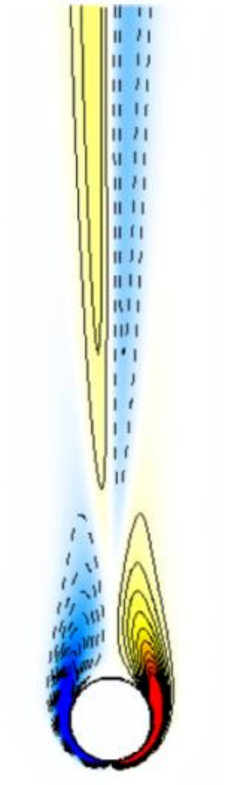

Figure 16. Steady state vorticity at suppression: t=1000, M_{red}=2.0, U_{red}=4.0, Ri=0.8, Re=150. The vortex structure here demonstrates bound vortices as opposed to vortex shedding.

II Theory

The goal of this study is to determine if VIV suppression using buoyant forces is possible for flexible, elliptical cylinders of various aspect ratios. As performed by the proceeding research in this field, this will be achieved by altering the surface temperature of the cylinder in comparison to the freestream fluid temperature. The suppression study will be conducted in both the lock-in and flexible flow regimes for each aspect ratio in question. Much like Wan and Patnaik (2016), the *Ri* will be used as the parameter to define the surface temperature relative to the other flow parameters [7]. In order do so, the governing equations of both the flexible body and flow field must be understood and non-dimensionalized in terms of the key parameters of interest.

2.1 Model of the Elastically Mounted Body

To simplify a 3-D, 6-DOF slender cylinder in a flow field, Wan and Patnaik, like many others, chose to reduce the cylinder to its 2-D cross section with 1-DOF [7]. This simplification greatly reduces the number of experimental variables and allows for key parameters to be isolated to prove a concept. For example, a true 3-D structure will have several vibrational modes, complex motion, and complex deformations to consider. The complexities are equally vast in a 3-D flow-field. While 3-D studies are useful for a specific product design, it is difficult to definitively isolate the influence of each input parameter. Since this thesis is still at the proof-of-concept stage in studying how thermal effects influence VIV's for ellipses, the model will also be reduced to a 2-D cross section with 1-DOF. Assuming the cylinder is sufficiently long in relation to its diameter, Zdravkovich (1981) claims that the ends of the cylinder only would influence the flow a few diameters near those ends [6]. Therefore the influence of the end boundary conditions can be neglected when studying a 2-D cross section far away from the ends.

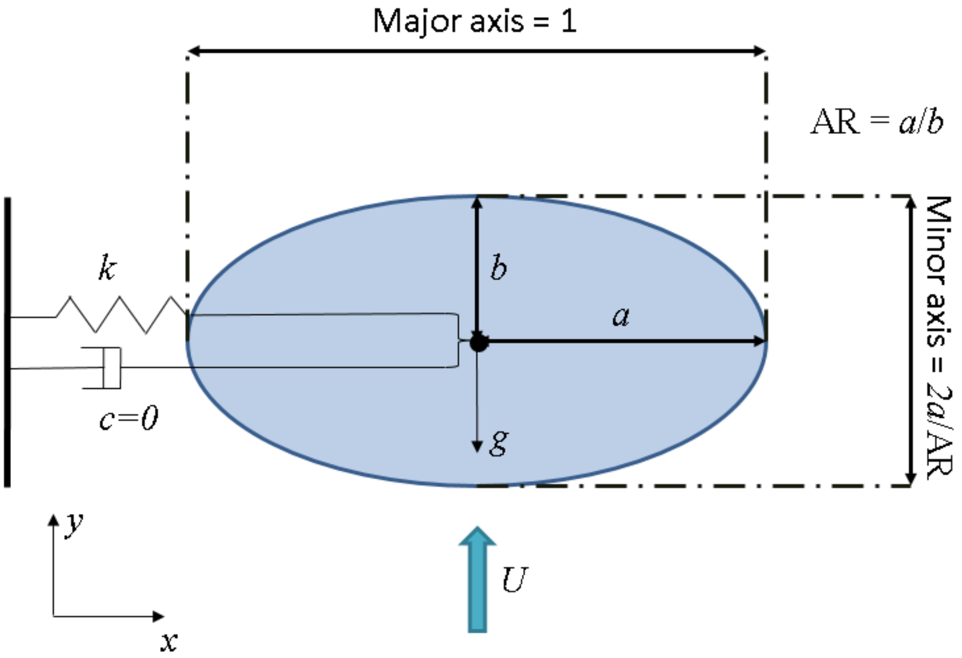

Figure 17. Schematic of a 2-D, elastically-mounted, cylinder with 1-DOF. The body only allowed to translate in the *x* direction. The major axis will always be set equal to 1 for grid sizing purposes. The depicted AR is 2. The gravity (g) is a body force in units length/time^2 and is equal to 9.81 m/s^2 for earth.

Figure 17 demonstrates how the cylinder will be reduced to a simple 2-D, 1-DOF mass-spring-damper system. This will replicate a cross section at some point along a flexible cylinder where the motion can be simply reduced to a body in motion in this system. Doing so assumes the spring coefficient is constant. Since the actual material and geometry (i.e. wall thickness) is not the focus of the study, assuming a constant spring rate will provide a close approximation to a cross section with minimal deformation. This leads to a third assumption: the cross section itself will not deform as the centroid is displaced. This is essentially true for a long, slender body undergoing small deformations due to bending. Both Wan and Patnaik (2016), and Navrose, Yogeswaran, Sen, and Mittal (2014), among many others made these assumptions for their VIV analyses[7], [8].

A fourth assumption is made that the body will predominantly move in the transverse (x) direction. For elliptical bodies of various aspect ratios (AR), Navrose, Yogeswaran, Sen, and Mittal (2014) systematically studied the response of freely vibrating elliptic cylinders with 2-DOF [8]. They studied how the oscillation of C_L and C_D (or C_x and C_y respectively) vary in frequency, magnitude, and phase relative to the body motion as the U_{red} is increased and decreased. Although their study included translation in the direction of the freestream velocity (y-direction), their results showed that the y_{rms}/D is about two orders of magnitude lower than the x_{rms}/D—note: their axis system is inverted from the one presented in this thesis; however, their findings has been renamed into the present reference frame. The RMS value, presented in Eq. (13), describes the variation of a set of values from their mean. The terms x_i represent the points in the data set. In turn, the RMS value helps us understand how much the body is oscillating. Since y_{rms}/D was found to be small for elliptic cross sections, it is safe to conclude that the y component of motion was small relative to the x component, and can be removed as a simplification to the model with marginal error.

$$x_{rms} = \sqrt{\frac{1}{n}\left(x_1^2 + x_2^2 + x_3^2 \ldots + x_n^2\right)} \tag{13}$$

To further validate this point, Figure 18, below, demonstrates how closely the amplitude versus U_{red} plots align between the study using 2-DOF and 1-DOF for motion. For a circular cross section and $M_{red} = 10$, both simulation would find a peak amplitude of about 0.6 between the values $4 < U_{red} < 5$ and the drop out of lock-in between $7 < U_{red} < 8$—assuming the curve for $M_{red} = 10$ falls somewhere between the curves for $M_{red} = 2$ and $M_{red} = 20$. Therefore, a 1-DOF model will be used to isolate the effect of thermal effects on the elastically mounted elliptical cylinder presented in Figure 17.

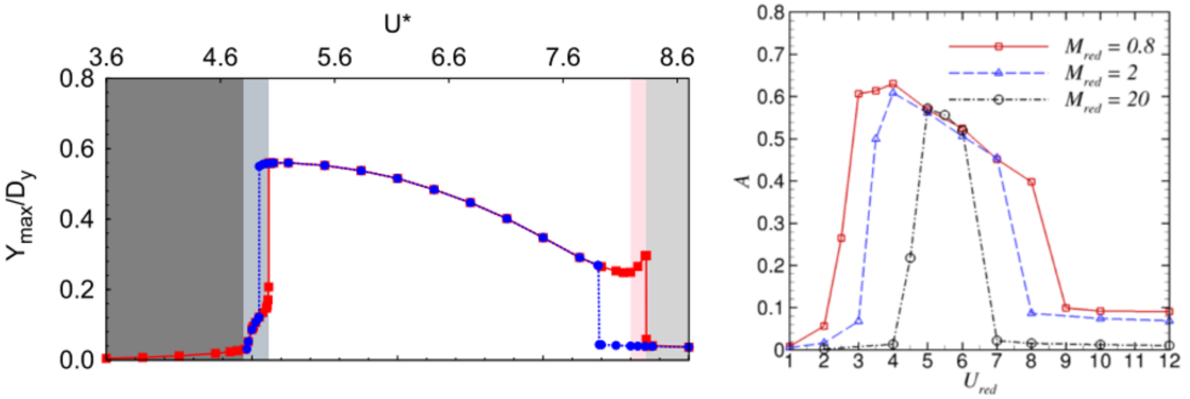

Figure 18. Comparison of steady-state translational amplitude for a circular cross section (AR=1). Navrose et al. [8] (left) uses M_{red}=10 as U* (U_{red}) is increased in red and decreased in blue. Wan and Patnaik [7] (right) vary the reduced mass. If superimposed between the M_{red}=2 and M_{red}=20, the plot produced by Navrose et al. would fall closely in line with the values found by Wan and Patnaik.

The equation of motion for a mass-spring-damper presented in Chapter I in Eq. (9)) can be rewritten in terms of 1-DOF as presented in Eq.(14) It is important not note that the motion is in the Lagrangian system, tracing the centroid of the body from its original position at rest. The equation of motion can then be non-dimensionalized in terms of the key parameters defined in Chapter 1 as shown in Eq. (15). The equation of motion is now in terms of U_{red}, M_{red}, and C_x, where C_x is defined in Eq. (16). In this equation, F_x is the fluid force component in the *x*-direction. To find this, the pressure acting along the body surface must be found, which leads to solving the flow field in the next section.

$$m\frac{d^2Q_x}{dt^2} + c\frac{dQ_x}{dt} + k\,Q_x = F_x \tag{14}$$

$$\frac{d^2Q_x}{dt^2} + \frac{4\pi\zeta}{U_{red}}\frac{dQ_x}{dt} + \frac{4\pi^2}{U_{red}^2}Q_x = \frac{1}{2M_{red}}C_x \tag{15}$$

$$C_L \equiv C_x = \frac{2F_x}{\rho_f U^2 A} \tag{16}$$

Q_x is non-dimensionalized by the diameter, D (ie. Q_x/D) and time in non-dimensionalized by D/U as done in [29]. For this thesis, M_{red} will be held constant at 10 to simulate the approximate density ratio of a steel body in water. U_{red} will be varied by changing f_{ex}. Increasing f_{ex}, and therefore the stiffness, decreases U_{red}. The damping ratio, ζ, is set to 0 to eliminate damping for two reasons. Damping only serves to reduce the vibrational amplitude and alter the response frequency of the structure [30]. Since the study aims to suppress motion at the worst-case-scenarios, reducing ζ to 0 is necessary. Additionally, eliminating damping decreases the computational cost of the simulation.

2.2 Modeling of the Flow Field

Since the model is including buoyant-induced flow from natural convection, it is helpful to utilize the Boussinesq approximation to simplify the non-dimensional Navier-Stokes equations for an incompressible flow. The approximation, states that density changes are negligible except in terms where the density is multiplied by gravitational forces [31]. Eq. (17) is the standard version of the continuity equation, where Eq. (18) shows the continuity equation after the Boussinesq approximation is applied and the terms are non-dimensionalized. Likewise, Eqns. (19, 20) represent the forms of the conservation of momentum equation and Eqns. (21, 22) represent the conservation of energy equation. In the energy equation, k_t represents the thermal conductivity. The resulting non-dimensional parameters are *Re, Pr,* and *Ri*. *Pr* and *Ri* are expanded in Eqns. (23 and 24). In these equations, ν is the kinematic viscosity, α is the thermal diffusivity, g is gravity and β is the thermal expansion coefficient.

$$\frac{\partial \rho}{\partial t} + \nabla \cdot (\boldsymbol{\rho u}) = 0 \tag{17}$$

$$\nabla \cdot \boldsymbol{u}^* = 0 \tag{18}$$

$$\frac{\partial \boldsymbol{u}}{\partial t} + \boldsymbol{u} \cdot \nabla \boldsymbol{u} = -\frac{1}{\rho} \nabla p + \nu \nabla^2 \boldsymbol{u} - g\alpha\Delta T \tag{19}$$

$$\frac{\partial \boldsymbol{u}^*}{\partial t} + \boldsymbol{u}^* \cdot \nabla \boldsymbol{u}^* = -\nabla p^* + \frac{1}{Re} \nabla^2 \boldsymbol{u}^* + Ri\,\theta \tag{20}$$

$$\frac{\partial T}{\partial t} + \boldsymbol{u} \cdot \nabla T = k_t \nabla^2 T \tag{21}$$

$$\frac{\partial \theta}{\partial t} + \boldsymbol{u}^* \cdot \nabla \theta = \frac{1}{RePr} \nabla^2 \theta \tag{22}$$

$$Pr = \frac{\nu}{\alpha} \tag{23}$$

$$Ri = \frac{g\beta\Delta\theta D}{U^2} \tag{24}$$

The Navier-Stokes equations are in the Eulerian reference frame and are functions of $\boldsymbol{u}^*$, p^*, and θ. These variables are the non-dimensional velocity, pressure, and temperature of the flow field and are non-dimensionalized in Equations 25-27. In these equations, U is the freestream velocity, ρ_f is the density of the fluid, T_∞ is the free-stream temperature, and T_s is the surface temperature of the bluff-body. The fluid pressure along the boundary of the bluff body can be found using the Navier-Stokes equations to find the net force acting on the body.

$$\boldsymbol{u}^* = \frac{\boldsymbol{u}}{U} \tag{25}$$

$$p^* = \frac{p}{\rho_f U^2} \tag{26}$$

$$\theta = \frac{T - T_\infty}{T_s - T_\infty} \tag{27}$$

2.3 Solution

Although an elliptic body is relatively simple, there is no direct analytical solution of the coupled Navier-Stokes equations combined with the equation of motion. One issue is that non-linear terms exist in the Navier-Stokes equations. This would require either an approximate solution or a numerical solution. Since this is a new field of research, no approximation solutions exist. Therefore, the solutions must be found numerically by discretizing the equations in time and space.

Another issue is the different reference frames. The Navier-Stokes equations are in Eulerian, meaning the equations evaluate the flow at a given position throughout time. The equation of motion, however, is Lagrangian, meaning the reference frame is always from the centroid of the fluff-body. Although there exist ways to convert reference frames, this will be unnecessary since the solution will be found numerically and the equation of motion can be solved separately at each time step after the forces acting on the body are found from Navier-Stokes solution. This is possible because the motion between time steps is small. The specifics on the numerical solutions will be discussed in Chapter III.

2.4 Critical Richardson Number

Now that the motion of the cylinder has been defined and the Navier-Stokes equations are in their desired form, the *Ri* may be directly used as an input to directly manipulate the temperature of the cylinder's surface relative to the temperature of the freestream fluid. It is the goal of the study to define a critical Richardson number (Ri_c) to non-dimensionally determine the minimum *Ri* when complete suppression occurs. Wan and Patnaik used numerical simulations to model VIV suppression for a circular cylinder with a thermal input dictated by the *Ri* [7]. As discussed in Chapter I, they found that for a 2-D circular cylinder and a Re of 150, vibrational motion in the lock-in and flexible regimes was reduced as the *Ri* was increased.

Complete suppression was considered to occur once the motion of the cylinder was very small relative to D. Since "very small" may be too arbitrary to alone determine Ri_c, Wan and Patnaik also considered how C_D (C_Y when the flow is aligned vertically with gravity) altered with a change in *Ri*. From the Reynolds Analogy, it is known that an increase in the heat transfer through convection at a surface boundary will increase the friction coefficient at that boundary [32]. Therefore, the body cannot be heated without the potential cost of adding drag. Figure 19, below, shows a plot of the amplitude of motion (A) and $\overline{C_D}$ as a function of Ri.

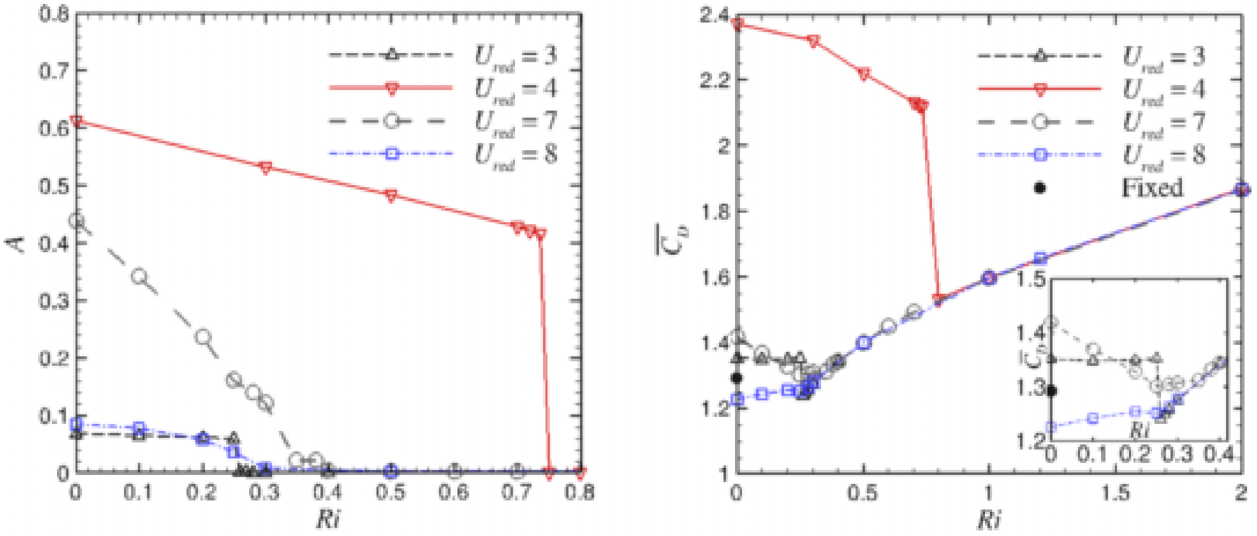

(a)

(b)

Figure 19. Steady-state amplitude (a) and time-averaged drag coefficient (b) at various Richardson numbers for U_{red} = 3, 4, 7, and 8. Re = 150, M_{red} = 2. The black dot in plot (b) shows the drag for an unheated, fixed body [7].

Using Figure 19, Ri_c may be determined graphically. In plot (a), the maximum, steady-state amplitude of the body's motion is plotted as the dependent variable against Ri. In this plot, U_{red} = 3, 4, 7, and 8 are considered to show the stiff (U_{red} = 3), lock-in (U_{red} = 4), and flexible (U_{red} = 7, 8) regions. VIV suppression can be determined using plot (a) when A ≈ 0. For the stiff, flexible and lock-in bodies, this occurred at $Ri \approx 0.25$, 0.3, and 0.8 respectively.

This is further supported by looking at the the $\overline{C_D}$ curve in plot (b). For the stiff and flexible bodies, there is a point where the $\overline{C_D}$ either reaches a local minimum or $d\overline{C_D}/dRi$ reaches a minimum near where suppression is first achieved. For example, the zoomed in section of plot (b) shows how the $\overline{C_D}$ curve for U_{red} = 8 levels off near $Ri \approx 0.25$, then begins to increase after that point. The $\overline{C_D}$ curves for U_{red} = 3 and 7 also have a minimum value at $Ri \approx 0.25$ and begin to increase thereafter.

Likewise, the lock-in region line (red) has a significant decrease in drag as the VIVs are suppressed, reaches a minimum at $Ri \approx 0.8$, and then gradually increases at the same rate as the other bodies. The critical Richardson number (Ri_c) is determined to be a point where both suppression is achieved and $\overline{C_D}$ is at or near the corresponding local minimum. While the lock-in region has a clearly defined Ri_c at $Ri \approx 0.8$, bodies in the transition of regions, such as the $U_{red} = 7$ curves, don't have a $\overline{C_D}$ minimum that lines up perfectly with a point of suppression; however, an estimate Ri_c may still be determined at $Ri \approx 0.35$.

Several conclusions can be drawn from the coupled results from plots (a) and (b). First, the drag is high when there is no or little heat input and the amplitude is high. This is due to the relative flow velocity around the body being greater due to the body's motion and a large low pressure region forming a the aft end of the body. It is also known that heating the body will increase the skin friction component to drag. Therefore, a tradeoff exists between the reduction of motion and the addition of heat.

For some bodies, such as those in lock-in, the drag increase due to motion is significantly higher than the drag increases due to heat transfer. Thus, a large decrease in drag is achieved despite increased heat transfer at the surface. This is also seen for the $U_{red} = 3$ and 7 bodies, but to a lesser extent. The flexible body, having a much lower unsuppressed VIV amplitude, did not see a decrease in drag; however, the drag saw little increase while reaching suppression, and the rate of drag increase noticeably climbs after Ri_c. Once VIV suppression is achieved, all of the bodies fell along the same $\overline{C_D}$ curve which increased as Ri increased. This leads to the conclusion that if thermal effects are used for VIV suppression, the system should operate at Ri_c to avoid unwanted increases in drag. This is particularly applicable to optimizing designs of a heat exchanger or taking advantage to a hotwire anemometer heat to reduce vibrational noise in the signal.

III Methodology

As stated in Chapter II, non-linearites, and the coupling of the Navier-Stokes to the 1-DOF equation in different reference frames, requires the use of numerical methods to solve. Mittal and Balachandar (1996) proved that accurate representation of elliptical cylinders can be achieved by using numerical methods compared to well established experimental values [33]. Song and Wu (2012) validated the use of fractional step methods on collocated grids using immersed boundary methods [34]. These immersed boundary methods as proven by Mittal and Iaccarino (2005); Ghias, Mittal, and Dong (2007); and Mittal, Dong, and Bozkurttas (2008) allow the body in motion to be represented on a fixed, Cartesian grid. The following chapter will first detail how the governing equations are discretized, discuss the domain space and boundary conditions, set-up and converge the grid, and provide the test cases and respective parameters used for the study.

3.1 Discretizing the Navier-Stokes Equations

A discrete function is one in which a differential equation can be turned into an approximate algebraic expression where known values can be used to solve for the unknown. Taylor series expansion of the differential terms are used to find these expressions. The forward difference shown in Eq. (28) is used for approximating the first derivative terms in time and space. The second derivative convection and diffusion terms are approximated by a second order central difference shown in Eq. (29). In these equations, *h* represents the discrete difference used in the domain. These equations also give the order of error associated with the approximation. A higher order of error is favorable since the difference is usually much less than 1.

$$f'(x) \approx \frac{f(x+h)-f(x)}{h} + \mathcal{O}(h) \tag{28}$$

$$f''(x) \approx \frac{f(x+h)-2f(x)+f(x-h)}{h^2} + \mathcal{O}(h^2) \tag{29}$$

Recall the non-dimensional Navier-Stokes equations presented in Chapter II from Eqns. (18, 20, and 22):

$$\nabla \cdot \boldsymbol{u}^* = 0$$

$$\frac{\partial \boldsymbol{u}^*}{\partial t} + \boldsymbol{u}^* \cdot \nabla \boldsymbol{u}^* = -\nabla p^* + \frac{1}{Re}\nabla^2 \boldsymbol{u}^* + Ri\,\theta$$

$$\frac{\partial \theta}{\partial t} + \boldsymbol{u}^* \cdot \nabla \theta = \frac{1}{RePr}\nabla^2 \theta$$

The conservation equations may be expanded to:

$$\frac{\partial u}{\partial x} + \frac{\partial v}{\partial y} = 0 \tag{30}$$

$$\frac{\partial u}{\partial t} + u\frac{\partial u}{\partial x} + v\frac{\partial u}{\partial y} = -\frac{\partial p^*}{\partial x} + \frac{1}{Re}\left(\frac{\partial^2 u}{\partial x^2} + \frac{\partial^2 u}{\partial y^2}\right) + Ri\theta \tag{31}$$

$$\frac{\partial v}{\partial t} + u\frac{\partial v}{\partial x} + v\frac{\partial v}{\partial y} = -\frac{\partial p^*}{\partial y} + \frac{1}{Re}\left(\frac{\partial^2 v}{\partial x^2} + \frac{\partial^2 v}{\partial y^2}\right) + Ri\theta \tag{32}$$

$$\frac{\partial \theta}{\partial t} + u\frac{\partial \theta}{\partial x} + v\frac{\partial \theta}{\partial y} = \frac{1}{RePr}\left(\frac{\partial^2 \theta}{\partial x^2} + \frac{\partial^2 \theta}{\partial y^2}\right) \tag{33}$$

Eqns. 30-33 are the continuity, *x*-momentum, *y*-momentum, and energy equation in that order. The equations are in terms of the two primitive variables $\boldsymbol{u}^*$, θ and p^* where $\boldsymbol{u}^*$ has been expanded to its non-dimensional components *u* (*x*-direction) and *v* (*y*-direction). Using the finite difference presented in Eqns. (28 29), they are discretized in time and space using a cell-centered, collocated arrangement on a Cartesian grid. This is to say that the values of $\boldsymbol{u}^*$ θ and p^* for a small, discrete volume is represented at a single point as shown by the dashed region of Figure 20. Eq. (34) demonstrates an example of the discretized energy equation.

$$\frac{\theta_{k+1}^{i,j}-\theta_k^{i,j}}{\Delta t}+u_k^{i,j}\frac{\theta_k^{i+1,j}-\theta_k^{i,j}}{\Delta x}+v_k^{i,j}\frac{\theta_k^{i,j+1}-\theta_k^{i,j}}{\Delta y} = \frac{1}{RePr}\left(\frac{\theta_k^{i+1,j}-2\theta_k^{i,j}+\theta_k^{i-1,j}}{\Delta x^2}+\frac{\theta_k^{i,j+1}-2\theta_k^{i,j}+\theta_k^{i,j-1}}{\Delta y^2}\right) \tag{34}$$

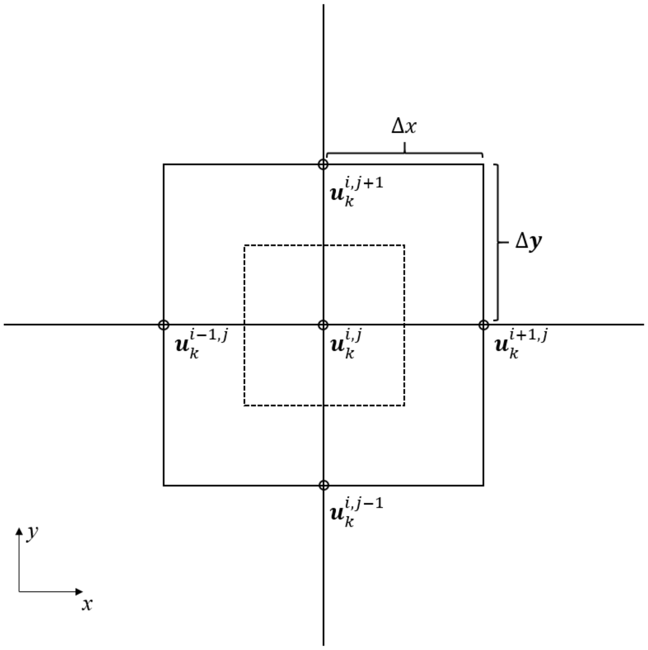

Figure 20 Collocated arrangement of *u* on a Cartesian grid. The indices *i, j,* and *k* represent the discrete steps in the *x*-direction, *y*-direction, and time respectively. The dashed region shows the area (or cell) represented by point (*i,j*).

3.2 Solution Method

Now that the governing equations are discretized, numerical solutions may be implemented. The custom solver used by Wan and Patnaik (2016) was employed. The Navier–Stokes equations are implicitly coupled with the body equation of motion and are solved iteratively. Starting from rest, the body position is updated based on its velocity of the previous step. Then the Poisson relations within the Navier-Stokes equations are iteratively solved using Line Successive Over Relaxation (LSOR). The Poisson equation is elliptic so the entire domain space must be solved simultaneously due to the dependence on needed information from the surrounding nodes in the second-order central differences. This is done iteratively until a residual criteria is met. For this simulation, the pressure at each node is compared between iteration. If the maximum difference between the two iterations is less that 5e-4 then the simulation is allowed to move on.

In time, the equations are integrated using a fractional-step method as performed in [7], [34], [35]. This means the time step is split into at least two sub-stages to solve for the next full time step. The method used solves for the primitive variables directly using the projection method as outlined by Kim and Moin (1985) and Guermond, Minev, and Shen (2006), since the method allows for the velocity and pressure terms to be decoupled [36], [37]. This method progresses in time to a predictor mid-time-step in advection terms for mass and momentum transport are solved. This is done by assuming the velocity field has no divergence. Then, the corrector step implements a time-centered estimate to the fluid properties and the divergence restraint is reinforced to form the final time-step state.

Once the flow is solved, the pressure and shear stresses along the surface of the body are numerically integrated along the surface to get the total force acting on the body by the flow. To do so an immersed boundary method as described in [38]–[40] is employed, allowing a body of complex geometry and in motion to be represented on a Cartesian grid. This is the forcing function in the body equation of motion from Eqns. (14 15). Knowing the resultant force acting on the body, the equation of motion is solved for the position of the body at the next time step. The solution method described in this section is them repeated. This entire process replicates the process presented in Wan and Patnaik (2016) [7].

3.3 Boundary Conditions and Domain Space

Now that the governing equations and the solution method is in order, the physical domain of the simulation must be determined. Since the goal is to model a single, elastic body subject tin a uniform freestream, the domain must be large enough to account for any motion by the body as well as have sufficient flow fore and aft of the body to ensure the boundary conditions have negligible impact on the accuracy of the simulation. The flow will be open to ambient conditions and not confined to a channel, so there will be no boundary layer development along the edges of the domain space. The following section describes the boundary conditions and domain sizing use to give an accurate representation of the desired physical setup.

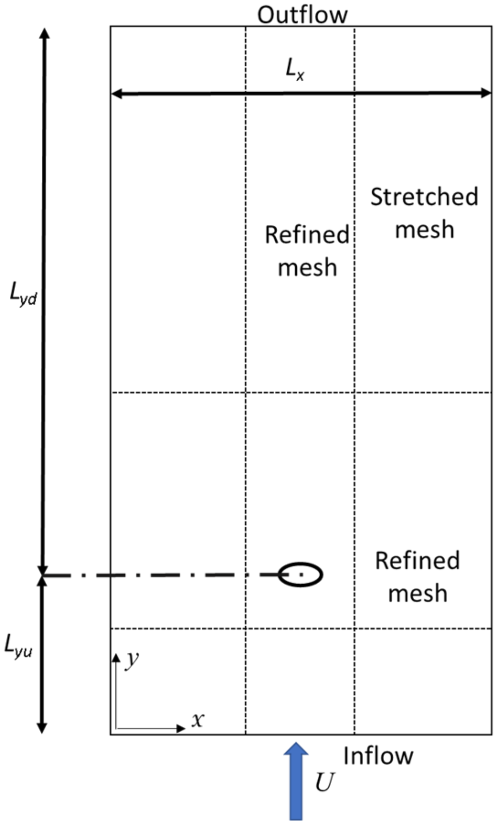

Figure 21. Notional sketch of the computational domain. L_x is the lateral length of the computational domain. L_{yu} and L_{yd} are the length up and downstream of the body centroid in units D. The dashed region contains the refined mesh where the region outside is more coarse. These sizing values are referenced in Table 1 below.

Figure 21 demonstrated the computational domain where fluid flows around a 1 DOF, elastically mounted cylinder. The boundary conditions, shown in Figure 22, are set up in accordance with Wan and Patnaik (2016) [7]. A non-slip and impermeable boundary condition is maintained at the cylinder wall as well as a Neumann boundary condition for pressure $\frac{\partial p}{\partial n} = 0$ where n is the normal vector to the surface. This is the best representation for a solid surface and a viscous fluid. When conducting simulations with convection taking place, the cylinder wall is set to maintain a constant, uniform temperature, T_s by setting θ equal to 1 at all points along the surface boundary.

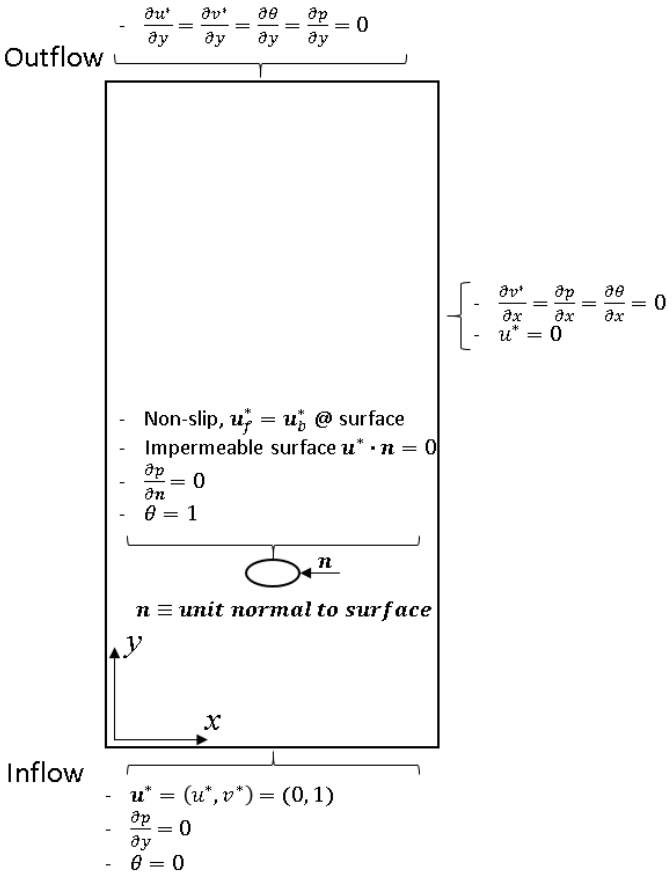

Figure 22. Boundary conditions applied to domain space. The conditions listed on top apply to the outlet boundary. The conditions to the right apply to both lateral bounds. The conditions in the center apply to the cylinder surface. The conditions at the bottom apply to the inlet boundary

The inflow boundary has a Dirichlet boundary condition where $\boldsymbol{u}^*$ = (0, 1) and the temperature is T_∞, $(\theta = 0)$. This represents a uniform free stream flowing vertically only at the entry. The freestream is cool relative to the body and the difference is determined by *Ri*. Additionally, a Neumann boundary condition is imposed for pressure $\left(\frac{\partial p}{\partial y} = 0\right)$. These conditions requires the body to be sufficiently upstream to be true since pressure and velocity changes will develop along the leading surface of the body.

The outflow boundary uses a Neumann boundary condition where $\frac{\partial u^*}{\partial y} = \frac{\partial v^*}{\partial y} = \frac{\partial \theta}{\partial y} = \frac{\partial p}{\partial y} = 0$. This is a good approximation if the outlet is sufficiently downstream of the body since these changes will be small. The lateral boundaries use a mix of Dirichlet and Neumann: $\frac{\partial v^*}{\partial x} = \frac{\partial \theta}{\partial x} = \frac{\partial p}{\partial x} = 0$ and $u^* = 0$. The latter mentioned maintains that no fluid crosses the lateral boundary. In these boundary conditions, u^* and v^* are the directional components of $\boldsymbol{u}^*$ in the *x* and *y* directions respectively.

To determine the proper size of the domain space, a convergence study is conducted on the computational domain for an elastically-mounted, circular cylinder at *Re*=150. The peak lift coefficient (C_L) showed consistent results throughout the variation and yielded accurate results with little variation when the domain space was increased. D2 ($L_x = 30D$, $L_{yu} = 8D$, and $L_{yd} = 32D$) will therefore be used for all simulations presented in Chapter IV will use this domain sizing. Table 1 shows the simplified results from this domain space study.

Table 1. Domain Space Variation [7]

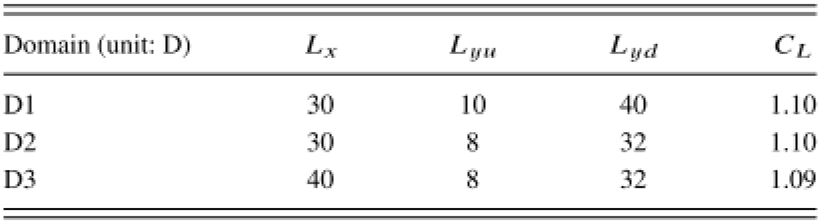

Domain (unit: D)	L_x	L_{yu}	L_{yd}	C_L
D1	30	10	40	1.10
D2	30	8	32	1.10
D3	40	8	32	1.09

3.4 Grid Convergence

Now that the size of the domain is determined, a grid must be determined to carry out the finite difference calculations. This study ensures that the solution to the fluid-structure interaction reaches a point where an increase in grid resolution has a minimal decrease in error. While the error is directly related to the grid sizing, so is computation cost. Therefore a study is needed to determine where further refinement has a minimal impact on the solution. The sizing is incrementally reduced and the key parameters are compared.

To aid in reducing computation cost, a region of the domain space, where the body and near wake are located, is more refined than the rest of the domain. This is called the "refined region" and is shown in Figure 21 from the prior section. Outside of the refined region, the changes in the flow properties are much smaller, so the error associated with them is inherently small. Therefore, the error will be less sensitive to the grid size, and a larger grid spacing can be used with minimal impact to the solutions at the body surfaces. Figure 23, below, shows how the grid begins to expand as is further removed from the refined region in both the *x* and *y*-direction.

Table 2 demonstrated the results when the resolution in the refined region is altered. *St*, C_L, and $\overline{C_D}$ (lift coefficient amplitude and mean drag coefficient) are all used as the key parameters to measure the results of the simulation. The vortex shedding frequency is consistent in all three as seen by the constant *St*. The parameter h represents the spatial difference used in the grid. This value is equal to both Δx and Δy as shown back in Figure 20 as square volumes are used within the refined region. The lift and drag coefficients see minor variation between h = 0.015 and 0.01—therefore h = 0.015 is selected to reduce computational loading for the simulations in Chapter IV.

Table 2. Cartesian Grid Sizing (refined mesh region) [7]

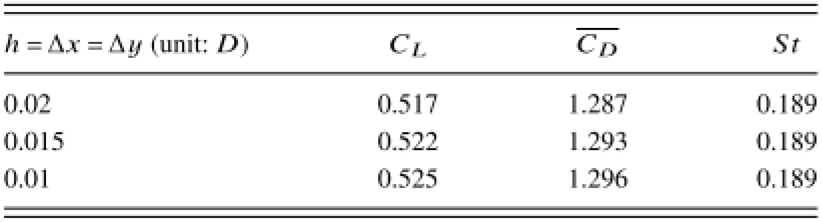

$h = \Delta x = \Delta y$ (unit: D)	C_L	$\overline{C_D}$	St
0.02	0.517	1.287	0.189
0.015	0.522	1.293	0.189
0.01	0.525	1.296	0.189

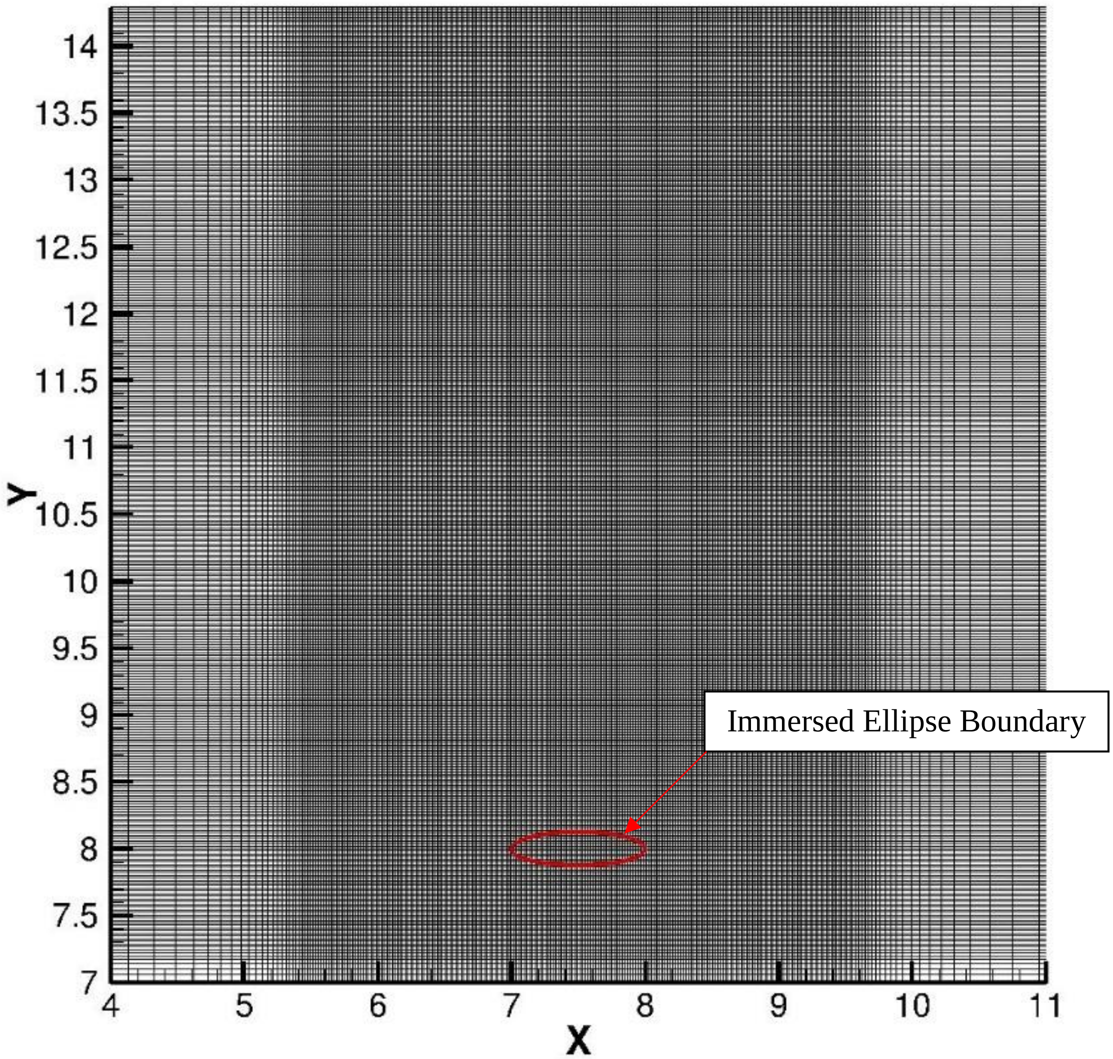

Figure 23. Cartesian grid for the refined region. Ellipse with AR=4 shown in red.

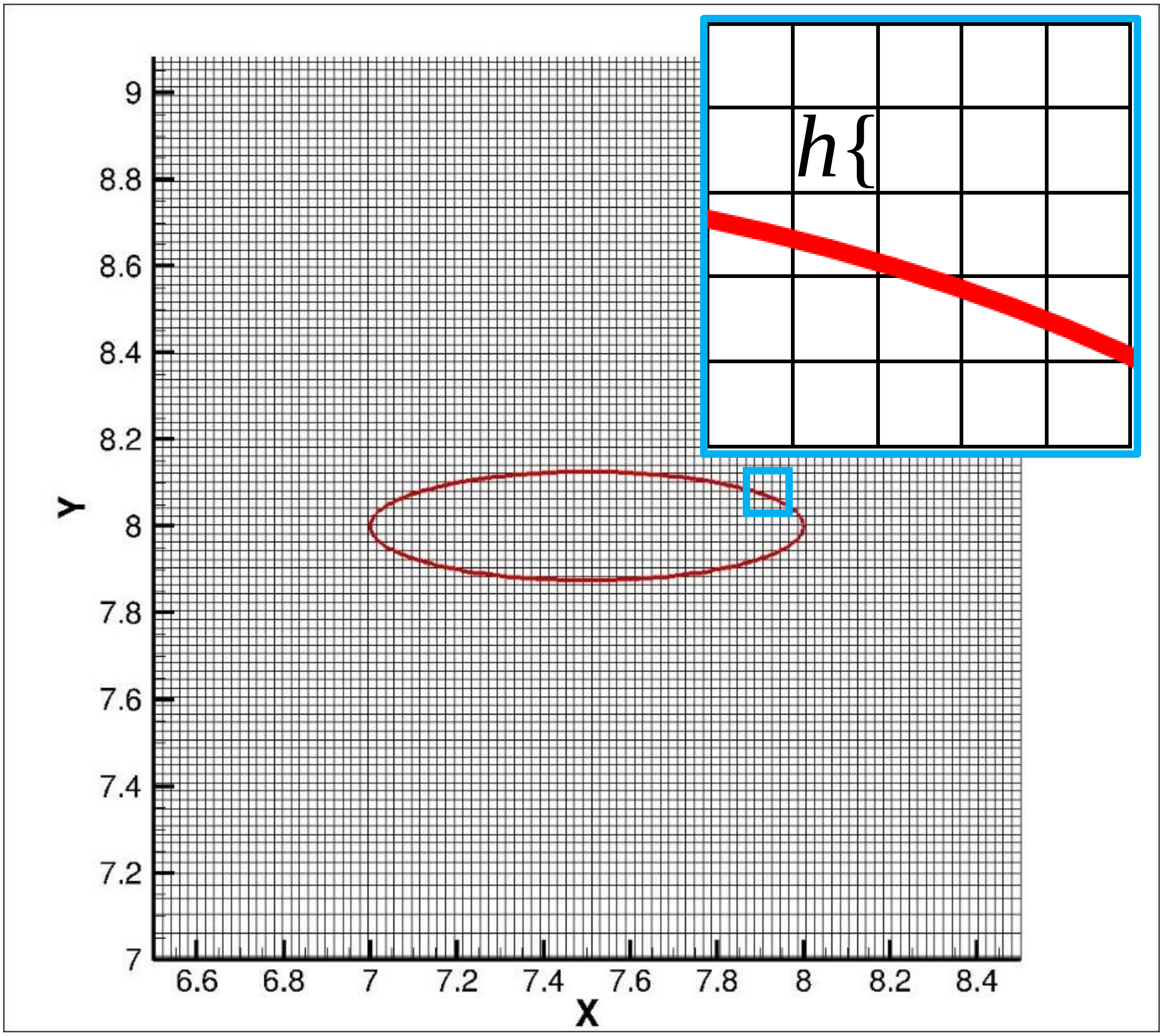

Figure 24. Zoomed Cartesian grid surrounding the body surface. Ellipse with AR=4 shown in red. Each square in the grid is length $h \times h$ as shown in the blown up box outlined in blue.

Lastly, the time step length was derived from a time step study using Δ*t* = 0.02, 0.01, 0.005 on the grid and domain space formulated from the last two studies. For this study, the vibrational amplitude Q_x/D was monitored at steady state. The difference between Δt = 0.01 and 0.005 was 1.6%, which justified using Δt = 0.01 for all of the remaining simulations in Chapter 0 in order to reduce the computation cost by half.

3.5 Model Validation

Validation of the model was conducted of the current model compared to the findings of other published studies. The validations presented were completed by Wan and Patnaik (2016) [7]. Three validation tests were used in order to ensure the model matched published findings for stationary vortex shedding, VIVs, and convection. This ensures all components of the model are accurate to test thermal effects combined with VIVs.

The first study compares the solver used on a stationary circular cylinder. Similar to the grid convergence study, *St*, C_L and $\overline{C_D}$ are all used as key parameters to compare the models. As Table 3 demonstrates, the results from the solver used match the results seen in other publications, including *Re* =100, which will be the *Re* used in this thesis.

Table 3. Validation of force coefficients and Strouhal number for a fixed cylinder [7]

Fixed cylinder	*Re*	C_L	$\overline{C_D}$	*St*
Shiels [41]	100	0.30	1.33	0.167
Qu [42]	100	0.32	1.32	0.165
Present	100	0.337	1.301	0.169
Qu [42]	150	0.501	1.305	0.184
Present	150	0.502	1.293	0.189
Liu [43]	200	0/69	1.31	0.192
Etenne [44]	200	0.67	1.360	0.195
Meneghini [45]	200	0.66	1.30	0.196
Present	200	0.685	1.311	0.201
Blackburn[46]	500	1.20	1.46	0.228
Present	500	1.166	1.410	0.227

Now that that the model is validated for a stationary cylinder with no heat transfer, the second validation study adds mixed convection to the model. Two different parameters, $\overline{C_D}$ and *Nu*, are compared, as they both are directly related to the heat transfer at the surface. Table 4 shows the comparison for the time-averaged drag coefficient. The case was validated for a circular cross section with Re = 100, Pr = 0.71, and Ri = 0 – 1, which will be similar for the test parameters used in this thesis. Table 5 shows the time-averaged Nusselt number, $\overline{Nu}$ also using parameters Re = 100, Pr = 0.71, which are the same used in this thesis. These two tests demonstrate that the model will accurately represent mixed convection.

Table 4. Time-averaged drag coefficient in mixed convection of flow past cylinders [7]

			Time Averaged $\overline{C_D}$	
Re	*Pr*	*Ri*	Literature	Present
			Patnaik [47]	Circular
40	0.71	0	1.63	1.446
		1	2.57	2.617
			Srinivas *et al.* [48]	Circular
	10	0	1.499	1.446
		1	2.398	2.466
		2	2.899	3.078
			Patnaik [47]	Circular
100	0.71	0	1.42	1.204
		0.5	1.61	1.594
		1	1.68	1.875
			Sharma and Eswaran [49]	Square
		0	~1.6	1.475
		0.5	~2.0	1.981
		1	~2.6	2.516
			Sengupta *et al.* [50]	Circular
130	0.71	0.2	1.42	1.305
			Patnaik [47]	Circular
200	.071	0	1.32	1.312
		0.5	1.38	1.325
		1	1.46	1.537

Table 5. Time-averaged Nusselt number $\overline{Nu}$ of flow past a heated stationary cylinder, *Re*=100, *Pr*=0.71 [7]

Ri	Chang and Sa [27]	Sengupta *et al.* [50]	Hasan and Ali [51]	Present
0	5.23	5.106	5.154	5.196
0.1	5.20	5.144	…	5.223

Table 6. Comparison on vibration amplitude and force coefficient of a cylinder in vortex-induced vibration [7]

	Re	M_{red}	U_{red}	A	C_L
Ahn [52]	150	2.0	4.0	0.58	1
Borazjani [53]	150	2.0	4.0	0.54	…
Present	150	2.0	4.0	0.61	1.10
Ahn [52]	150	2.0	5.0	0.54	0.26
Present	150	2.0	5.0	0.58	0.27
Borazjani [53]	200	2.0	4.0	0.5	0.72
Present	200	2.0	4.0	0.59	0.72

The final validation study compares how the VIV response compares to other published literature. All cases were limited to 1-DOF motion perpendicular to the direction of freestream flow. The U_{red} was chosen such that the body would be in lock-in. The study compares the motion directly by considering the motion amplitude (A) and the amplitude of the C_L signal. The study also found that the forced response frequency (f_{ex}) for Re = 150, U_{red} = 4.0 matched Ahn and Kallinderis (2006) with their frequency being 0.232 Hz and Wan and Patnaik's being 0.231 Hz [52]. Likewise f_{ex} was consistent with Borazjani and Sotiropoulos (2009) at Re = 200, U_{red} = 4.0 with their result being 0.23 and Wan and Patnaik's being 0.233 [53]. All studies demonstrated periodic vortex shedding which would be expected given the flow conditions and other findings throughout VIV literature. Although a higher M_{red} (M_{red} =10) will be used in the test cases for this thesis, the solver has proven to be robustly accurate in a number of test cases. All three studies prove the solver will be an accurate tool for solving the test cases presented.

3.6 Test Parameters

The goal of this thesis is to see how the findings of Wan and Patnaik (2016) can be extended to elliptical cross sections of various ARs. Therefore, tests were conducted in regards to the seven ARs shown in Figure 25. Before considering the addition of heat transfer, the VIV regimes discussed in Chapter I section 1.4 must be found; particularly the lock-in and flexible regions. Simulations were run at Re = 100 and M_{red} = 10 while U_{red} is varied between 1 and 9 to match the conditions used in Navrose *et al.* (2014). This ensures VIV validation for elliptic cross sections may be performed [8]. M_{red} = 10 is similar to the density ratio of steel in water, which is common for many application.

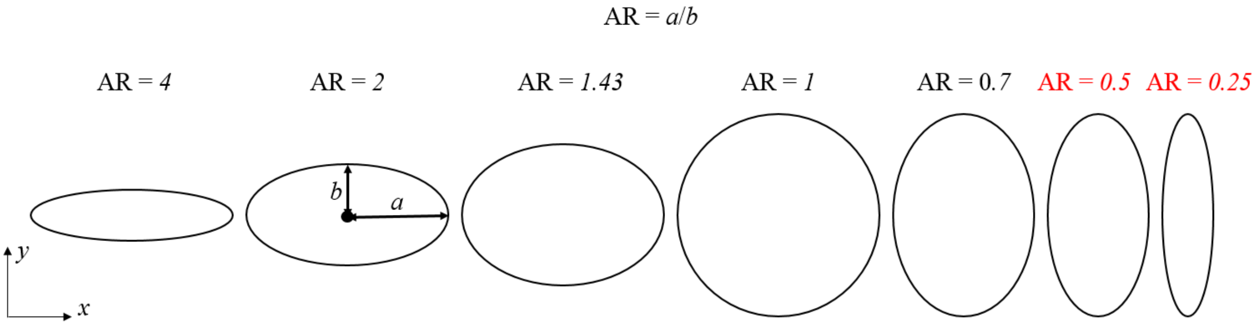

Figure 25. Aspect ratios considered in the study: 4, 2, 1.43, 1, 0.7, 0.5, and 0.25. ARs 0.5 and 0.25 did not demonstrate vortex shedding and were eliminated from the study.

The aspect ratios were selected such that three of the cases (AR = 1.43, 1, 0.7) could be used to validate against other literature, while the remaining extend beyond most available published literature to expand the knowledge base. Increasing the AR beyond 4 and decreasing below 0.25 causes the body to act more like a thin plate than a conical body and therefore were not considered. Table 7 shows the U_{red} sweep test cases used to find the VIV regimes for each AR. Down the left column is each AR studied. Along each row lists the U_{red} value used in each simulation. For example, AR 0.25 was tested at U_{red} = 1, 2, 3, 4, 5, 6, 7, 8, and 9. Initially, only integer values between 1 – 9 were tested. Then intermediate values were selected to add resolution to the data set.

This initial test found that vortex shedding did not occur for AR = 0.5 and 0.25 within 1000 seconds given these test conditions. Therefore these aspect ratios were eliminated from the study. Figure 26 demonstrates the vorticity at 1000 seconds for both aspect ratios. Both demonstrate symmetric boundary layers that do not separate at the aft end

Table 7. U_{red} test points used to find VIV regimes for each AR considered

AR	U_{red} values selected for each simulatoin; Re = 100, M_{red} = 10														
0.25	1	2	3	4	5	6	7	8	9						
0.5	1	2	3	4	5	6	7	8	9						
0.7	1	2	3	4	4.5	5	5.5	6	7	8	9				
1	1	2	3	3.5	4	4.5	5	5.5	6	7	8	9			
1.43	1	2	3	4	4.5	4.8	5	5.5	6	6.5	7	8	9		
2	1	2	3	3.5	3.8	4	4.5	5	5.5	6	7	8	9		
4	1	2	3	3.5	3.8	4	4.2	4.4	4.8	5	5.5	6	7	8	9

.

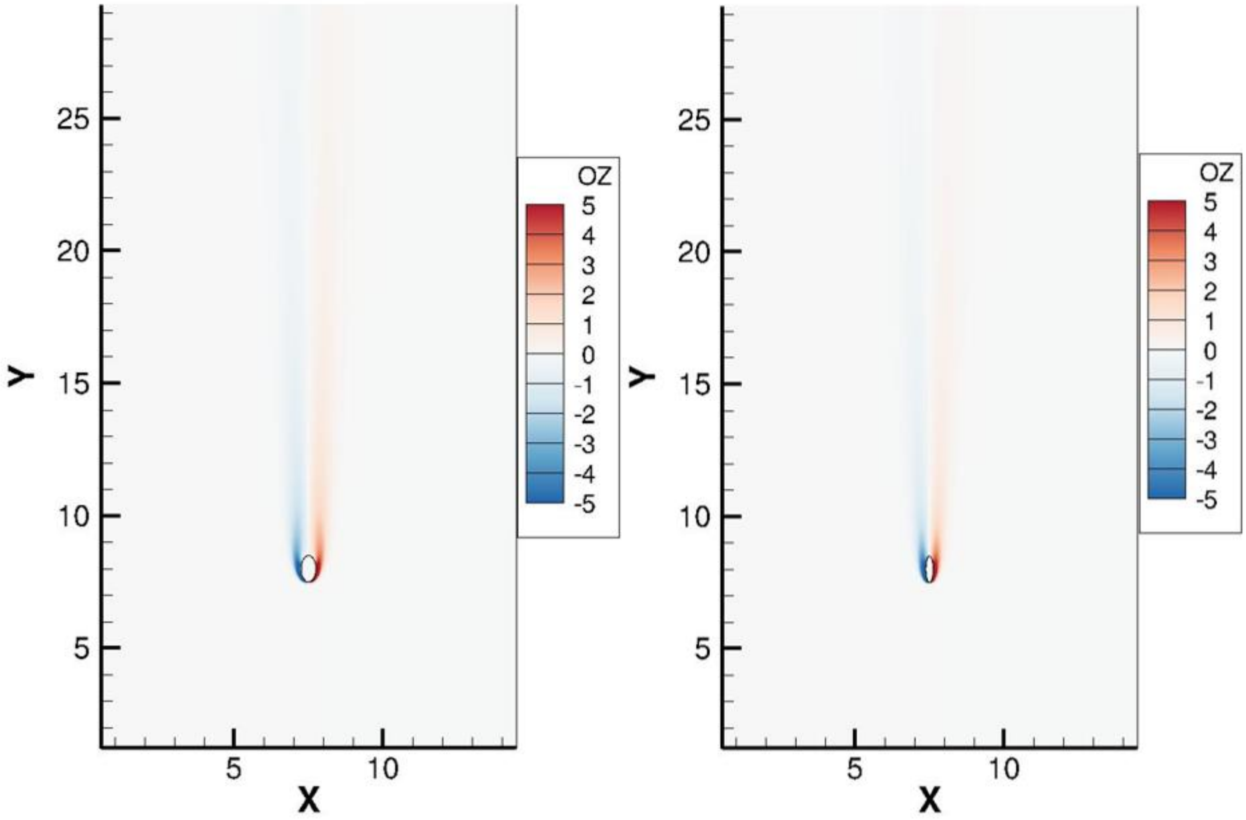

Figure 26. Vorticity plot of AR = 2 (left) and AR = 4 (right) at time step 100000 (1000 seconds). Re = 100, U_{red} = 5.

Once the VIV regimes are established from the U_{red} sweeps, a U_{red} is selected within the lock-in and flexible regimes for each aspect ratio. These are the U_{red} values listed next to each AR in Table 8. Then, simulation with increasing *Ri* are conducted in search of Ri_c. Like Table 7, the *Ri* value used for each simulation is listed across the table at the given AR and U_{red}. These test points were used to find Ri_c. Initially, six test points were simulated between *Ri* = 0.2 and 1.2. Then intermediate test points were added to increase the data's resolution near where Ri_c appeared to be. Any trends Ri_c as a function of AR will be noted as an outcome of this study.

Table 8. *Ri* test points used to find Ri_c for each AR in the lock-in and flexible regime

AR	U_{red}	*Ri values used for each simulation* to find Ri_c														
0.7	5	0.05	0.1	0.15	0.2	0.3	0.4	0.6	0.8	1						
	8	0.05	0.1	0.15	0.2	0.3	0.4	0.6	0.8	1						
1	5	0.2	0.25	0.275	0.3	0.35	0.4	0.45	0.5	0.6	0.8	1	1.2			
	8	0.1	0.15	0.2	0.25	0.3	0.4	0.6	0.8	1	1.2					
1.43	5	0.2	0.25	0.3	0.325	0.35	0.375	0.4	0.6	0.8	1	1.2				
	8	0.2	0.25	0.3	0.325	0.35	0.375	0.4	0.6	0.8	1	1.2				
2	4.5	0.2	0.4	0.5	0.525	0.55	0.5525	0.5575	0.575	0.6	0.8	1	1.2			
	8	0.2	0.4	0.45	0.5	0.525	0.55	0.555	0.575	0.6	0.8	1	1.2			
4	4.5	0.2	0.4	0.6	0.8	1	1.025	1.05	1.075	1.1	1.125	1.15	1.175	1.2	1.3	1.5
	8	0.2	0.4	0.6	0.8	1	1.025	1.05	1.075	1.1	1.125	1.15	1.175	1.2	1.3	1.5

IV Results and Discussion

4.1 Overview

For this study, an elastically-mounted, elliptical cylinder that is allowed to oscillate perpendicular to the free stream flow (*x*-direction). The cylinder and flow are simplified to a 2-D cross section in a flow confined to the same plane. Although the body is allowed to translate, the cross section is assumed to be rigid. Additionally, temperature is added as a second parameter in the control of vortex-induced vibration. As demonstrated in Figure 21 from section 3.3, a uniform freestream enters from the bottom of the domain space and flows to the top, parallel to the direction of gravity. The cylinder is subject to transverse virbations in the x-direction as a result of vortex shedding. The cylinder surface is heated to a uniform, constant temperature, effects of temperature induced buoyance are studied.

The Reynolds number is 100 and the reduced mass M_{red} is 10 to coincide with parameters in the VIV study performed by Navrose *et al*. [8]. M_{red} can be transferred to the density ratio ρ_s/ρ_f. The reduced mass 10.0 roughly corresponds to solid steel in a liquid water medium, which is common in physical application. Recalling Eq. 5:

$$M_{red} = \frac{m_{body}}{\rho_{fluid}\, D^2}$$

And noting that the hydraulic diameter is defined by Eqns. 35 and 36 as:

$$D = \frac{4ab(64 - 16E^2)}{(a+b)(64 - 3E^4)} \tag{35}$$

where

$$E = \frac{a-b}{a+b} \tag{36}$$

Variables *a* and *b* are defined by half the major and minor axis respectfully as demonstrated in Figure 25 from section 3.6. Table 9 shows the density ratio used for each aspect ratio.

Table 9. Density ratios by AR

AR	$\frac{\rho_s}{\rho_f}$
0.7	12.14565559
1	12.73239545
1.43	12.14247567
2	10.71004966
4	6.830706866

4.2 Comparison of Vortex-Induced Vibrations at Various Reduced Velocity

First, each aspect ratio will be subject to flow until reaching stead-state without being heated. This process will be repeated at various reduced velocities, representing structures of different rigidities. This will be done by changing the natural frequency of the structure as seen in a vacuum (f_{vac}). As U_{red} increases, the natural frequency of the structure decreases. Initially, the U_{red} is tested at integer values between 1 – 9. Intermediate tests are added until the lock-in region and flexible region are clearly established. At each test case, A_x, C_L, C_D, and f_{ex} will be monitored to observe how the body is responding to the flow. These values are shown in a summary of results completed for each simulation. This is shown in Figure 27, below.

Plot A shows the transient motion (Ax/D) in blue and the lift coefficient (C_L or Cx) in red. By including the transient response, one use this plot to see if the lift and motion are in phase, determine the magnitude of these values, and determine if the forcing function is in phase with the motion. It is important to note that the plot uses a dual *y*-axis since the magnitude of values may differ between the lift coefficient and amplitude. The amplitude will be the one of the primary values used to determine which VIV regime the body is in.

Plot B shows the transient response of the drag coefficient (C_D or C_Y) in blue. Additionally, the minimum, maximum, and mean steady state values are plotted as shown in the legend. In the title, the mean drag and the range is reported along with the RMS value. These valued help determine the magnitude of the drag coefficient as well as how much it is oscillating. The RMS captures the amount of oscillation from the mean value best, and can aid in determining if the body is within the lock-in region. A high RMS value indicates a high amount of oscillation within the drag coefficient, which is due to well defined vortex shedding. The frequency of the steady state C_D signal is double that of the C_L when vortex shedding is present signal since each shed vortex generates a cycle while a pair of shed vortices is needed to generate one lift cycle.

Plot C shows the results from a power spectral density (PSD) analysis on the lift and amplitude signals. This plot shows the gain as the dependent variable and the frequency, in Hz, as the independent variable. This analysis is the method used to determine the excitation frequency of the body (f_{ex}). The frequency is found by selecting the frequency of which the peak amplitude gain is found, and the value is shown in the plot's title. Knowing the natural frequency of the system from the U_{red} selected, the frequency ratio of the excitation frequency and the natural frequency can be found. A ratio close to unity represents a body within lock-in. It is important to note that a frequency ratio of unity will not find the U_{red} with the peak amplitude unless M_{red} is sufficiently large. This is because the resonance response frequency in water is different than in a vacuum due to the additional mass of the fluid within the boundary layers surrounding the body. This will be demonstrated within the results for each aspect ratio.

Plot D represents a phase diagram between the lift coefficient and the body motion. By plotting the two variable against themselves, it can be determined if the lift and motion are in phase. A positive correlation shows the relationship as in-phase and a negative correlation shows the relationship is out of phase. This can also be seen in plot A, but is more clearly shown in plot D. From the literature, it is expected that the phase will shift from in phase at the leading into the lock-in region, to out of phase about half way through the lock-in region. It is desired that the U_{red} selected within the lock-in region, be selected such that the lift and motion are in phase. This will ensure the suppression study scrutinizes high amplitude scenarios. Likewise, it is expected that the flexible region selections will show and out of phase relationship. Combined, plots A-D give a general overview of how the body is reacting to the flow, and this information can be used to determine which VIV regime the body is experiencing.

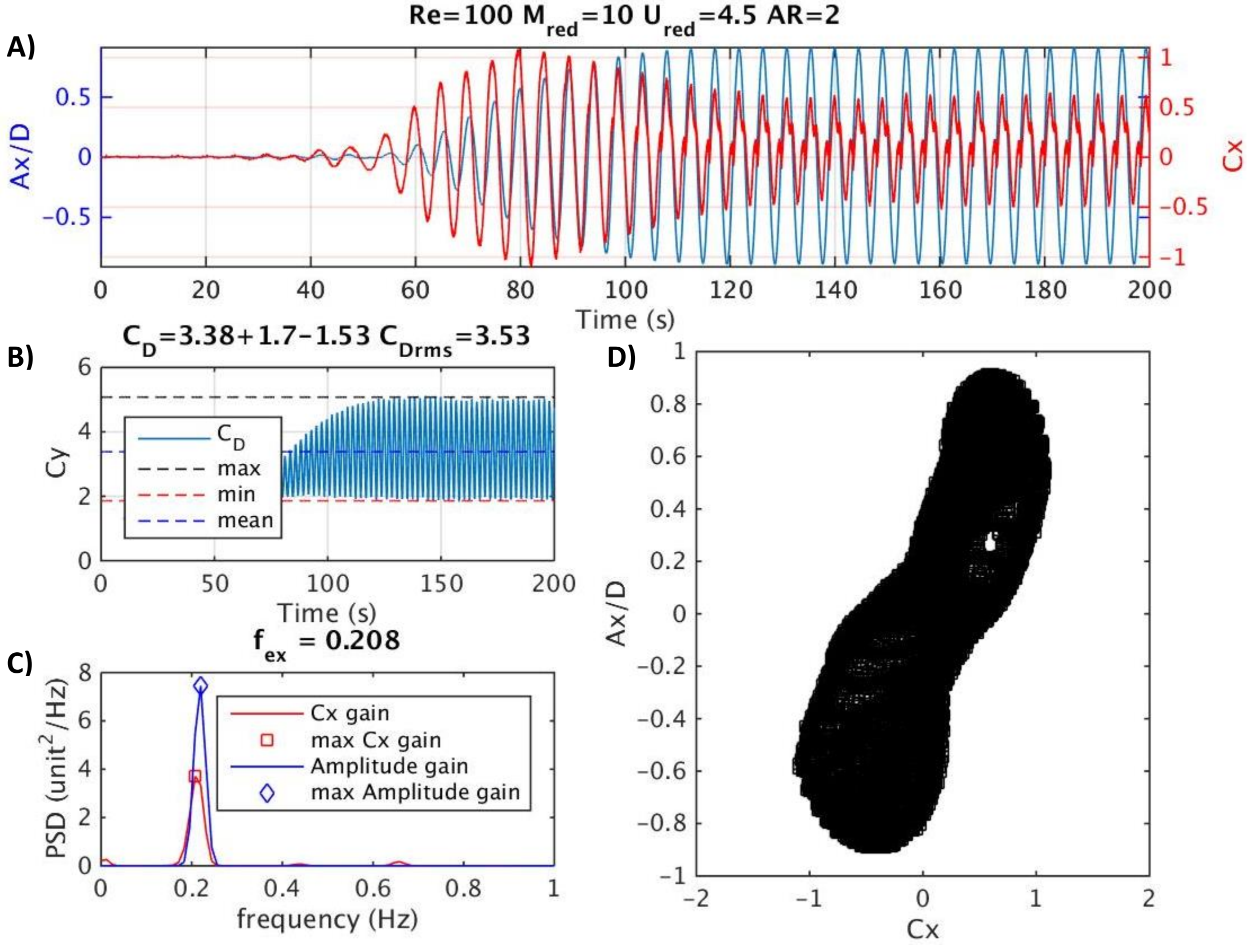

Figure 27. Sample summary of results for a single U_{red} simulation.

4.2.1 Reduced Velocity Sweep for AR = 0.7

Starting with the smallest aspect ratio, simulations of varying reduced velocities were ran to steady-state. The steady-state amplitude, frequency ratio, and C_{Drms} was recorded for each simulation and plotted against U_{red}. Figure 28 offers a comparison between the results from this study and that completed by Navrose *et al.* [8]. Although the resolution of the plots in this study is not as resolved as the data collected by Navrose, (as it in itself is not the objective of this thesis) the comparison shows that similar results were found. Additionally, the model used by Navrose used a ramping *Re*, where the *Re* was held constant for each study in this simulation, so an aggregate of their two curves is used for comparison. It is also important to note that the model used by Navrose allowed for motion in the *x* and *y*-directions, which allows the drag force to have a large hand in the body motion. Therefore, the amplitudes reported by Navrose are slightly different than those found by the present study, but not different by a large margin.

Both simulations showed the leading edge of lock-in occurring when U_{red} is slightly greater than 4 and the flexible region occurring when U_{red} is greater than 6. Therefore, the studies are in agreement that the lock-in region can be defined as between $4.2 < U_{red} < 6$. A similar comparison was shown in Figure 18. The frequency ratio plot and the C_{Drms} plot also confirm that the lock-in region is in this range. The peak amplitude found by both studies is found to be about 0.3. Notice, the peak amplitude at $U_{red} \approx 4.2$ corresponds with a frequency ratio slightly less than 1 as predicted. However, the frequency ratio of 1 does fall within the lock-in region at $U_{red} \approx 5$. Within the frequency plot, there is an outlier data point when $U_{red} = 1$. When the body was simulated as very stiff, the motion amplitude was near zero and the resolution of the motion output was too coarse to accurately represent the motion. Therefore, the PSD study struggled to get an accurate reading of the frequencies within the signal.

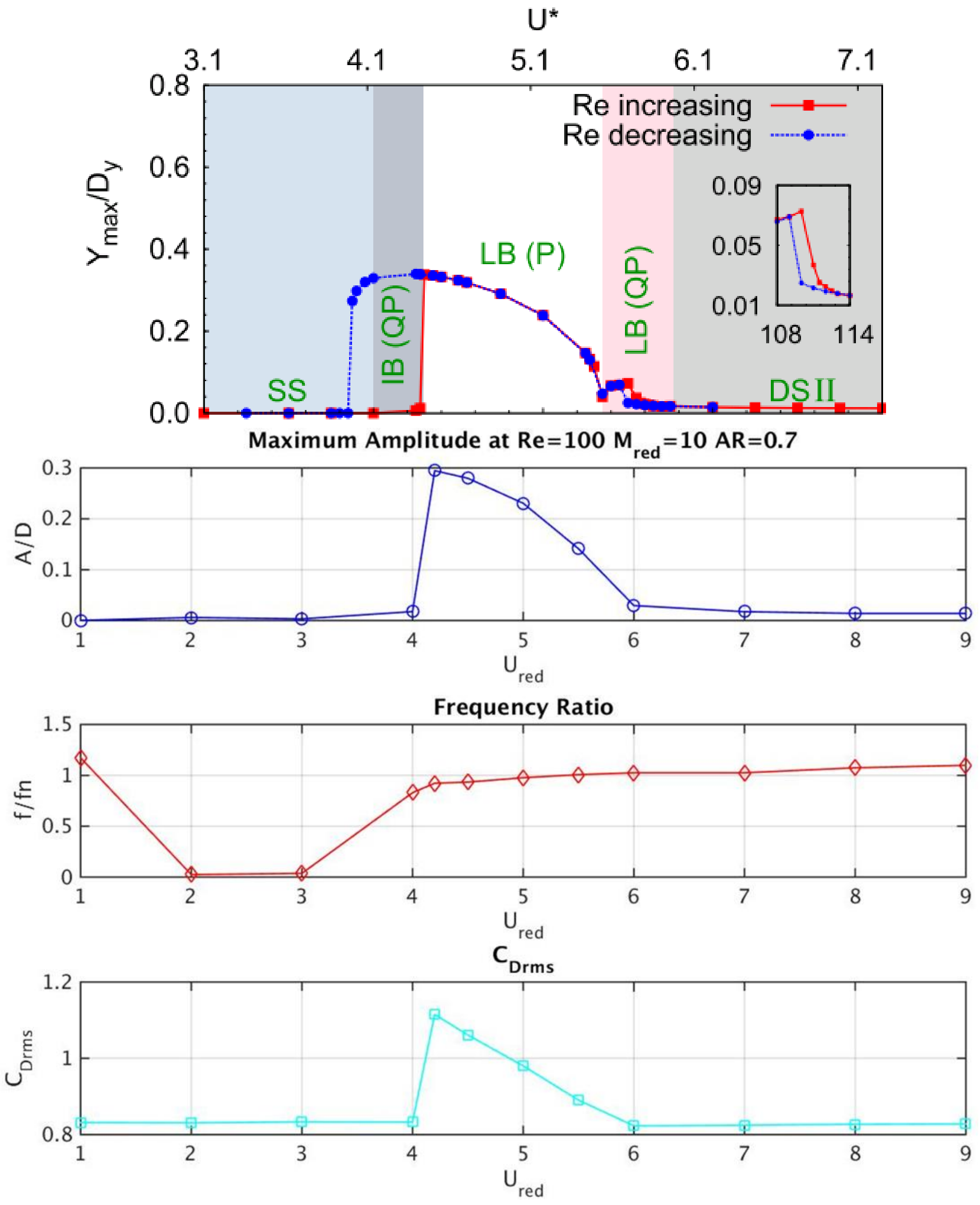

Figure 28. U_{red} sweep results for AR=0.7. Top plot is the amplitude results from Navrose et al [8]. Second, third and fourth plot shows the steady-state amplitude, frequency ratio, and C_{Drms} respectively from the present study.

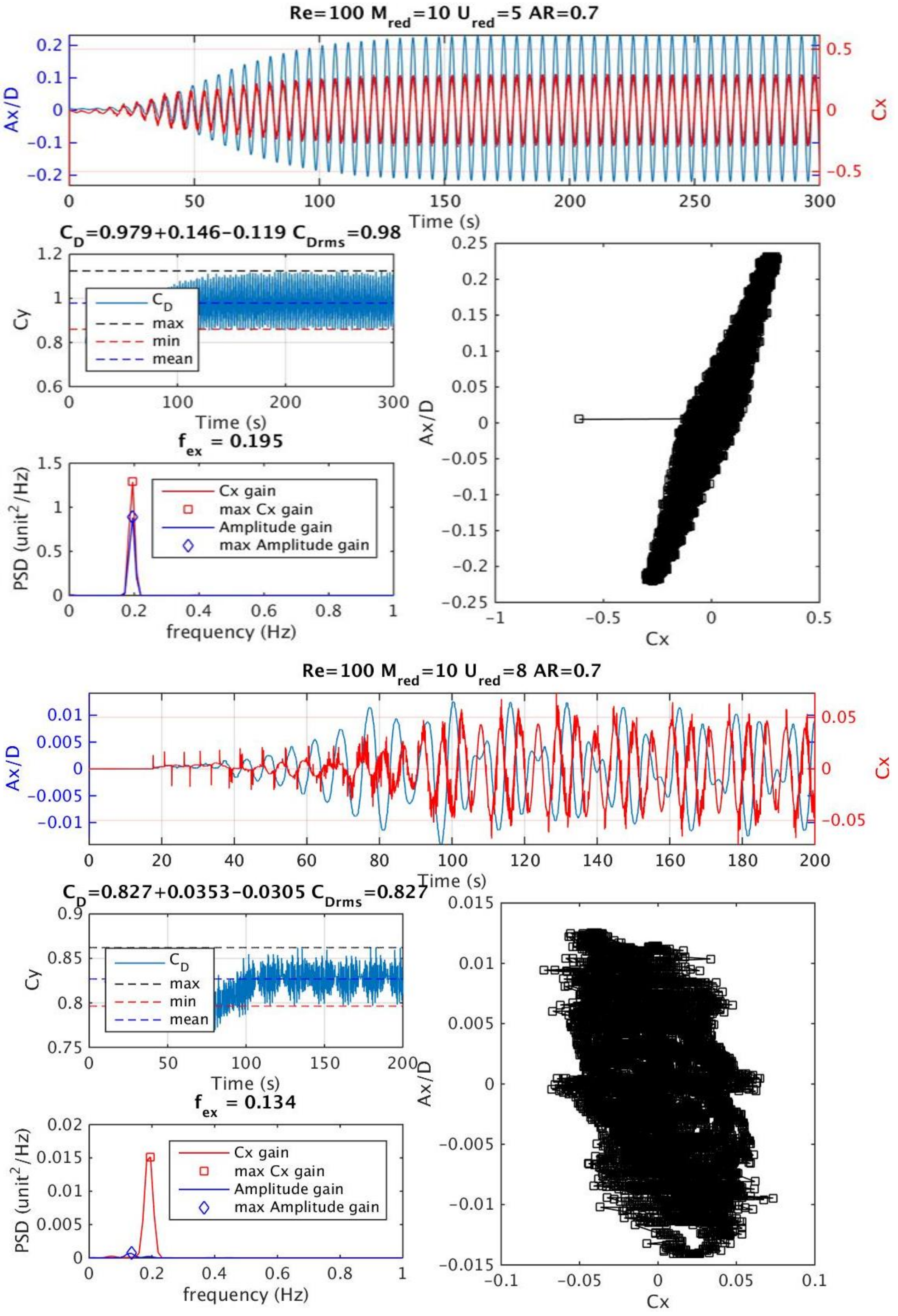

Figure 29. Summaries of simulations collected within lock-in at U_{red} = 5 (top) and the flexible region when U_{red} = 8 (bottom).

Figure 29 presents the detailed data summaries of a point within the lock-in and flexible regimes at U_{red} = 5 and 8 respectively. The top summary shows how the lift and motion signals are in phase and are clearly defined, which is expected within the lock-in region. The bottom summary shows how the motion is now two orders of magnitude smaller and the lift and motion signals are out of phase. This aspect ratio is unique in that, when in the flexible region, the influence of the natural frequency causes beating in the lift, drag, and motion signals. The influence of the natural frequency, shows up in the PSD plot, as the peak amplitude power is at 0.134 Hz and is not aligned with the peak lift frequency. This causes there to be little correlation between the lift and motion signals as seen in the phase diagram.

Additionally, the aliasing exists in the plots due to the motion output resolution being 0.001 D. The solver carries more significant figures, so this problem is isolated to the output plots. The small steps in the transient phase are clear indicator that aliasing exists.

Figure 30, below, shows a visualization of the flow for the lock-in regime (left) and the flexible regime (right). The plot shows the vorticity where the blue represents velocity changes indicative of clockwise rotation and red represents velocity changes indicative of counter-clockwise rotation. The deeper the color, the higher the change in velocity is. A high spatial change in velocity correlates to high shear.

The most noticeable features are the high amounts of shear along the surface of the body. This boundary layer formation is expected for laminar, viscous flow. Compared to the other aspect ratios in this study, the vortex separation in the wake is small for both regimes. This coincides with the finding that the motion amplitude for this AR is also the smallest in the study. Since the body is relatively thin, there is less backflow in the wake, causing weak vortices to form compared to the wider aspect ratios.

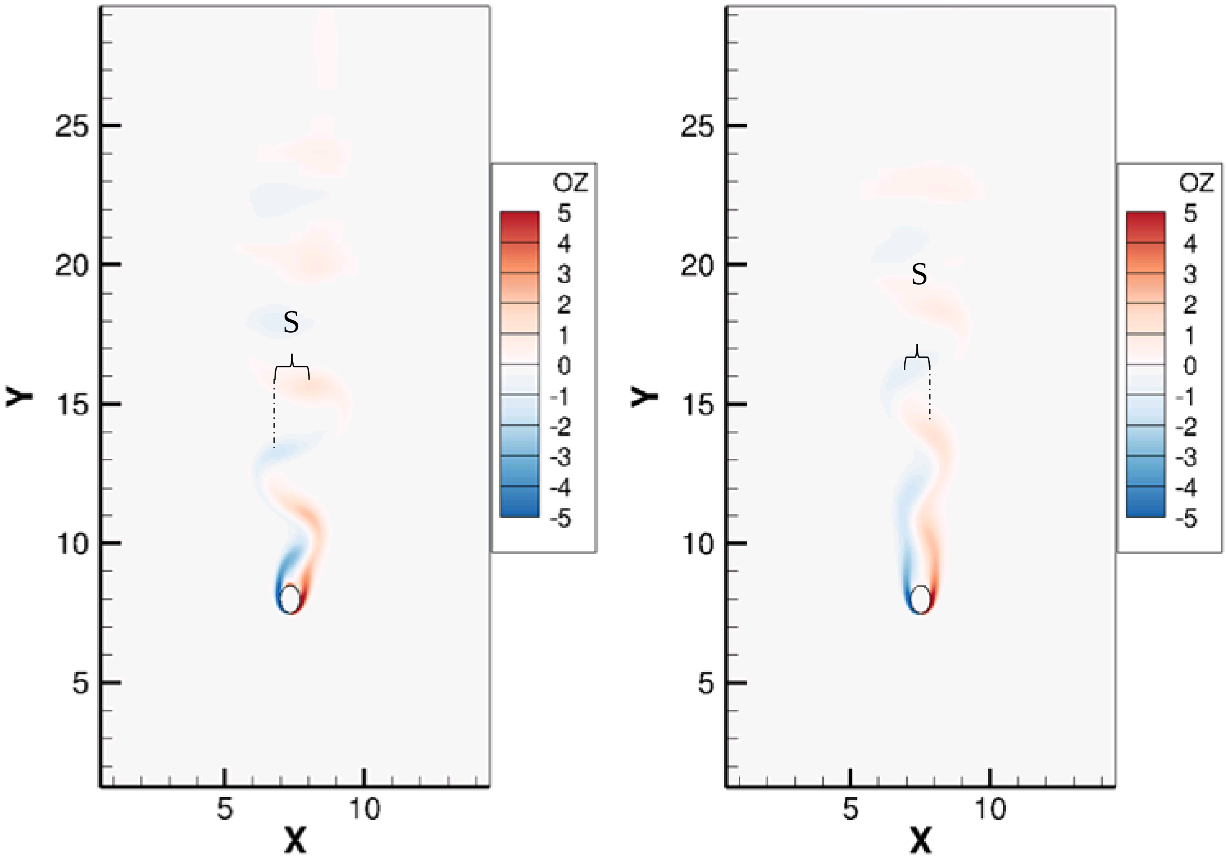

Figure 30. Flow visualization using vorticity. Vortex shedding is shown during lock-in (left) and the flexible regime (right). The vortex separation, S, is approximately 1.2 D for the lock-in regime and 1 D in the flexible region. AR = 0.7.

4.2.2 Reduced Velocity Sweep for AR = 1

The results of the U_{red} sweep for AR=1 are displayed in Figure 31, Figure 32, and Figure 33. Once again, the lock-in region is clearly defined by the motion amplitude, frequency ratio, and C_{Drms} plots and concurs with the results found by Navrose *et al*. [8]. The studies are in agreement that the lock-in region can be defined as between $5 < U_{red} < 8$ with a peak amplitude at about 0.6 D. Once again, summaries are presented for $U_{red} = 5$ and $U_{red} = 8$ to ensure values chosen to be within the lock-in and flexible regimes are acting as predicted by the literature.

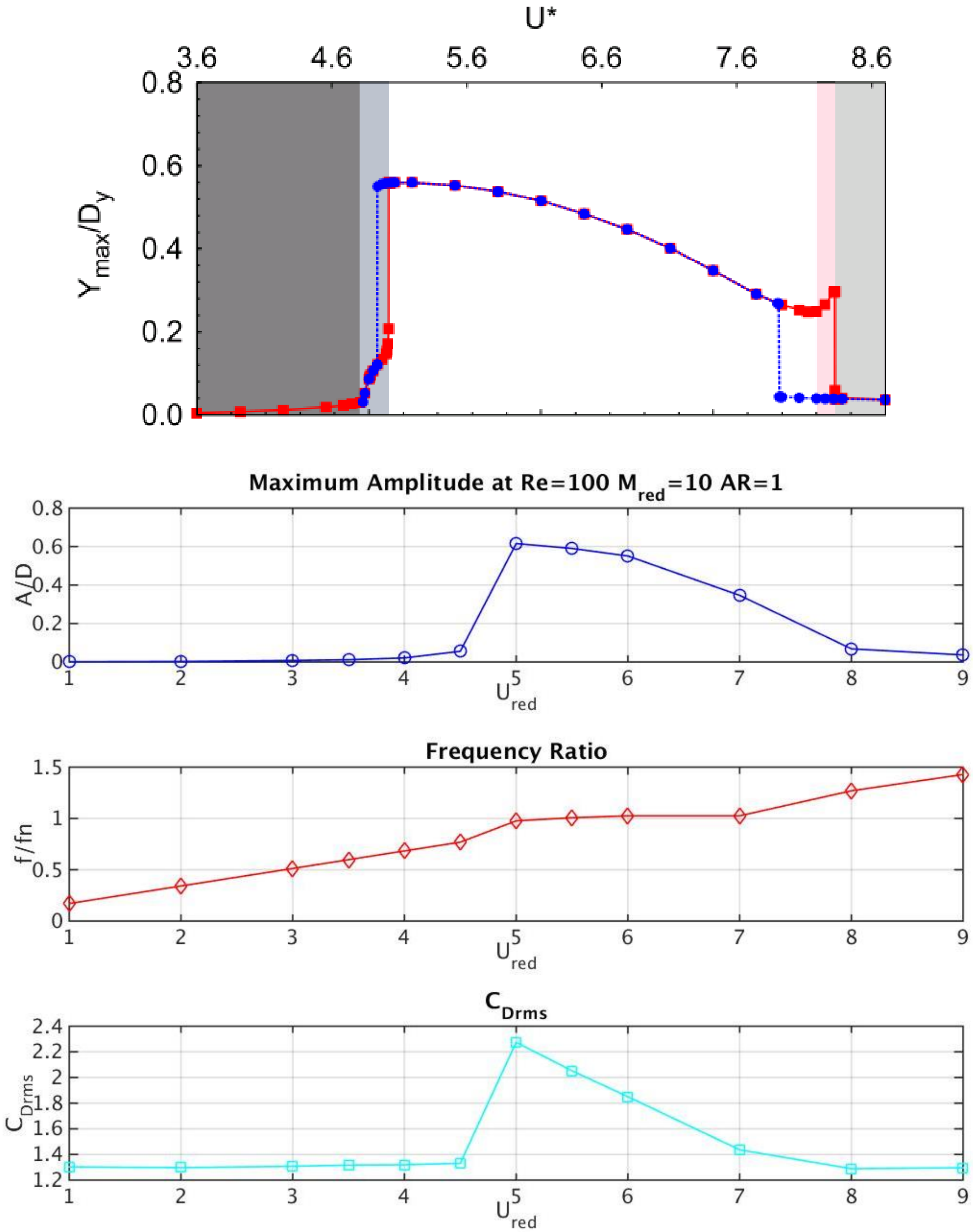

Figure 31. U_{red} sweep results for AR=1. Top plot is the amplitude results from Navrose et al [8]. Second, third and fourth plot shows the steady-state amplitude, frequency ratio, and C_{Drms} respectively from the present study.

At U_{red} = 5, the body response is at the peak of the lock-in regime. The phase diagram in Figure 32 (top) shows that the lift and drag are operating in phase. Additionally, the frequency ratio from Figure 31 is close to unity. This provides another example of the peak lock-in value operating a frequency ratio slightly offset from unity due to the added mass of the surrounding fluid. As expected, C_{Drms} also is at a maximum at U_{red} = 5. The flow visualization from Figure 33 demonstrates that the vortex separation is higher than seen in AR = 0.7. For the lock-in regime, the vortex separation is about 2 D as compared to 1.2 D. By visual inspection, the vortices are also more tightly formed than seen in the lock-in region for AR = 0.7.

At U_{red} = 8, the body response is at the beginning of the flexible region. The phase diagram in Figure 32 (bottom) shows that the lift and drag are operating out of phase. Despite the beating in the motion signal, a clear negative correlation between the motion and lift may be determined. The frequency ratio from Figure 31 has surpassed unity, limiting the effectiveness of the lift force on the body. The motion amplitude has reduced about an order of magnitude from peak lock-in (0.6 D to 0.07 D). The mean drag coefficient is also substantially lower, at 1.29 versus 2.21 at peak lock-in, as well as the RMS value. The flow visualization from Figure 33 demonstrates that the vortex separation is less than that observed in the lock-in region for the same AR. Subjectively, the vortices are also less tightly formed than seen in the lock-in region and takes more distance upstream to fully separate.

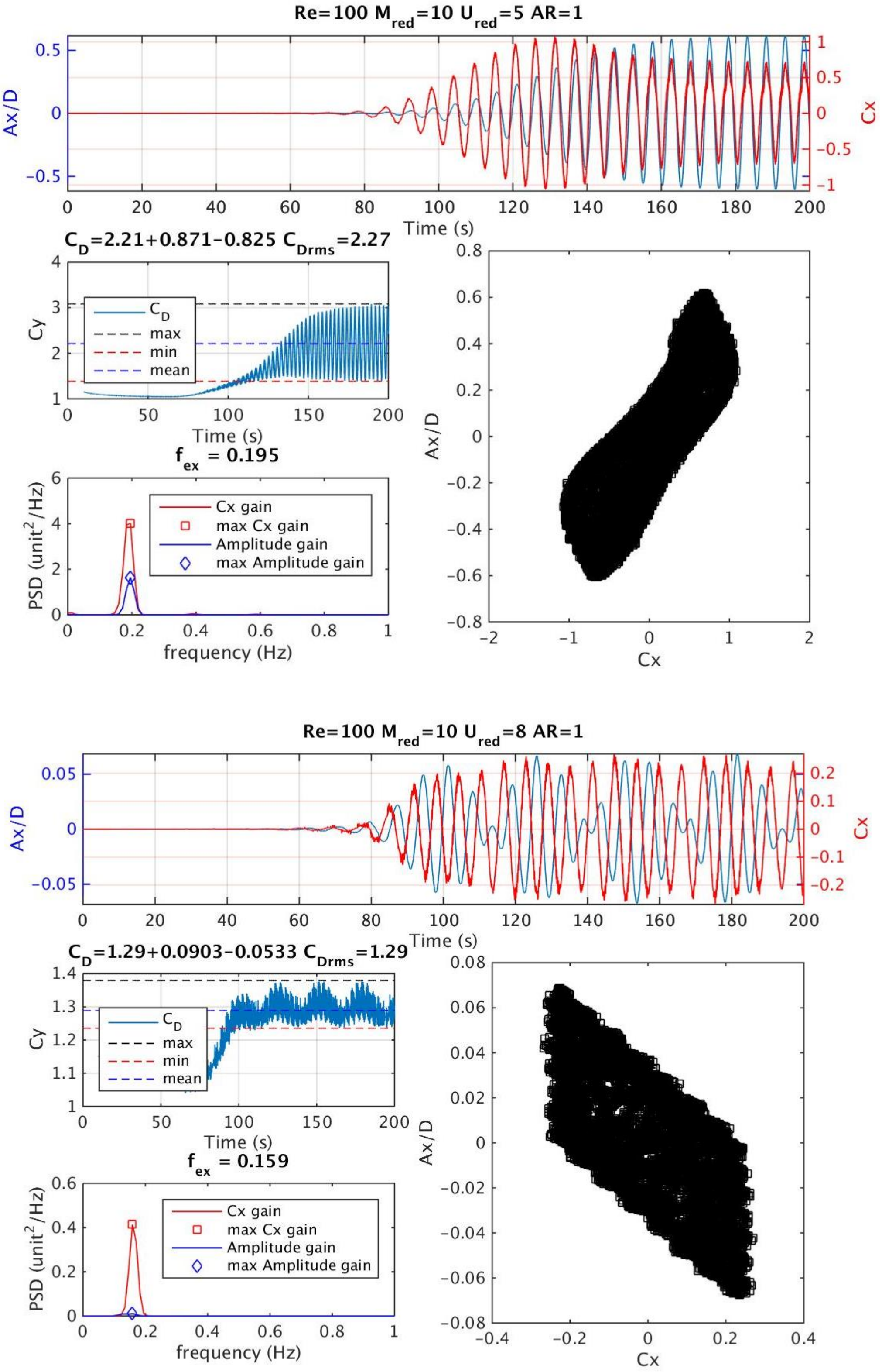

Figure 32. Summaries of simulations collected within lock-in at U_{red} = 5 (top) and the flexible region when U_{red} = 8 (bottom).

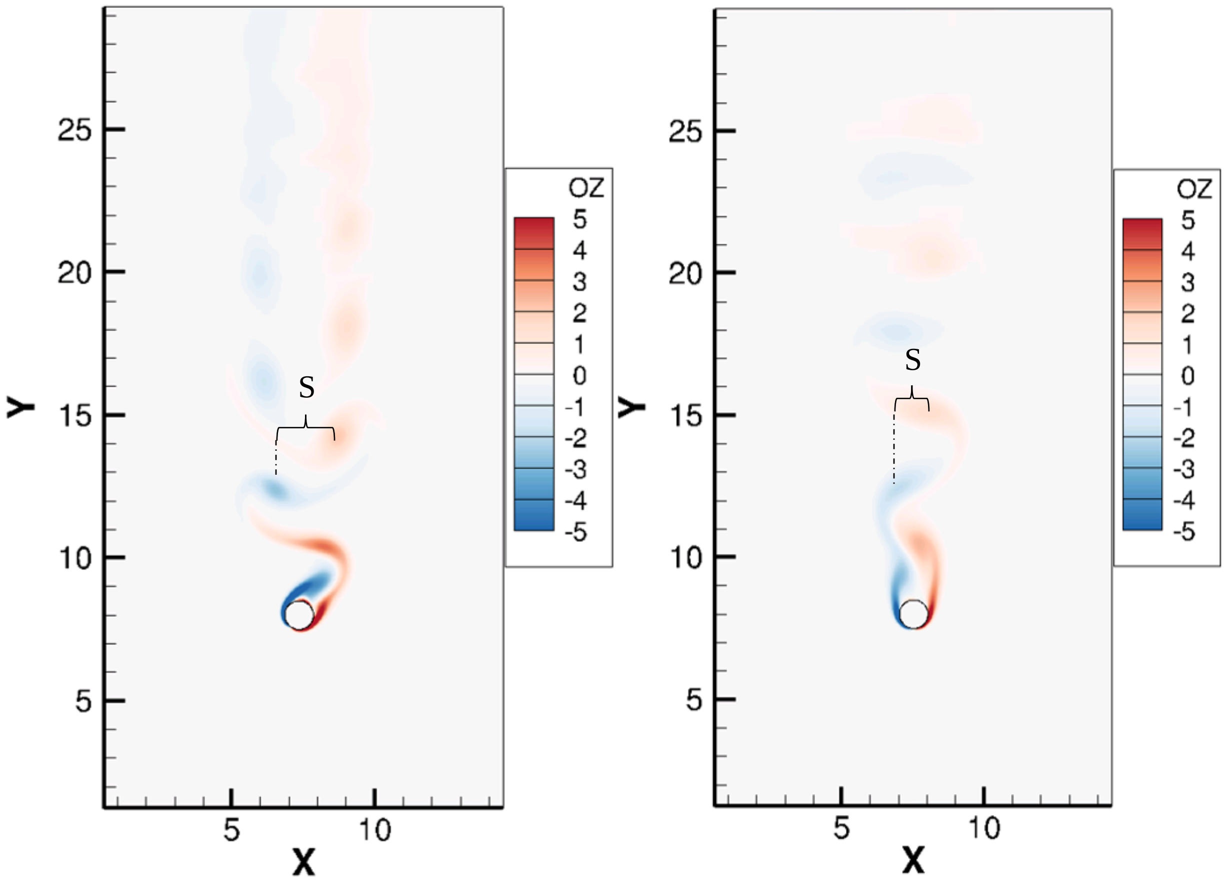

Figure 33. Flow visualization using vorticity. Vortex shedding is shown during lock-in (left) and the flexible regime (right). The vortex separation, S, is approximately 2 D for the lock-in regime and 1.2 D in the flexible region. AR = 1.

4.2.3 Reduced Velocity Sweep for AR = 1.43

The results of the U_{red} sweep for AR=1.43 are displayed in Figure 34, Figure 35, and Figure 36. The lock-in region is defined using the same methodology used for AR = 0.7 and AR = 1. The motion amplitude plot and concurs with the results found by Navrose *et al*. [8]. The studies are in agreement that the lock-in region can be defined as between $4.5 < U_{red} < 7$ with a peak amplitude at about 0.75 D. The summaries for $U_{red} = 5$ and $U_{red} = 8$ are selected for comparison and validation.

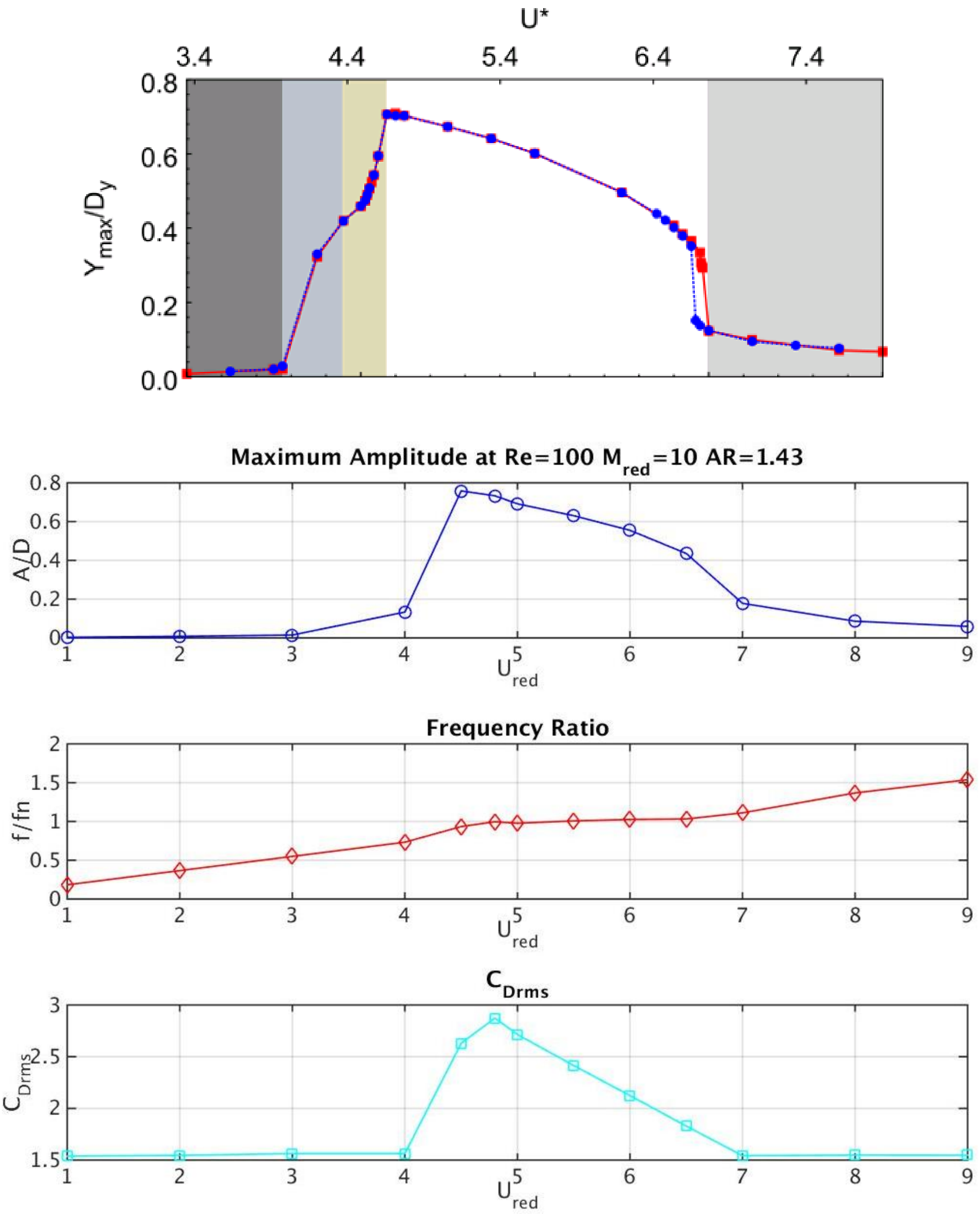

Figure 34. U_{red} sweep results for AR=1.43. Top plot is the amplitude results from Navrose et al [8]. Second, third and fourth plot shows the steady-state amplitude, frequency ratio, and C_{Drms} respectively from the present study.

At U_{red} = 5, the body response is slightly past the peak of the lock-in regime. The phase diagram in Figure 35 (top) shows that the lift and drag are beginning to shift out of phase, which is expected for a U_{red} midway through the lock-in regime. At this point, the frequency ratio from Figure 34 is at unity, where the peak value (U_{red} = 4.5) is operating a frequency ratio slightly less than unity like the other ARs. The flow visualization from Figure 36 continues to demonstrate that as the the vortex separation increases, so does the vibrational amplitude. The lock-in regime has a vortex separation of approximately 2.3 D as compared to 1.2 D and 2 D for AR = 0.7, 1 respectively.

At U_{red} = 8, the body response is well into the flexible region. The phase diagram in Figure 35 (bottom) confirms that the lift and drag are operating out of phase. The beating in the signal has reduced compared to the signals seen for AR = 1, and the phase has a stronger, negative correlation. Similar to the previous aspect ratios, the motion amplitude has reduced about an order of magnitude from peak lock-in (0.75 D to 0.09 D). The mean drag coefficients continue to support that the higher body velocities create higher drag coefficients. For AR = 1.43, $\overline{C_D}$ reduces from 2.62 at peak lock-in to 1.55 in the flexible regime. The flow visualization from Figure 36 demonstrates that the vortex separation approximately the same as the separation for the flexible regimes of AR = 0.7 and 1. The vibrational amplitudes are on the order of 0.1 D and vortex separation are approximately 1 D for each of the simulations. The lock-in values do not share the same trend, as the peak amplitude has increased from 0.3 D to 0.75 D between AR = 0.7 and AR = 1.43. Likewise, the vortex separation has nearly doubled from 1.2 D to 2.3 D between the two aspect ratios.

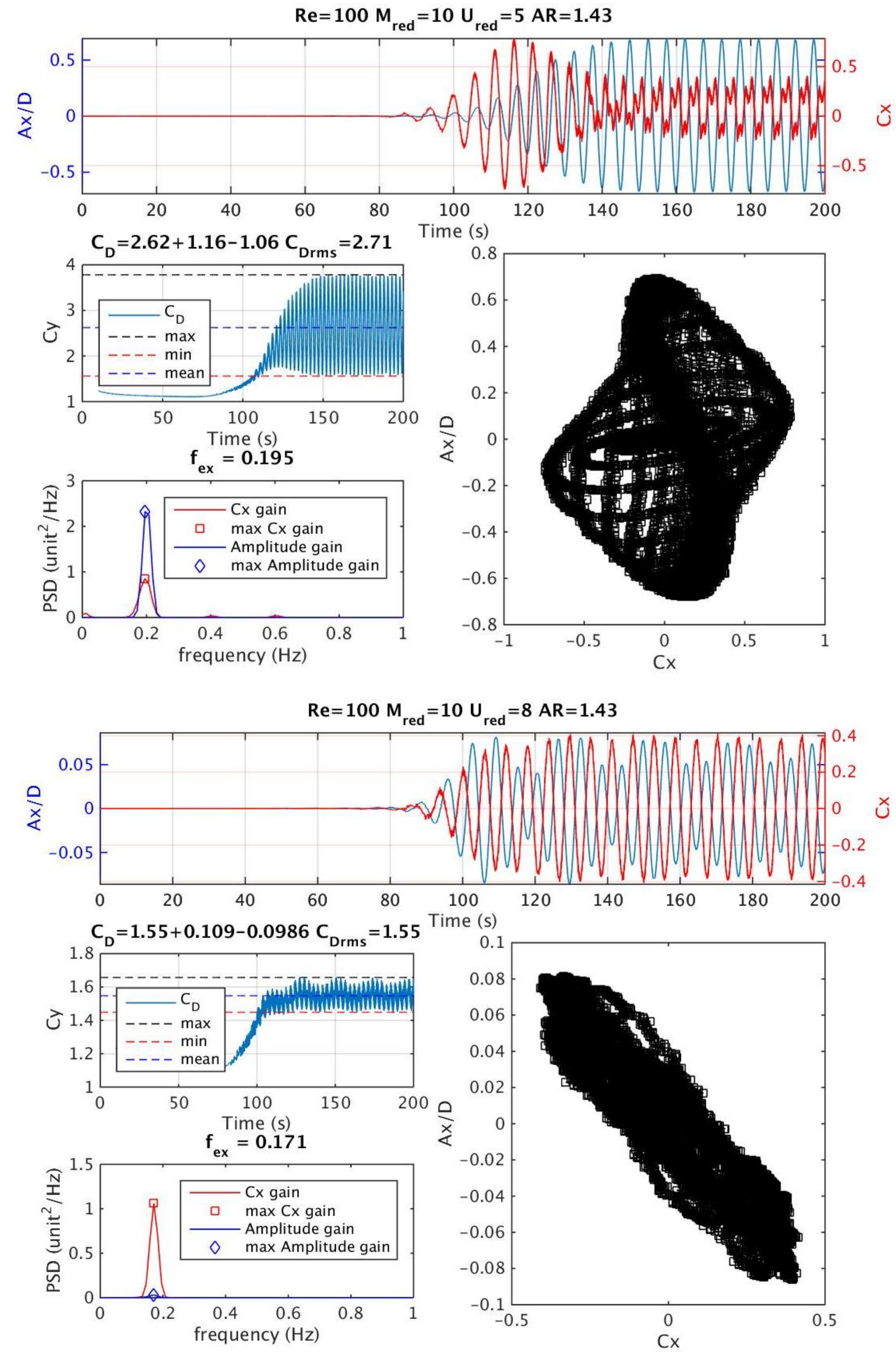

Figure 35. Summaries of simulations collected within lock-in at U_{red} = 5 (top) and the flexible region when U_{red} = 8 (bottom).

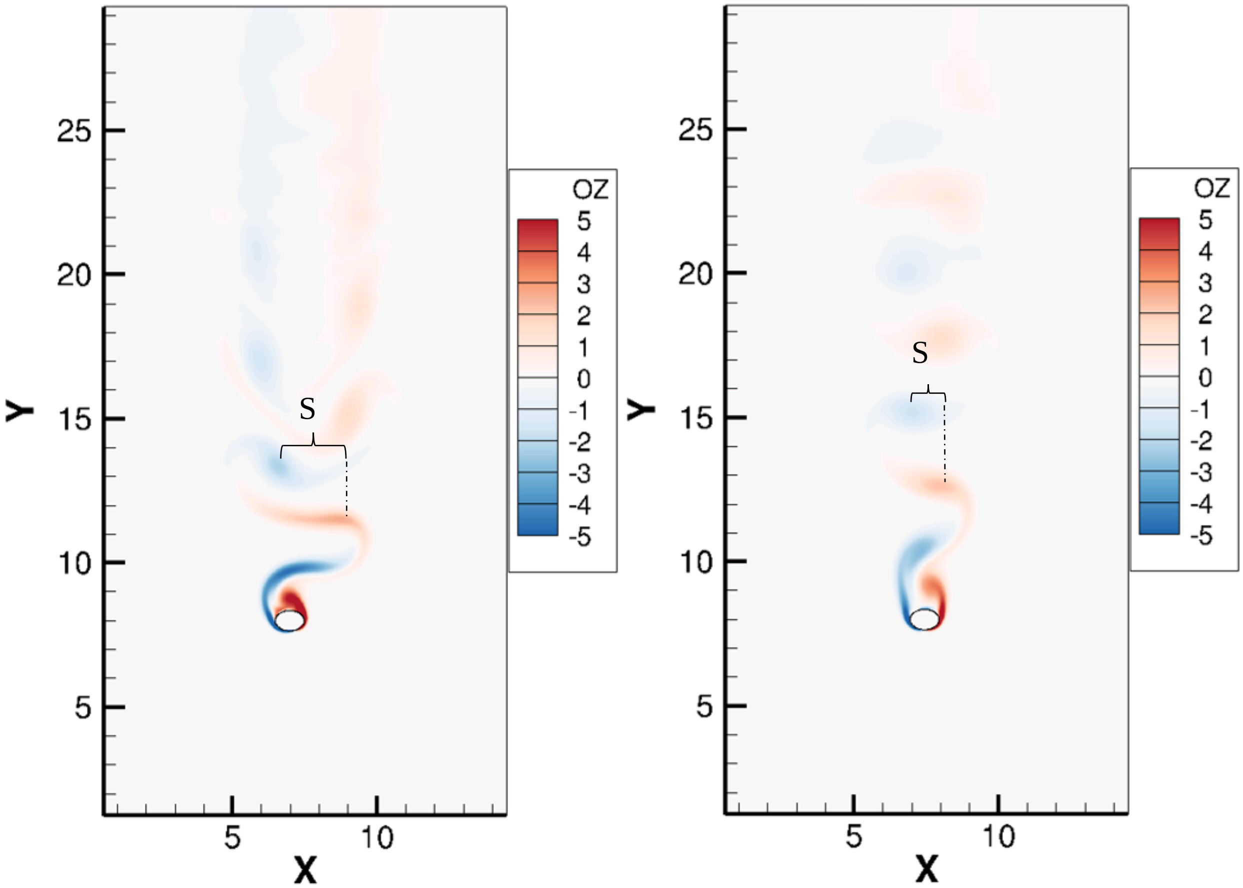

Figure 36. Flow visualization using vorticity. Vortex shedding is shown during lock-in (left) and the flexible regime (right). The vortex separation, S, is approximately 2.3 D for the lock-in regime and 1.2 D in the flexible region. AR = 1.43.

4.2.4 Concluding Remarks from Comparison

These three ARs (0.7, 1, and 1.43) conclude the comparison and validation process of the solver used against the findings of Navrose *et al.* (2014) [8]. There were several differences between the two models, yet the results were nearly identical. This validates that using a 1-DOF model sufficiently represent the transverse motion, as adding motion parallel to the flow yielded little difference in the results. Navrose *et al.* also used a ramping *Re* to alter U_{red} as opposed to changing the stiffness of the body and leaving *Re* a constant. Their *Re* varied between 60 and 140 while the present study held *Re* constant at 100. Since dimensionless parameters are used, this validates that the same vortex shedding modes are exhibited for the same U_{red}, so long as the *Re* is within the laminar region. Finally, two different mathematical models were used for numerical simulation. Navrose *et al*. used a finite element method detailed in Tezduyar, Behr, and. Mittal (1992) [54] where the present study used the finite volume methods described in Chapter III. These comparison validate the model for elastically mounted elliptical cross section and give confidence extending the model to simulate aspect ratios 2 and 4.

4.3 Extended Vortex-Induced Vibrations Studies for AR = 2 and 4

The same evaluation methods used for aspect ratios 0.1, 1, and 1.43 were extended to 2 and 4. Figure 37 shows the steady-state amplitude and frequency ratio as U_{red} is varied. Referring back to Figure 31 and Figure 34 the initial branches (seen in the grey and tan regions in the plots produced by Navrose *et al*) widen from AR = 1 to AR = 1.43. This trend continues to the higher aspect ratios. The amplitude plot from Figure 37 clearly show the initial branches widening from $3 < U_{red} < 4$ for AR = 2 to about $2.5 < U_{red} < 4.2$ for AR = 4. The transition to the flexible regime, however, remains fairly consistent. At $U_{red} = 8$, both ARs have amplitudes on the order of 0.1 D, which is consistent with the previously studied aspect ratios. The peak lock-in amplitude continues to increase from approximately 0.9 D for AR = 2 to 1.1 for AR = 4. At the higher aspect ratios, the frequency ratio is essentially unity at the peak amplitudes, which differs from the lower aspect ratios. This is because the cross section thickness perpendicular to the direction of motion is much thinner, like an airfoil. Therefore, the added mass of the fluid is significantly lower and the resonance frequency is essentially the natural frequency in the vacuum. As expected, the mean drag continues to increase for both the lock-in and flexible regions as the AR increases. The flow visualizations in Figure 38 show that vortices continue to separate and tighten as AR is increased, and is indicative of the vibrational amplitudes to increasing. Table 10 consolidates the results from the U_{red} sweeps.

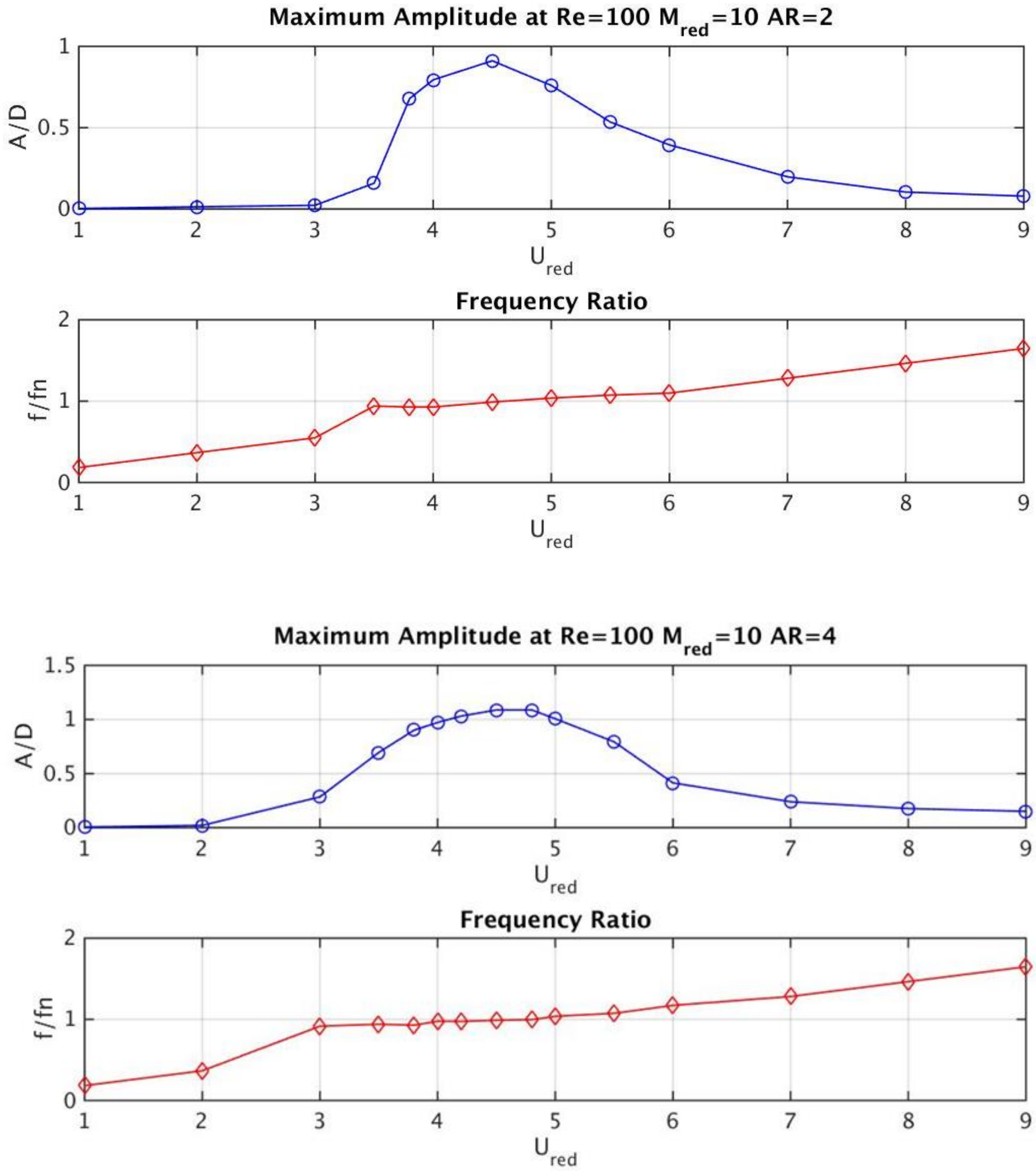

Figure 37. U_{red} sweep results for AR = 2 (top) and AR = 4 (bottom).

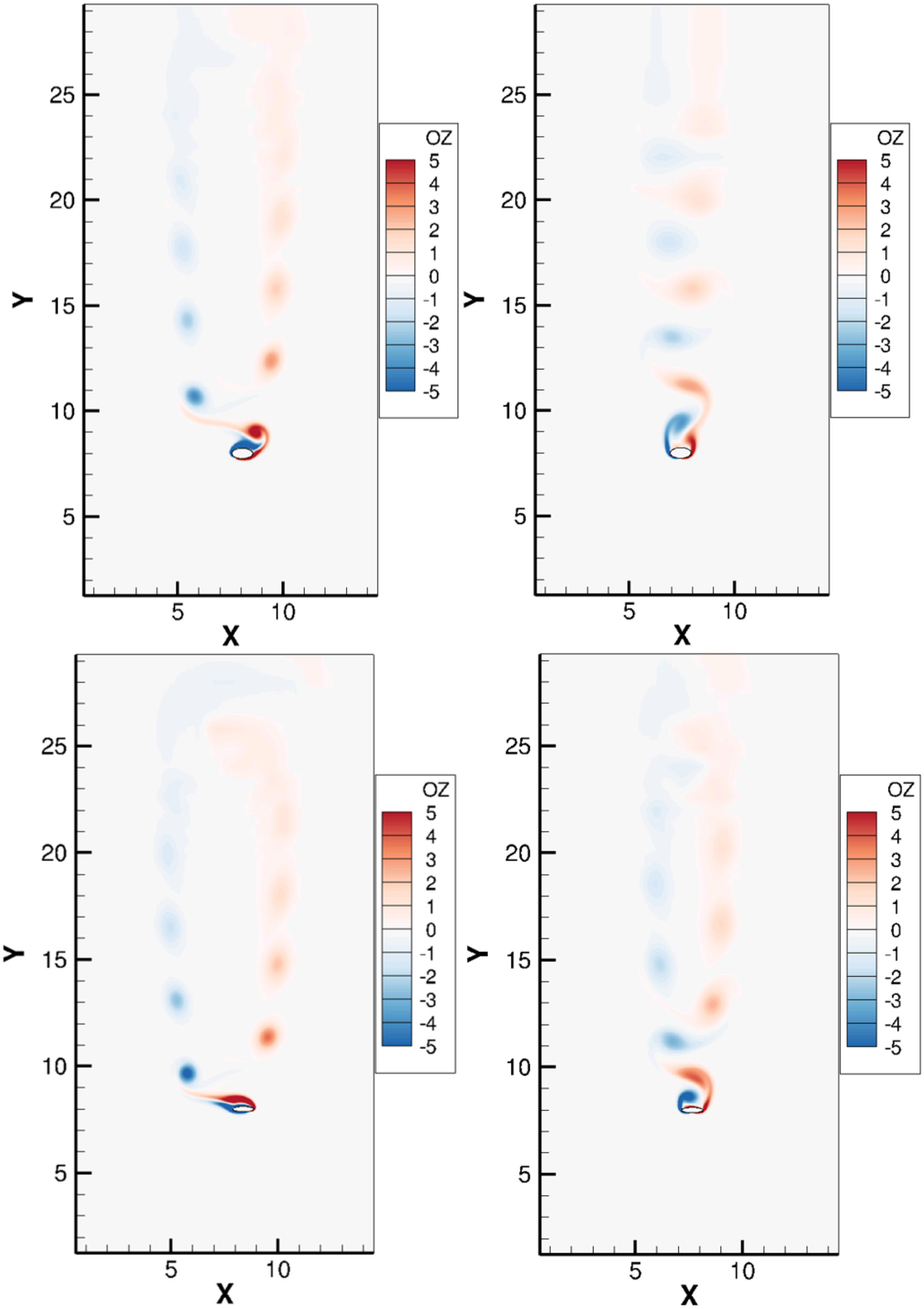

Figure 38. Flow visualizations using vorticity for AR = 2 (top) and AR = 4 (bottom). The left plots are the bodies at lock-in (U_{red} = 4.5) and the right plots are the bodies within the flexible regimes (U_{red} = 8).

Table 10. Consolidated U_{red} Sweep Results

		Lock-in regime				Flexible regime			
AR	Lock-in range (U_{red})	A/D max	C_{Lmax}	$\overline{C_D}$	C_{Drms}	A/D	C_{Lmax}	$\overline{C_D}$	C_{Drms}
0.7	4.2 – 6	0.3	0.3	0.9402	0.956	0.015	0.07	0.827	0.827
1	5 – 8	0.6	1.1	2.1898	2.27	0.7	0.3	1.29	1.29
1.43	4.5 – 7	0.75	1.6	2.6457	2.71	0.9	0.4	1.55	1.55
2	4.5 – 6	0.9	1.2	3.3958	3.53	0.095	0.5	1.85	1.85
4	4.5 – 6	1.1	0.7	4.2123	4.28	0.16	0.55	2.34	2.34

4.4 Suppression Using Thermal Effects

The principle behind suppression using thermal effects is to see if the fluid surrounding the body can produce sufficient buoyant forces to elevate the vertical component of velocity and recede the separation point aft on the body. This is best shown in Figure 39. The velocity diagram shows how the heated fluid (shown in the temperature diagram) is accelerated to nearly double the freestream velocity due to thermal-induced buoyant forces. Ideally, the vortices are altered such that they do not separate and stay bound to the body. This will eliminate any oscillatory fluid dynamic forces experienced by the body and subsequently eliminate any vibrations.

Now that the fluid-body interaction for each AR has been characterized, thermal effects are added to the simulations to evaluate if suppression can be achieved. To do so, a U_{red} is selected within the lock-in and flexible regimes for each aspect ratio. It is desired that lock-in region suppressed since it is the worst-case scenario for structure. The flexible regime is also modeled for comparison. Each U_{red} selected is shown in Table 11. They are held constant throughout a series of simulations operating at various *Ri*s. Each simulation is ran to steady state. Initially, simulations were ran at *Ri* = 0.2, 0.4, 0.6 0.8, 1 and 1.2. Intermediate simulations were added to increase resolution where Ri_c seemed to be located. A summary of the tests completed are included in Table 8 from Chapter III.

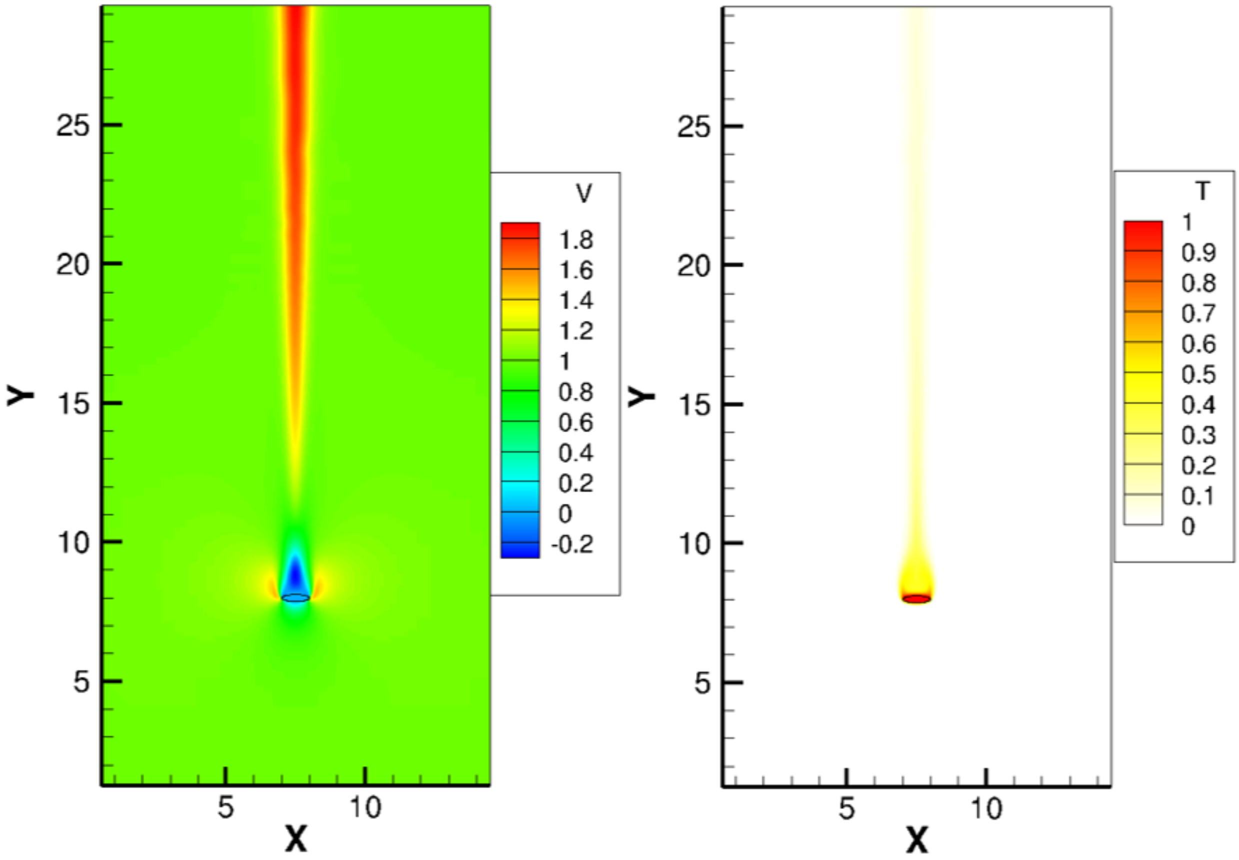

Figure 39. (left) Thermal effects due to buoyant forces as seen by the vertical component of velocity. The freestream velocity is 1 (green). (right) Temperature increase of flow due to convection. The freestream temperature is zero (white). The heated temperature fluid is accelerated due to buoyant forces created from a change in density. AR = 4, Ri = 1.15, U_{red} = 4.5, M_{red} = 10, Re = 100, Pr = 7 t = 190s.

Table 11. U_{red} selections to simulate suppression within the lock-in and flexible regimes

AR	Lock-in regime	Flexible regime
0.7	5	8
1	5	8
1.43	5	8
2	4.5	8
4	4.5	8

Now that heat transfer is being considered, the Prandtl number (Pr) must be considered. Pr is a dimensionless number representing the ratio of momentum diffusivity to thermal diffusivity and is expressed as $Pr = \upsilon/\alpha$, where υ is the kinematic viscosity and α is the thermal diffusivity of the fluid. For water at room temperature (293 K), $Pr \approx 7$. This will be the value used for all the simulations involving heat transfer. It is important to note that Pr for water does change significantly temperature, so this value should be altered when considering modeling for high or cold temperature applications.

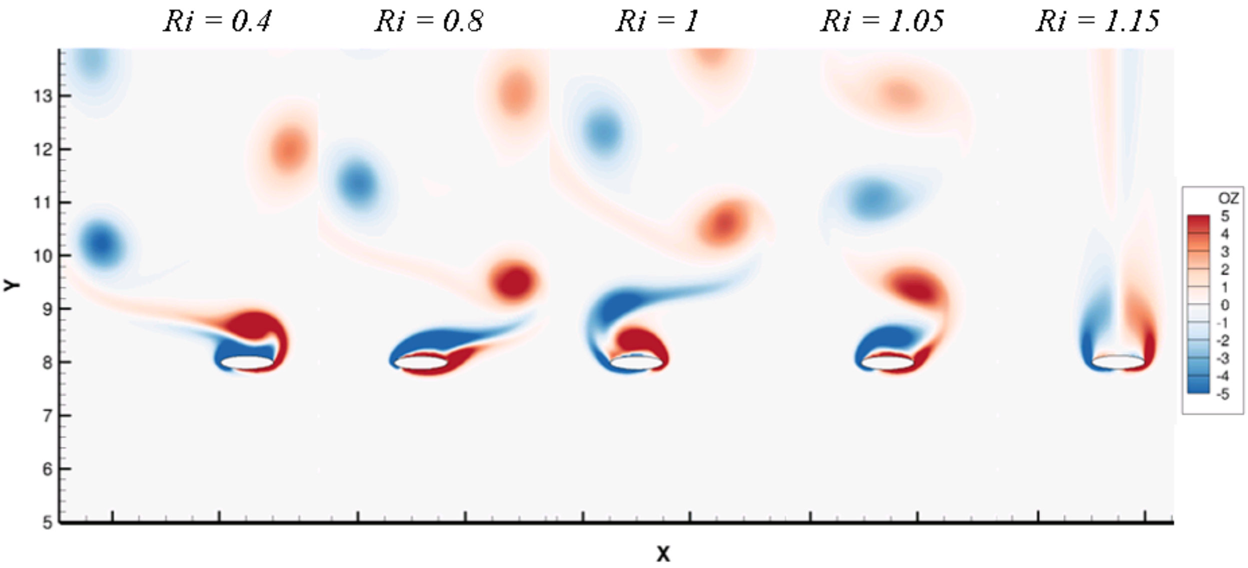

Figure 40. Flow visualization using vorticity where AR = 4. *Ri* is increased until *Ri*$_c$ is reached at *Ri* = 1.15. At *Ri*$_c$, bound vortices have replaced the shed vortices. As *Ri* is increased, the vortex separation decreases until vortex shedding is suppressed. U_{red} = 4.5, M_{red} = 10, *Re* = 100, *Pr* = 7.*t* = 200s

Table 12. Summary on critical Richardson number and time averaged drag coefficient $\overline{C_D}$ *Re* = 100, *Pr* = 7, M_{red} =10

AR	U_{red}	Ri_c	$\overline{C_D}$ at $Ri = 0$	$\overline{C_D}$ at Ri_c	$\overline{C_D}$ reduction (%)
0.7	5	0.15	0.9402	0.9153	2.6
1	5	0.25	2.1898	1.3754	37.2
1.43	5	0.375	2.6457	1.5916	39.8
2	4.5	0.6	3.3958	1.8977	44.1
4	4.5	1.175	4.2123	2.5246	40.1

Figure 40 demonstrates how increasing *Ri* decreases the vortex separation in the near wake until vortex shedding is suppressed altogether at Ri_c. Once Ri_c is achieved, the vortices remain bound to the aft edge, and vibrational motion is suppressed.

Although increasing *Ri* reduces vortex shedding and vibrational motion, a penalty in drag occurs by increasing the shear stress at the body's surface. The drag reduction due to a reduction in motion may outweigh the drag increase due to heat transfer. This is the case for all of the aspect ratios operating at a stiffness within lock-in. Table 12, above, lists the mean drag coefficient at $Ri = 0$ and Ri_c for each AR at their lock-in U_{red}. The drag reduction percentage is listed in the final column. The reduction varied for each aspect ratio but was approximately 40% for all ARs greater than or equal to 1. The maximum reduction was found with AR = 2 at 44%. The minimum reduction was found at AR = 0.7 at only 2.6%. This aspect ratio was an outlier in this regard. While

Once the vibrational motion is suppressed, the drag coefficient was found to rise. In fact, the drag coefficient for an AR with both a lock-in and flexible stiffness maintained the same drag coefficient at a given *Ri* once both bodies had suppressed vortex shedding. This agrees with the findings of Wan and Patnaik (2016) [7].

Prior to reaching Ri_c, the trends in drag coefficient are different for the flexible body. For all aspect ratios, the drag coefficient begins to increase as *Ri* is increased. For AR = 1.43, 2, and 4, after a period of drag coefficient increase, the drag coefficient begins to decrease until it reaches a local minimum. This decrease occurs as the amplitude drops off at a faster rate. After the motion is suppressed the drag coefficient increases thereafter. For AR = 0.7 and 1, the drag coefficient always increases. However, the rate of drag coefficient increase is significantly less as the motion reduction increases. Once the motion is suppressed, the drag coefficient increases at an faster rate. The *Ri* where the local minimum, or point of slope increase, coincides with the *Ri* of complete or near-complete suppression (A<0.01D). Therefore, a critical Richardson number can also be determined for the flexible regime. The suppression as a function of *Ri* is graphically represented in Figure 41 - Figure 45 below. The curves representing the lock-in regions are in blue, while the curves representing the flexible regimes are in red. The top plot of each figure shows the steady state amplitude as a function *Ri*. The bottom plot shows the mean drag coefficient as a function of *Ri*. The graphs may be used to visually justify where Ri_c is located for each AR in the lock-in and flexible regimes.

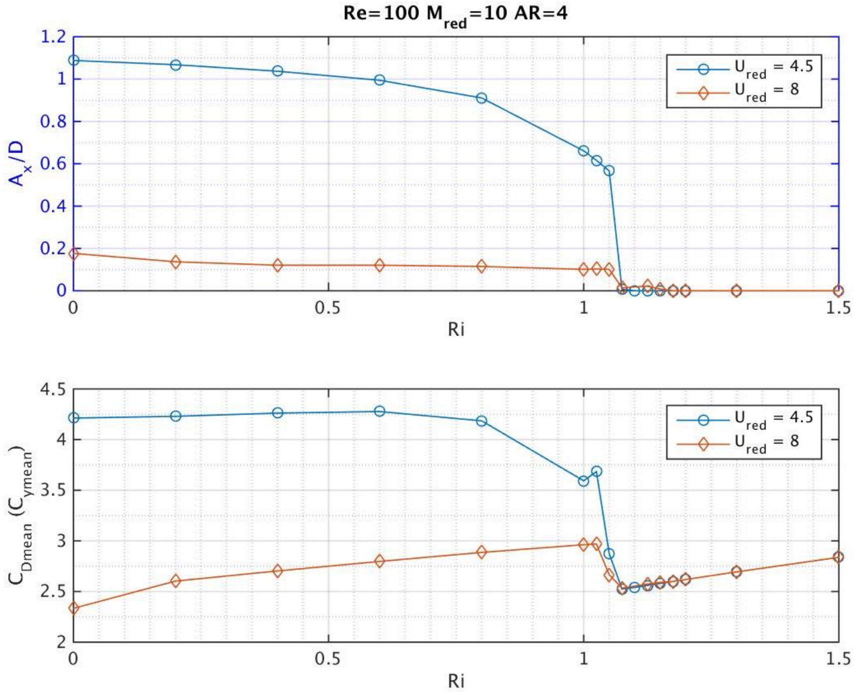

Figure 41. (Top) Steady state motion amplitude for the lock-in and flexible regime as *Ri* is varied. (Bottom) Mean drag coefficient for the lock-in and flexible regime as *Ri* is varied. AR = 4

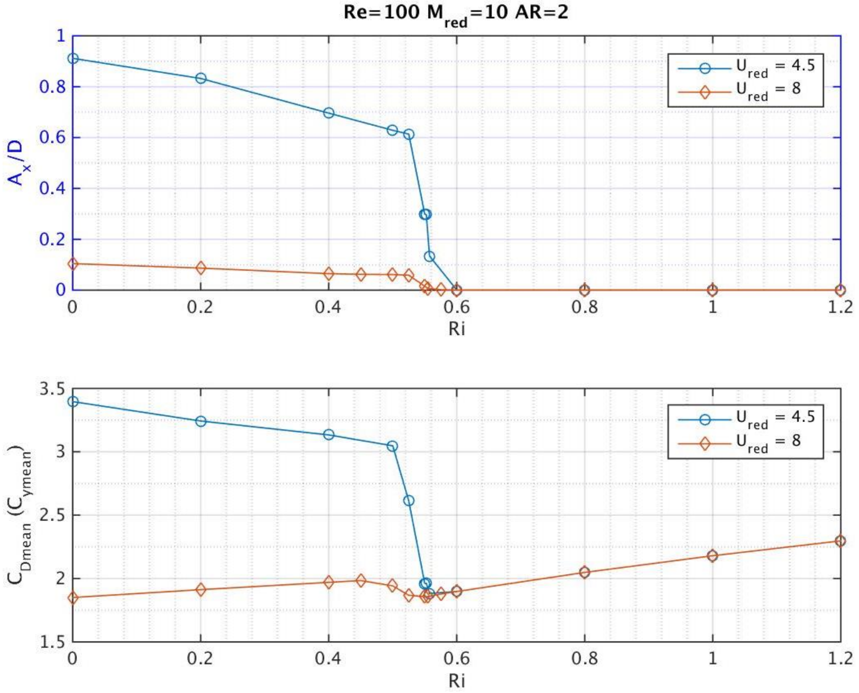

Figure 42. (Top) Steady state motion amplitude for the lock-in and flexible regime as *Ri* is varied. (Bottom) Mean drag coefficient for the lock-in and flexible regime as *Ri* is varied. AR = 2

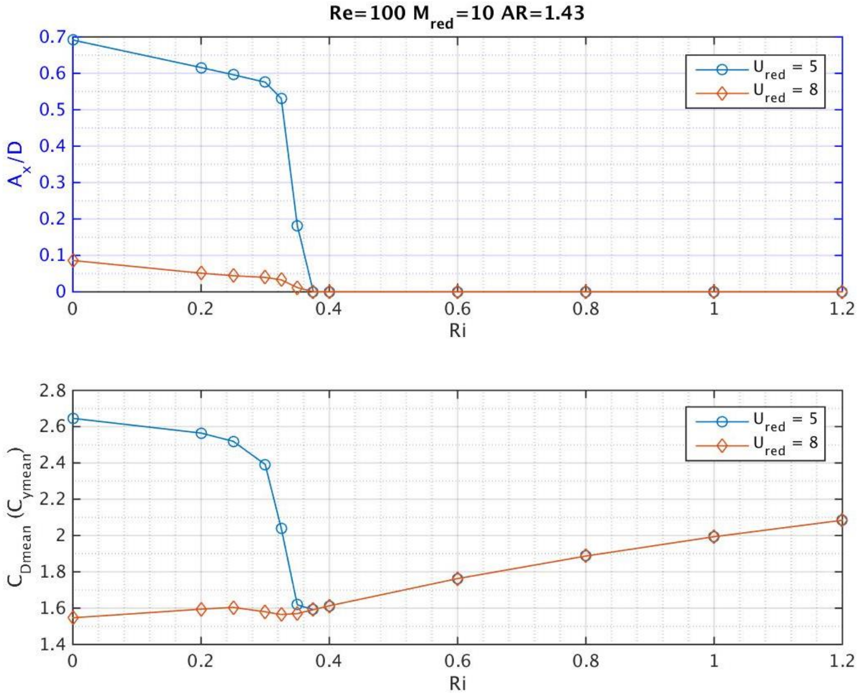

Figure 43. (Top) Steady state motion amplitude for the lock-in and flexible regime as Ri is varied. (Bottom) Mean drag coefficient for the lock-in and flexible regime as Ri is varied. AR = 1.43

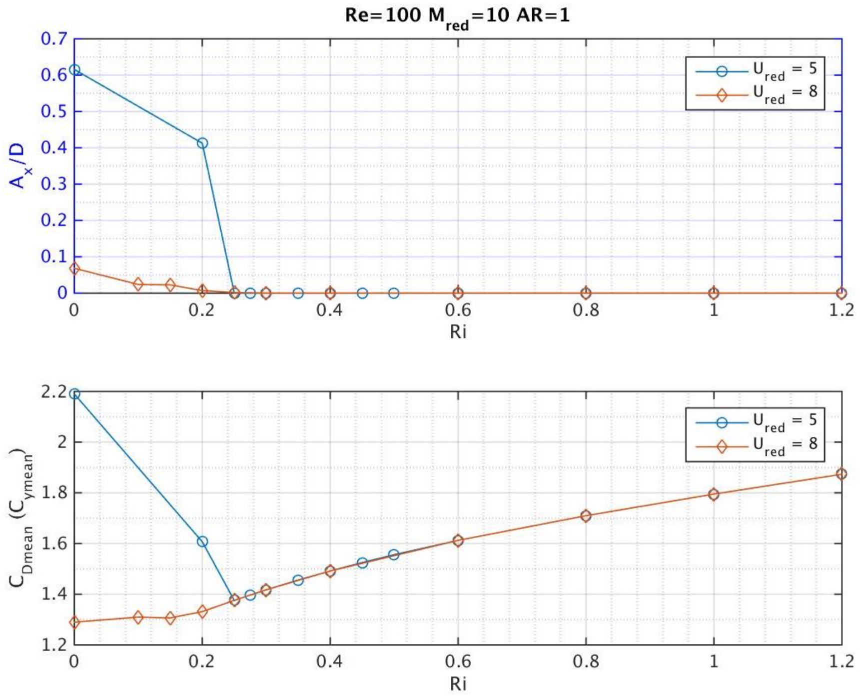

Figure 44 (Top) Steady state motion amplitude for the lock-in and flexible regime as *Ri* is varied. (Bottom) Mean drag coefficient for the lock-in and flexible regime as *Ri* is varied. AR = 1

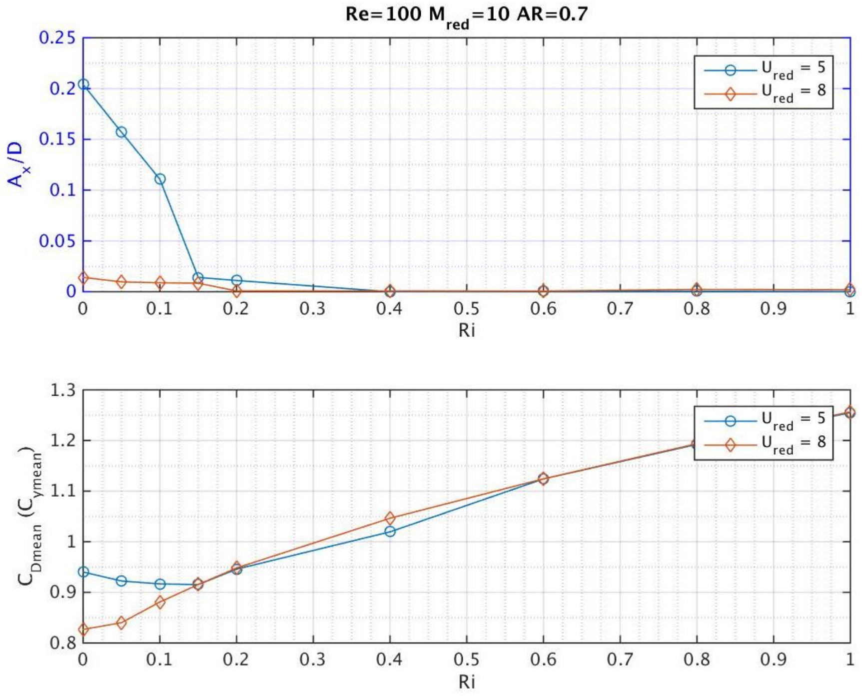

Figure 45. (Top) Steady state motion amplitude for the lock-in and flexible regime as *Ri* is varied. (Bottom) Mean drag coefficient for the lock-in and flexible regime as *Ri* is varied. AR = 0.7

Figure 46 shows the trend in Ri_c as a function of the aspect ratio. As the aspect ratio increases, the Ri_c increases linearly for both the lock in and flexible region. Since the unsuppressed amplitudes increased as AR increased, it was expect that more heat would be needed to suppress the vortex shedding. Physically, the separation point needs to be shifted much further for a high AR, which confirms the finding that a higher Ri_c is found. At AR = 0.7, the Ri difference is approximately 0.1. This difference is significantly less than the difference found by Wan and Patnaik, but their comparison was at a much lower reduced mass [7]. No comparison was made by Wan and Patnaik between the two regions at the higher reduced mass. As the AR increases, Ri_c converges between the two regimes to where they are essentially equal by AR = 4.

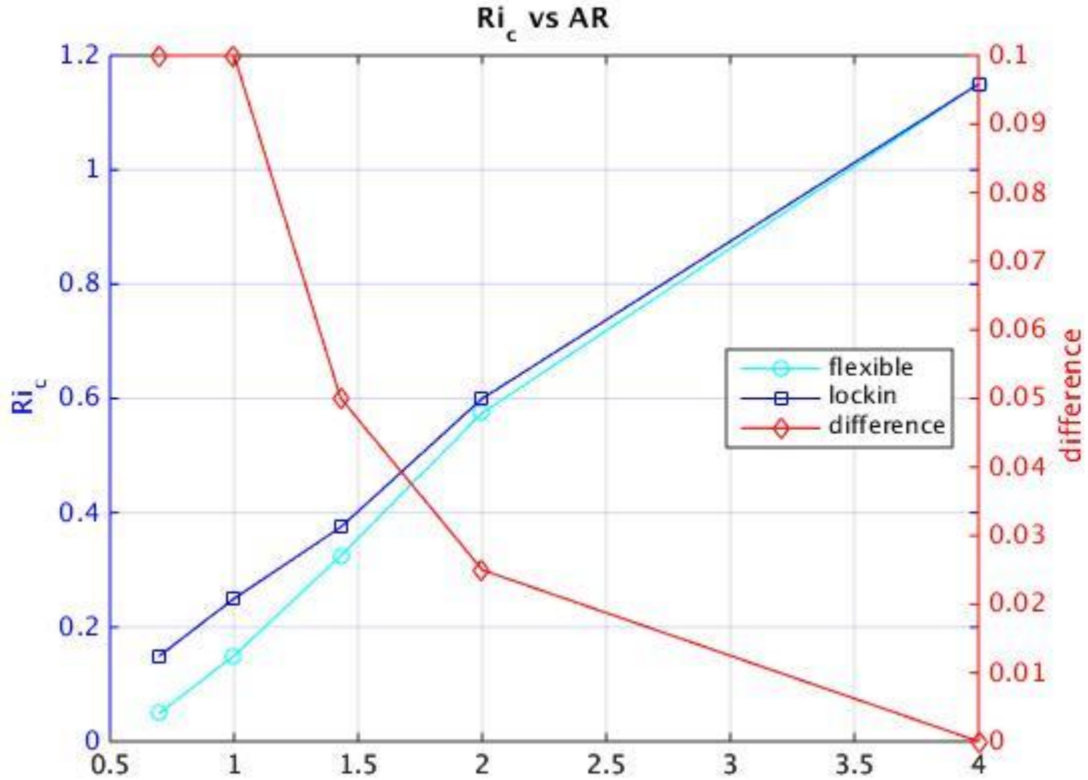

Figure 46. Ri_c as a function of AR. The left axis in blue represents the values of Ri_c where the right axis in red shows the difference in Ri_c between the body in lock-in and the flexible regimes for each AR.

V Conclusion

Vortex-induced transverse vibration of elastically-mounted, elliptical cylinders subject to a flow of Reynolds number 100 is simulated using numerical methods. Aspect ratios 0.7, 1, 1.43, 2, and 4 were considered. The mass and stiffness are represented by their non-dimensional parameters, reduced mass and reduced velocity, respectively. The reduced mass of the cylinders is selected as 10 to simulate a steel cylinder in water. The reduced velocity is varied between 1 and 9. As the reduced velocity increases, the stiffness of the cylinder decreases. A lock-in region is determined when the frequency of the vortex shedding closely matches the natural frequency body immersed in fluid. A flexible region was determined when the stiffness was too low for the frequencies to align, and the lift coefficient and motion are out of phase. It was found that as the aspect ratio is increased, the VIV amplitude and the associated drag coefficient also increased. This was true for both the lock-in and flexible regimes.

The cylinder was then heated to a uniform surface temperature to evaluate how thermal effects could lead to VIV suppression. For this to be possible, the flow direction had to be aligned with direction of the thermal induced buoyancy force. Buoyant forces within the heated fluid cause the boundary layer separation point to shift aft on the body. To achieve suppression, the vortex shedding must be reduced to bound vortices that remain attached to the aft end of the body. This investigation was completed by varying the Richardson number. As *Ri* increases, the vibrational amplitude is reduced. Eventually, the amplitude is reduced to zero when the vortices are no longer shedding.

Although the amplitude may be reduced by increasing *Ri*, a penalty in drag occurs by increasing the shear stress at the body’s surface. For the bodies within the lock-in regime, the drag coefficient is decreased as the amplitude decreases until it reaches a local minimum. Once the motion is eliminated, the drag coefficient begins to rise as *Ri* is further increased. Thus a optimum value of *Ri*, the critical Richardson number, is achieved when both the drag coefficient and amplitude are reduced.

For a flexible body, it remains true that as *Ri* increases, the vibrational amplitude decreases until it reaches zero; however, the trend in drag is different than that found in the lock-in regime. For all aspect ratios, the drag coefficient begins to increase as *Ri* is increased. For AR = 1.43, 2, and 4 as the amplitude drops off, the drag coefficient begins to decrease until it reaches a local minimum, then begins to increase thereafter. For AR = 0.7 and 1, the drag coefficient increases at a lower rate as the rate of suppression increases. Then the drag coefficient increases at a faster rate once suppression is achieved. The *Ri* where the local minimum, or point of slope increase, closely coincides with the *Ri* of complete suppression. Therefore, a critical Richardson number can also be determined for the flexible regime.

For both regimes, the drag coefficients are essentially equal and increases at the same rate with an increase in *Ri* once the VIV motion is suppressed. Additionally, most aspect ratios exhibit a higher critical Richardson number within lock-in than the flexible region. However, the Ri_c approaches the same value as AR increases. By AR = 4, Ri_c was essentially equal for the two regions.

A peak drag reduction of 44% can be obtained at the critical Richardson number for AR = 1.43. The drag is also reduced by 37-40% for AR = 1, 2, and 4. The drag reduction is small for AR = 0.7 (2.6%), but the VIV amplitudes for this aspect ratio were significantly smaller than the others and low *Ri* was required for suppression.

References

[1] T. Sarpkaya, “A critical review of the intrinsic nature of vortex-induced vibrations,” *J. Fluids Struct.*, vol. 19, pp. 389–447, 2004.

[2] V. Strouhal, “Ueber eine besondere Art der Tonerregung,” *Ann. der Phys. und Chemie*, vol. 241, no. 10, pp. 216–251, Jan. 1878.

[3] H. Bénard, “Formation de centres de giration à l’arrière d’un obstacle en mouvement,” *C. R. Acad. Sci. Paris*, vol. 147, pp. 839–842, 1908.

[4] T. Von Kármán, “Ueber den Mechanismus des Widerstandes, den ein bewegter Körper in einer Flüssigkeit erfährt,” *Nachrichten von der Gesellschaft der Wissenschaften zu Göttingen, Math. Klasse*, pp. 509–517, 1911.

[5] J. Wesfreid, “Henri Bénard: Thermal convection and vortex shedding,” *C. R. Mec.*, vol. 345, pp. 446–466, 2017.

[6] M. Zdravkovich, “Review and classification of various aerodynamic and hydrodynamic means for suppressing vortex shedding,” *J. Wind Eng. Ind. Aerodyn.*, vol. 7, no. 2, pp. 145–189, 1981.

[7] H. Wan and S. Patnaik, “Suppression of vortex-induced vibration of a circular cylinder using thermal effects,” *Phys. Fluids*, vol. 28, no. 12, 2016.

[8] N. Navrose, V. Yogeswaran, S. Sen, and S. Mittal, “Free vibrations of an elliptic cylinder at low Reynolds numbers,” *J. Fluids Struct.*, vol. 51, pp. 55–67, 2014.

[9] T. Prasanth and S. Mittal, “Vortex-induced vibrations of a circular cylinder at low Reynolds numbers,” *J. Fluid Mech.*, vol. 594, pp. 463–491, 2008.

[10] P. Bearman and M. Brankovi, “Experimental studies of passive control of vortex-induced vibration,” *Eur. J. Mech. B/Fluids*, vol. 23, pp. 9–15, 2004.

[11] S. Rashidi, M. Hayatdavoodi, and J. Esfahani, “Vortex shedding suppression and wake control: A review,” *Ocean Eng.*, vol. 126, pp. 57–80, 2016.

[12] D. Gao, W. Chen, H. Li, and H. Hu, “Flow around a circular cylinder with slit,” *Exp. Therm. Fluid Sci.*, vol. 82, pp. 287–301, 2017.

[13] S. Soumya and K. Prakash, “Effect of splitter plate on passive control and drag reduction for fluid flow past an elliptic cylinder,” *Ocean Engineering*, vol. 141. pp. 351–374, 2017.

[14] J. Wu, C. Shu, and N. Zhao, “Investigation of flow characteristics around a stationary circular cylinder with an undulatory plate,” *Eur. J. Mech. B/Fluids*, vol. 48, pp. 27–39, 2014.

[15] M. Zdravkovich, “Review of Flow Interference Between Two Circular Cylinders in Various Arrangements,” *J. Fluids Eng.*, vol. 99, no. 4, p. 618, 1977.

[16] M. Zdravkovich, “The Effects of Interference Between Circular Cylinders in Cross-Flow,” *J. Fluids Struct.*, vol. 1, no. 2, pp. 239–261, 1987.

[17] M. Zdravkovich, “Review of interference-induced oscillations in flow past two parallel circular cylinders in various arrangements,” *J. Wind Eng. Ind. Aerodyn.*, vol. 28, no. 2, pp. 183--200, 1988.

[18] D. Sumner, “Two circular cylinders in cross-flow: A review,” *J. Fluids Struct.*, vol. 26, pp. 849–899, 2010.

[19] Y. Zhou and M. Alam, “Wake of two interacting circular cylinders: A review,” *Int. J. Heat Fluid Flow*, vol. 62, pp. 510–537, 2016.

[20] C. Evangelinos, D. Lucor, and G. E. Karniadakis, “DNS-derived force distribution on flexible cylinders subject to vortex-induced vibrations,” *J. Fluids Struct.*, vol. 14, no. 429–440, pp. 429–440, 2000.

[21] Z. Song, M. Duan, and J. Gu, “Numerical investigation on the suppression of VIV for a circular cylinder by three small control rods,” *Phys. Procedia*, vol. 64, pp. 169–183, 2017.

[22] M. Silva-Ortega and G. R. S. Assi, “Flow-induced vibration of a circular cylinder surrounded by two, four and eight wake-control cylinders,” *Exp. Therm. Fluid Sci.*, vol. 85, pp. 354–362, 2017.

[23] G. Artana, R. Sosa, E. Moreau, and G. Touchard, “Control of the near-wake flow around a circular cylinder with electrohydrodynamic actuators,” *Exp. Fluids*, vol. 35, no. 6, pp. 580–588, 2003.

[24] J. Ffowcs Williams and B. Zhao, “The active control of vortex shedding,” *J. Fluids Struct.*, vol. 3, no. 2, pp. 115–122, 1989.

[25] M. Zhang, L. Cheng, and Y. Zhou, “Closed-loop-controlled vortex shedding and vibration of a flexibly supported square cylinder under different schemes,” *Phys. Fluids*, vol. 16, no. 5, pp. 1439–1448, 2004.

[26] M. Zhang, L. Cheng, and Y. Zhou, “Closed-loop control of fluid-structure interactions on a flexibly supported cylinder,” in *European Journal of Mechanics, B/Fluids*, 2004, vol. 23, no. 1, pp. 189–197.

[27] K.-S. Chang and J.-Y. Sa, “The effect of buoyancy on vortex shedding in the near wake of a circular cylinder,” *J. Fluid Mech.*, vol. 220, no. 1, p. 253, Nov. 1990.

[28] N. Michaux and M. Bélorgey, “Near-wake behavior of a heated circular cylinder: Viscosity-buoyancy duality,” *Exp. Therm. Fluid Sci.*, vol. 15, no. 2, pp. 91–100, 1997.

[29] H. Wan and S. S. Patnaik, “Suppression of vortex-induced vibration of a circular cylinder using thermal effects,” *Phys. Fluids*, vol. 28, no. 12, 2016.

[30] D. Newman and G. Karniadakis, “A direct numerical simulation study of flow past a

freely vibrating cable," *J. Fluid Mech.*, vol. 344, no. 1, pp. 95–136, 1997.

[31] O. Darrigol, "Joseph Boussinesq's legacy in fluid mechanics," *C. R. Mec.*, vol. 345, pp. 427–445, 2017.

[32] S. Jayanti, "Reynolds Aanalogy," *A-to-Z Guide to Thermodynamics, Heat and Mass Transfer, and Fluids Engineering,* 2011. [Online]. Available: http://www.thermopedia.com/content/1092/. [Accessed: 24-Jan-2018].

[33] R. Mittal and S. Balachandar, "Direct Numerical Simulation of Flow Past Elliptic Cylinders," *J. Comput. Phys.*, 1996.

[34] L. Song and S. Wu, "Numerical Simulation of Incompressible Viscous Flow Using an Implicit Fractional Step Method on Collocated Grid," vol. 2, no. Mems, pp. 81–84, 2012.

[35] H. Wan, H. Dong, and Z. Liang, "Vortex Formation of Freely Falling Plates."

[36] J. Kim and P. Mciin, "Application of a Fractional-Step Method to Incompressible Navier-Stokes Equations," *J. Comput. Phys.*, vol. 59, pp. 308–323, 1985.

[37] J. L. Guermond, P. Minev, and J. Shen, "An overview of projection methods for incompressible flows," *Comput. Methods Appl. Mech. Eng.*, vol. 195, no. 44–47, pp. 6011–6045, 2006.

[38] R. Mittal and G. Iaccarino, "Immersed Boundary Methods," *Annu. Rev. Fluid Mech.*, vol. 37, no. 1, pp. 239–261, 2005.

[39] R. Mittal, H. Dong, M. Bozkurttas, F. M. Najjar, A. Vargas, and A. von Loebbecke, "A versatile sharp interface immersed boundary method for incompressible flows with complex boundaries," *J. Comput. Phys.*, vol. 227, no. 10, pp. 4825–4852, 2008.

[40] R. Ghias, R. Mittal, and H. Dong, "A sharp interface immersed boundary method for compressible viscous flows," *J. Comput. Phys.*, vol. 225, no. 1, pp. 528–553, 2007.

[41] D. Shiels, A. Leonard, and A. Roshko, “Flow-induced vibration of a circular cylinder at limiting structural parameters,” *J. Fluids Struct.*, vol. 15, no. 1, pp. 3–21, 2001.

[42] L. Qu, C. Norberg, L. Davidson, S.-H. Peng, and F. Wang, “Quantitative numerical analysis of flow past a circular cylinder at Reynolds number between 50 and 200,” *J. Fluids Struct.*, vol. 39, pp. 347–370, 2013.

[43] C. Liu, X. Zheng, and C. H. Sung, “Preconditioned Multigrid Methods for Unsteady Incompressible Flows,” *J. Comput. Phys.*, vol. 139, no. 1, pp. 35–57, 1998.

[44] S. Etienne and D. Pelletier, “The low Reynolds number limit of vortex-induced vibrations,” *J. Fluids Struct.*, vol. 31, pp. 18–29, 2012.

[45] J. Meneghini, F. Saltara, C. Siqueira, and J. Ferrari Jr, “Numerical Simulataion of Flow Interference Between Two Circular Cylinders in Tandem and side-by-Side Arrangements,” *J. Fluids Struct.*, vol. 16, no. 15, pp. 399–413, 2001.

[46] H. Blackburn and R. Henderson, “A study of two-dimensional flow past an oscillating cylinder,” *J. Fluid Mech.*, vol. 385, 1999.

[47] V. Patnaik and K. Seetharamu, “Numerical simulation of vortex shedding past a circular cylinder under the influence of buoyancy,” *Int. J. Heat Mass Transf.*, vol. 42, no. 18, pp. 3495–3507, 1999.

[48] A. Srinivas, R. Bharti, and R. Chhabra, “Mixed convection heat transfer from a cylinder in power-law fluids: Effect of aiding buoyancy,” *Ind. Eng. Chem. Res.*, vol. 48, no. 21, pp. 9735–9754, 2009.

[49] A. Sharma and V. Eswaran, “Effect of channel-confinement and aiding/opposing buoyancy on the two-dimensional laminar flow and heat transfer across a square cylinder,” *Int. J. Heat Mass Transf.*, vol. 48, no. 25–26, pp. 5310–5322, Dec. 2005.

[50] T. Sengupta, K. Venkatasubbaiah, and S. Pawar, “Nonlinear instability of mixed convection flow over a horizontal cylinder,” *Acta Mech.*, vol. 201, no. 1–4, pp. 197–210, 2008.

[51] N. Hasan and R. Ali, “Vortex-shedding suppression in two-dimensional mixed convective flows past circular and square cylinders,” *Phys. Fluids*, vol. 25, no. 5, p. 53603, May 2013.

[52] H. Ahn and Y. Kallinderis, “Strongly coupled flow/structure interactions with a geometrically conservative ALE scheme on general hybrid meshes,” *J. Comput. Phys.*, vol. 219, no. 2, pp. 671–696, Dec. 2006.

[53] I. Borazjani and F. Sotiropoulos, “Vortex-induced vibrations of two cylinders in tandem arrangement in the proximity - Wake interference region,” *J. Fluid Mech.*, vol. 621, pp. 321–364, Feb. 2009.

[54] T. Tezduyar, M. Behr, S. Mittal, and J. Liou, “A new strategy for finite element computations involving moving boundaries and interfaces-The deforming-spatial-domain/space-time procedure: II. Computation of free-surface flows, two-liquid flows, and flows with drifting cylinders,” *Comput. Methods Appl. Mech. Eng.*, vol. 94, no. 3, pp. 353–371, 1992.

REPORT DOCUMENTATION PAGE	*Form Approved* *OMB No. 0704-0188*

1. REPORT DATE *(DD-MM-YYYY)* 22-03-2018	**2. REPORT TYPE** Master’s Thesis	**3. DATES COVERED** *(From - To)* September 2017 - March 2018

4. TITLE AND SUBTITLE Suppression of Vortex-Induced Vibrations for Elliptical Cylinders Using Mixed Convection	**5a. CONTRACT NUMBER**
	5b. GRANT NUMBER
	5c. PROGRAM ELEMENT NUMBER
6. AUTHOR(S) DesRoches, Jeffrey A, Capt	**5d. PROJECT NUMBER**
	5e. TASK NUMBER
	5f. WORK UNIT NUMBER
7. PERFORMING ORGANIZATION NAME(S) AND ADDRESS(ES) Air Force Institute of Technology Graduate School of Engineering and Management (AFIT/EN) 2950 Hobson Way, Building 640 WPAFB OH 45433-8865	**8. PERFORMING ORGANIZATION REPORT NUMBER** AFIT-ENY-MS-18-M-251
9. SPONSORING / MONITORING AGENCY NAME(S) AND ADDRESS(ES) AFRL/RQQI Dr. Soumya Patnaik 1050 5th Street B20018D RD201 WPAFB, Ohio 45433 soumya.patnaik.1@us.af.mil	**10. SPONSOR/MONITOR’S ACRONYM(S)** AFRL/RQQI
	11. SPONSOR/MONITOR’S REPORT NUMBER(S)

12. DISTRIBUTION / AVAILABILITY STATEMENT
DISTRIBUTION STATEMENT A.
APPROVED FOR PUBLIC RELEASE; DISTRIBUTION UNLIMITED.

13. SUPPLEMENTARY NOTES
This material is declared a work of the U.S. Government and is not subject to copyright protection in the United States.

14. ABSTRACT

Transverse vortex-induced vibrations (VIVs) of a 2-D, elliptic cylinder with various aspect ratios and stiffness are studied. The amplitude of transverse motion due to VIVs can be reduced as the thermal control parameter, the Richardson number (Ri), increases. Complete suppression is achieved when Ri is above a critical value. This critical Ri depends on both body-to-fluid density, aspect ratio, and structural stiffness. The study includes finding the lock-in regime for each aspect ratio, where the vibrational amplitude is at a maximum. Bodies at lock-in require a higher critical Ri to suppress VIV than either rigid or flexible structures; however, the gap between the critical Ris decreases with an increase in aspect ratio. Drag experienced by the body is also studied. A maximum drag reduction of 44% was found for an aspect ratio of 2 at the critical Richardson number.

15. SUBJECT TERMS
Vortex-Induced Vibrations, Vortex Shedding, Mixed Convection, VIV Suppression,

16. SECURITY CLASSIFICATION OF:			**17. LIMITATION OF ABSTRACT**	**18. NUMBER OF PAGES**	**19a. NAME OF RESPONSIBLE PERSON** Jeffrey DesRoches AFIT/ENY
a. REPORT U	**b. ABSTRACT** U	**c. THIS PAGE** U	UU	111	**19b. TELEPHONE NUMBER** *(include area code)* (774) 328-0535

Standard Form 298 (Rev. 8-98)
Prescribed by ANSI Std. Z39.18